

TECHNISCHE UNIVERSITÄT MÜNCHEN  
Lehrstuhl T31 für Theoretische Elementarteilchenphysik

# Semileptonic $B$ Decays in the Standard Model and Beyond

Michael Wick

Vollständiger Abdruck der von der Fakultät für Physik der Technischen Universität München zur Erlangung des akademischen Grades eines

Doktors der Naturwissenschaften (Dr. rer. nat.)

genehmigten Dissertation.

Vorsitzender: Univ.-Prof. Dr. Stephan Paul

Prüfer der Dissertation: 1. Univ.-Prof. Dr. Andrzej J. Buras  
2. Priv.-Doz. Dr. Andre H. I. Hoang

Die Dissertation wurde am 24.08.2010 bei der Technischen Universität München eingereicht und durch die Fakultät für Physik am 15.09.2010 angenommen.



# Zusammenfassung

In dieser Arbeit diskutieren wir verschiedene Aspekte von Zerfällen, die auf den Quarkniveau-Übergängen  $b \rightarrow s\nu\bar{\nu}$  und  $b \rightarrow s\mu^+\mu^-$  basieren, sowie Übergangs-Formfaktoren für radiative und seltene semileptonische  $B$ -Meson-Zerfälle.

Der Quarkniveau-Übergang  $b \rightarrow s\nu\bar{\nu}$  bietet die Möglichkeit, transparent  $Z$  Pinguin- und andere elektroschwache Pinguineffekte in Szenarien für Neue Physik (NP) in Abwesenheit von Dipoloperatorbeiträgen und Higgspinguinbeiträgen zu untersuchen. Wir beschreiben eine Analyse des Zerfalls  $B \rightarrow K^*\nu\bar{\nu}$  mit verbesserten Formfaktoren sowie der Zerfälle  $B \rightarrow K\nu\bar{\nu}$  und  $B \rightarrow X_s\nu\bar{\nu}$  im Rahmen des Standardmodells (SM) und in einer Reihe von NP-Szenarien wie dem allgemeinen Minimalen Supersymmetrischen Standardmodell (MSSM), Szenarien mit veränderten  $Z/Z'$  Pinguinen und in einer Erweiterung des SM durch ein skalares Singulett. Die Ergebnisse für das SM und die NP-Szenarien können anschaulich in einer  $(\epsilon, \eta)$ -Ebene visualisiert werden.

Der seltene Zerfall  $B \rightarrow K^*(\rightarrow K\pi)\mu^+\mu^-$  gilt als einer der entscheidenden Kanäle für die  $B$ -Physik, da er eine Vielzahl von Messgrößen bietet. Wir untersuchen systematisch die oft korrelierten Effekte in diesen Observablen im Rahmen des SM und verschiedener NP-Modelle, insbesondere des Littlest Higgs-Modells mit T-Parität und verschiedenen MSSM Szenarien und identifizieren diejenigen Observablen mit kleinerer bis mittlerer Abhängigkeit von hadronischen Größen und großem Einfluss der NP.

Darüber hinaus untersuchen wir die Übergangsformfaktoren für radiative und seltene semileptonische  $B$ -Meson-Zerfälle in leichte Pseudoskalare oder Vektormesonen, indem wir theoretische und phänomenologische Zwangsbedingungen von Gitter QCD, Lichtkegelsummenregeln und dispersiven Grenzen kombinieren. Besonderes Augenmerk legen wir auf die Parametrisierung der Formfaktoren, die auf der sogenannten Reihenentwicklung beruhen und analysieren in diesem Zusammenhang die systematischen Unsicherheiten auf quantitativer Ebene. In dieser Analyse sowie in der Analyse der  $b \rightarrow s$ -Übergänge nutzen wir konsequent eine zweckdienliche Definition der Formfaktoren auf Grundlage der Helizität.



# Abstract

In this thesis we study several aspects of decays based on the quark level transitions  $b \rightarrow s\nu\bar{\nu}$  and  $b \rightarrow s\mu^+\mu^-$  as well as transition form factors for radiative and rare semi-leptonic  $B$  meson decays.

The quark level transition  $b \rightarrow s\nu\bar{\nu}$  offers a transparent study of  $Z$  penguin and other electroweak penguin effects in New Physics (NP) scenarios in the absence of dipole operator contributions and Higgs penguin contributions. We present an analysis of  $B \rightarrow K^*\nu\bar{\nu}$  with improved form factors and of the decays  $B \rightarrow K\nu\bar{\nu}$  and  $B \rightarrow X_s\nu\bar{\nu}$  in the Standard Model (SM) and in a number of NP scenarios like the general Minimal Supersymmetric Standard Model (MSSM), general scenarios with modified  $Z/Z'$  penguins and in a singlet scalar extension of the SM. The results for the SM and NP scenarios can be transparently visualized in a  $(\epsilon, \eta)$  plane.

The rare decay  $B \rightarrow K^*(\rightarrow K\pi)\mu^+\mu^-$  is regarded as one of the crucial channels for  $B$  physics as it gives rise to a multitude of observables. We investigate systematically the often correlated effects in these observables in the context of the SM and various NP models, in particular the Littlest Higgs model with T-parity and various MSSM scenarios and identify those observables with small to moderate dependence on hadronic quantities and large impact of NP.

Furthermore, we study transition form factors for radiative and rare semi-leptonic  $B$ -meson decays into light pseudoscalar or vector mesons, combining theoretical and phenomenological constraints from Lattice QCD, light-cone sum rules, and dispersive bounds. We pay particular attention to form factor parameterizations which are based on the so-called series expansion, and study the related systematic uncertainties on a quantitative level. In this analysis as well as in the analysis of the  $b \rightarrow s$  transitions, we use consistently a convenient form factor definition on grounds of helicity.



# Contents

<b>1</b>	<b>Introduction</b>	<b>11</b>
<b>2</b>	<b>Transition Form Factors</b>	<b>15</b>
2.1	Definition of Form Factors . . . . .	16
2.2	Symmetry Limits . . . . .	19
2.2.1	Kinematic Endpoints . . . . .	19
2.2.2	Heavy Quark Limit . . . . .	19
2.2.3	Soft Collinear Limit . . . . .	20
2.3	Methods based on the Dispersive Relation . . . . .	21
2.3.1	Unitary Representation . . . . .	21
2.3.2	Short Distance and Light Cone Expansion . . . . .	23
2.3.3	Borel Transformation and Subtractions . . . . .	24
2.3.4	Resulting Information on the Form Factors . . . . .	24
2.4	Lattice QCD versus Light Cone Sum Rules . . . . .	25
2.5	Parametrization of Form Factors . . . . .	26
<b>3</b>	<b><math>B \rightarrow K^{(*)}\nu\nu</math> and <math>B \rightarrow X_s\nu\nu</math></b>	<b>29</b>
3.1	Introduction . . . . .	29
3.2	Effective Hamiltonian . . . . .	29
3.3	Observables . . . . .	30
3.3.1	$B \rightarrow K^*\nu\nu$ . . . . .	30
3.3.2	$B \rightarrow K\nu\nu$ . . . . .	34
3.3.3	$B \rightarrow X_s\nu\nu$ . . . . .	34
3.4	Experimental Bounds and Standard Model Predictions . . . . .	35
3.5	Model-independent Analysis of New Physics Effects . . . . .	36
3.5.1	Model-independent constraints on Wilson coefficients . . . . .	37
3.5.2	Modified $Z$ penguins . . . . .	39
3.5.3	Decay to invisible scalars . . . . .	42

3.6	Effects in specific New Physics Models . . . . .	45
3.6.1	Heavy $Z'$ . . . . .	45
3.6.2	Littlest Higgs with T-Parity . . . . .	46
3.6.3	Randall-Sundrum model with custodial protection . . . . .	47
3.6.4	Minimal Supersymmetric Standard Model (MSSM) . . . . .	47
<b>4</b>	<b><math>B \rightarrow K^* \mu^+ \mu^-</math></b>	<b>53</b>
4.1	Introduction . . . . .	53
4.2	Effective Hamiltonian . . . . .	53
4.3	Differential Decay Distribution . . . . .	55
4.3.1	Massless leptons . . . . .	57
4.3.2	Massive leptons . . . . .	60
4.3.3	The CP-conjugated mode . . . . .	61
4.4	Transversity amplitudes . . . . .	62
4.5	Additional Corrections to Transversity Amplitudes . . . . .	63
4.6	Observables . . . . .	64
4.6.1	Differential Observables . . . . .	65
4.6.2	Integrated Observables . . . . .	67
4.6.3	Zero crossings . . . . .	67
4.7	Standard Model . . . . .	68
4.8	Model-independent Analysis . . . . .	73
4.9	Specific New Physics Scenarios . . . . .	78
4.9.1	Minimal Flavor Violation . . . . .	79
4.9.2	Minimal Flavor Violating MSSM . . . . .	79
4.9.3	Flavor Blind MSSM . . . . .	80
4.9.4	Littlest Higgs with T-Parity . . . . .	83
4.9.5	General MSSM . . . . .	85
<b>5</b>	<b>Series Expansion</b>	<b>91</b>
5.1	Introduction . . . . .	91
5.2	Dispersive Bounds . . . . .	91
5.2.1	Unitary representation of the correlator . . . . .	92
5.2.2	Operator Product Expansion for the Correlator . . . . .	94
5.2.3	Dispersive Bounds . . . . .	94
5.3	Series Expansion Parametrization . . . . .	95
5.4	Simplified Series Expansion . . . . .	98

5.5	Fitting prescription . . . . .	99
5.6	Results . . . . .	101
<b>6</b>	<b>Summary and Outlook</b>	<b>111</b>
<b>A</b>	<b>Kinematics and Polarization Vectors</b>	<b>115</b>
<b>B</b>	<b>Calculation of Wilson Coefficients</b>	<b>117</b>
B.1	Perturbative Contribution . . . . .	117
B.2	Condensate Contribution to the Correlation Functions . . . . .	120
B.3	Results . . . . .	122
B.4	Decomposition of the tensor-current correlator . . . . .	124
<b>C</b>	<b>Input Data for the Series Expansion</b>	<b>127</b>



# Chapter 1

## Introduction

The Large Hadron Collider (LHC) at CERN, one of mankind's most ambitious scientific enterprises, started in 2009 to take first data. The main goal of the experiments performed at the LHC is to discover new particles and forces. Specifically, most of the current interest is focused on the Higgs mechanism. This mechanism and its prediction, the Higgs particle, plays a crucial and dual role in modern particle physics:

On the one hand, the detection of the Higgs particle would be the capstone of the experimental validation of the so-called Standard Model of Particle Physics (SM). This model, established in the early 70's of the last century, describes an extremely broad range of physical phenomena, even though it is extremely compact in its mathematical formulation. In this framework, the Higgs mechanism triggers the electroweak symmetry breaking and generates also the masses of quarks and charged leptons.

On the other hand, the Higgs particle can be seen as the Achilles' heel of the SM. In fact, each of the couplings of the Higgs boson postulated in the SM – to itself or to matter – gives rise to severe problems. These problems were pointed out soon after the formulation of the SM and were termed the vacuum energy problem [1], the electroweak hierarchy problem [2], the vacuum instability problem [3] and the flavor problem [4].

The two problems probably most discussed in particle physics are the electroweak hierarchy problem and the flavor problem. The electroweak hierarchy problem deals with the vast energy scale difference between the electroweak breaking scale and the Planck scale. This difference goes hand in hand with a vast correction to the Higgs mass due to quantum fluctuations. The related flavor problem describes the clash of the expectation of a sign of NP to cure the electroweak hierarchy problem at an energy scale of 1 TeV and the lack of any experimental observation of such modification in flavor violating transitions up to an effective energy scale of 4-5 TeV.

---

Most of the extensions of the SM discussed nowadays, commonly termed as New Physics (NP), address at least one of these two problems.

The most reasonable solution to the flavor problem is the so-called Minimal Flavor Violation (MFV) hypothesis. Under this assumption the NP interactions leading to flavor violation in the respective SM extension are linked to the known structure of Yukawa couplings of the SM. As a result, the flavor changing contributions of the respective NP scenario are suppressed and in agreement with the experimental information on flavor observables.

One of the best motivated approaches to the electroweak hierarchy problem is the introduction of a new symmetry of space-time, supersymmetry, which maps the known set of particles to an as yet undiscovered set of mirror particles. The huge quantum corrections are cancelled, as the respective quantum fluctuations of each of the new particles contributes oppositely to the corresponding quantum fluctuations associated with the original particle. A full formulation of this idea was given by the now well-established Minimal Supersymmetric Standard Model (MSSM), which contains also a heuristic parametrization of the soft breaking of supersymmetry.

All extensions of the SM have in common that they can be probed in principle in two ways: directly, through the production of new particles, or in quantum fluctuations involving new particles which modify decays of SM particles. Both approaches are realized at the upcoming LHC experiments. Specifically, at the LHCb experiment, exclusive  $B$  meson decays will play a major role for precision tests of the flavor sector in the SM and its possible NP extensions. Special attention is attracted by the rare decay  $B \rightarrow K^*(\rightarrow K\pi)\mu^+\mu^-$ . Since all decay products are charged, this decay gives access to a broad set of observables and since also the charge-conjugated decay is experimentally accessible the observables are partly sensitive to CP violation.

While the hadronic part is identical to  $B \rightarrow K^*(\rightarrow K\pi)\mu^+\mu^-$ , the decay  $B \rightarrow K^*(\rightarrow K\pi)\nu\bar{\nu}$  is very different in many other aspects. Although the neutrinos cannot be detected experimentally and consequently only two observables can be measured, the neutral and massless final states open a unique possibility to transparently study  $Z$  penguin effects. The analysis of these effects in the context of other decays probing the quark level decay  $b \rightarrow s\nu\bar{\nu}$  completes the available theoretical information on this decay and the Super-B facilities make the measurement realistic.

In order to extract information on the underlying short-distance transitions between different quark flavors of the above mentioned decay, hadronic matrix elements will be required as theoretical input and the precision to which they can be predicted will be essential for the success of the flavor program at LHCb.

This thesis is organized as follows. In chapter 2, we recall some properties of form factors and provide convenient definitions for  $B$  meson form factors. Furthermore, we give a brief introduction on methods based on the dispersive relation.

In chapter 3, we define the observables that can in principle be measured in  $B \rightarrow K^*(\rightarrow K\pi)\nu\bar{\nu}$ ,  $B \rightarrow K\nu\bar{\nu}$  as well as  $B \rightarrow X_s\nu\bar{\nu}$  and present a numerical analysis of these decays, first within and then beyond the SM, both model-independently and within concrete extensions of the SM.

In chapter 4, we review the effective Hamiltonian governing the decay  $B \rightarrow K^*(\rightarrow K\pi)\mu^+\mu^-$ , discuss the kinematics of the decay and define the basic observables in the process. The definition satisfies the requirements of theoretical cleanliness and high sensitivity to NP effects. We present the result of a phenomenological analysis of those observables in the SM, in a model-independent way and in several selected NP scenarios.

In chapter 5, we introduce the idea of the so-called series expansion (SE) of the dependence of the form factors on the momentum exchange. Then we review the derivation of dispersive bounds from current-correlation functions and summarize the results for the profile functions obtained from the operator product expansion. We apply our formalism to  $B \rightarrow K$  and  $B \rightarrow \rho$  form factors, by fitting the (truncated) SE to theoretical “data” from Quantum Chromodynamics (QCD) on the Lattice and/or Light Cone Sum Rules (LCSR).

We present our conclusions in chapter 6 and discuss some technical details in the appendix.



# Chapter 2

## Transition Form Factors

In this chapter, we will focus on the theoretical description and prediction of hadronic matrix elements entering  $B \rightarrow V\gamma$ ,  $B \rightarrow L\ell^+\ell^-$  and  $B \rightarrow L\nu\bar{\nu}$  decays, where  $L = P, V$  is a light pseudoscalar or vector meson.

In dealing with these hadronic matrix elements, one faces two levels of parametrization.

- The first level of parametrization is the definition of the form factors. The form factors are scalar functions arising as coefficients in the parametrization of the Lorentz vector-like hadronic matrix elements in terms of the relevant momenta and polarization vectors. In this thesis we use a form factor definition based on a projection of the hadronic matrix element on a complete orthogonal set of polarization states of a virtual vector boson (representing either the  $\gamma$  or the dileptons  $\ell^+\ell^-$  or  $\nu\bar{\nu}$ ) radiated in the transition  $B \rightarrow L$ .
- The second level of parametrization deals with the dependence of the form factors on the momentum transfer  $q^\mu$  over the kinematically allowed range. This is important in order to compare results among different form factor calculations (e.g. LCSR, Lattice QCD or dispersive bounds) and to use these results in the prediction of decay observables. Two important, often conflicting criteria for a parametrization are the quality of the fit to results of calculations at different  $q^2$  and a minimal number of parameters to give predictive results.

In the following, we discuss the definition of the form factors used in this thesis and their parametrization in  $q^2$ , including the analytical behavior of the form factors in certain physical limits, and give a brief overview of methods based on the dispersive relation.

## 2.1 Definition of Form Factors

The hadronic matrix elements for a transition between a pseudoscalar  $B$  meson and a generic pseudoscalar meson are usually written in terms of three form factors,  $f_0(q^2)$ ,  $f_+(q^2)$  and  $f_T(q^2)$ , which depend on the momentum transfer  $q^2 = (p - k)^2$ :

$$\begin{aligned}\langle P(k) | \bar{q} \gamma_\mu b | B(p) \rangle &= \left( p_\mu + k_\mu - q_\mu \frac{m_B^2 - m_P^2}{q^2} \right) f_+(q^2) + \frac{m_B^2 - m_P^2}{q^2} q_\mu f_0(q^2), \\ \langle P(k) | \bar{q} \sigma_{\mu\nu} q^\nu b | B(p) \rangle &= \frac{i}{m_B + m_P} \left( q^2 (p + k)_\mu - (m_B^2 - m_P^2) q_\mu \right) f_T(q^2).\end{aligned}\quad (2.1)$$

Note that, at zero momentum transfer, the additional relation  $f_+(0) = f_0(0)$  holds.

Similarly, the matrix elements for a transition between a  $B$  meson and a generic vector meson can be expressed in terms of another set of form factors,  $V(q^2)$ ,  $A_{0-3}(q^2)$ ,  $T_{1-3}(q^2)$  conventionally defined as:

$$\begin{aligned}\langle V(k, \varepsilon) | \bar{q} \gamma_\mu b | \bar{B}(p) \rangle &= i \epsilon_{\mu\nu\rho\sigma} \varepsilon^{*\nu}(k) p^\rho k^\sigma \frac{2V(q^2)}{m_B + m_V}, \\ \langle V(k, \varepsilon) | \bar{q} \gamma_\mu \gamma_5 b | \bar{B}(p) \rangle &= -\varepsilon_\mu^*(k) (m_B + m_V) A_1(q^2) + (p + k)_\mu (\varepsilon^*(k) \cdot q) \frac{A_2(q^2)}{m_B + m_V} \\ &\quad + q_\mu (\varepsilon^*(k) \cdot q) \frac{2m_V}{q^2} (A_3(q^2) - A_0(q^2)),\end{aligned}\quad (2.2)$$

where  $A_0(0) = A_3(0)$ . For transitions involving a tensor current, the matrix elements are characterized by the tensor form factors:

$$\begin{aligned}\langle V(k, \varepsilon) | \bar{q} \sigma_{\mu\nu} q^\nu b | \bar{B}(p) \rangle &= i \epsilon_{\mu\nu\rho\sigma} \varepsilon^{*\nu} p^\rho k^\sigma 2T_1(q^2), \\ \langle V(k, \varepsilon) | \bar{q} \sigma_{\mu\nu} q^\nu \gamma_5 b | \bar{B}(p) \rangle &= T_2(q^2) (\varepsilon_\mu^*(k) (m_B^2 - m_V^2) - (\varepsilon^*(k) \cdot q) (p + k)_\mu) \\ &\quad + T_3(q^2) (\varepsilon^*(k) \cdot q) \left( q_\mu - \frac{q^2}{m_B^2 - m_V^2} (2p - q)_\mu \right),\end{aligned}\quad (2.3)$$

where  $T_1(0) = T_2(0)$ . The equations of motion for the quarks imply an additional constraint,

$$A_3(q^2) = \frac{m_B + m_V}{2m_V} A_1(q^2) - \frac{m_B - m_V}{2m_V} A_2(q^2),\quad (2.4)$$

and therefore the  $B \rightarrow V$  transitions are characterized by seven independent form factors. The above constitute the standard definitions of the form factors widely used in the literature. However, for the purpose of this thesis, it is convenient to use certain linear

## 2. Transition Form Factors

---

combinations of these, dubbed helicity amplitudes in ref. [5]. They have the following advantages over the traditional form factors:

- They have definite spin-parity quantum numbers, which is useful when considering the contribution of excited states or in the context of Light Cone Sum Rules and Lattice QCD.
- They have simple relations to the universal form factors, appearing in the heavy-quark and/or large-energy limit.
- They lead to particularly simple expressions for the observables in the  $B \rightarrow K^* \nu \bar{\nu}$  and  $B \rightarrow K^* \ell^+ \ell^-$  decays, as is shown in chapters 3 and 4, respectively.
- They diagonalize the unitarity relations, which are used in chapter 5 to derive the dispersive bounds on certain form factor parameterizations.

These helicity form factors are defined as the coefficients of a projection of the matrix element on a set of polarization vectors of a (virtual) vector boson carrying the four momentum  $q^\mu$ . Since the set of polarization vectors is complete and orthogonal, the form factors are conveniently defined through the Lorentz contraction of the relevant matrix element and the respective polarization vector. In order to put the contributions to the various current correlation functions entering the dispersive bounds on an equal footing, we also choose a particular normalization convention and define new  $B \rightarrow P$  vector form factors via

$$\mathcal{A}_{V,\sigma}(q^2) = \sqrt{\frac{q^2}{\lambda}} \varepsilon_\sigma^{*\mu}(q) \langle P(k) | \bar{q} \gamma_\mu b | \bar{B}(p) \rangle. \quad (2.5)$$

Here,

$$\lambda = ((m_B - m_P)^2 - q^2) ((m_B + m_P)^2 - q^2) \quad (2.6)$$

is a standard kinematic function, which often recurs in this thesis, although with different masses. It should always be clear from the context which masses are meant. Furthermore, the polarization vector  $\varepsilon_\sigma^{*\mu}(q)$  – transverse ( $\sigma = \pm$ ), longitudinal ( $\sigma = 0$ ) or time-like ( $\sigma = t$ ) – is defined in appendix (A.1). These definitions imply that

$$\mathcal{A}_{V,0}(q^2) = f_+(q^2), \quad \mathcal{A}_{V,t}(q^2) = \frac{m_B^2 - m_P^2}{\sqrt{\lambda}} f_0(q^2), \quad (2.7)$$

while the transverse projections vanish. Similarly, for the  $B \rightarrow P$  tensor form factor, we

define

$$\mathcal{A}_{T,\sigma}(q^2) = (-i) \sqrt{\frac{1}{\lambda}} \varepsilon_\sigma^{*\mu}(q) \langle P(k) | \bar{q} \sigma_{\mu\nu} q^\nu b | \bar{B}(p) \rangle. \quad (2.8)$$

Here, the only non-zero form factor is<sup>1</sup>

$$\mathcal{A}_{T,0}(q^2) = \frac{\sqrt{q^2}}{m_B + m_P} f_T(q^2). \quad (2.9)$$

A similar analysis for the  $B \rightarrow V$  vector and axial-vector form factors yields

$$\mathcal{B}_{V,\sigma}(q^2) = \sqrt{\frac{q^2}{\lambda}} \sum_{\varepsilon(k)} \varepsilon_\sigma^{*\mu}(q) \langle V(k, \varepsilon(k)) | \bar{q} \gamma_\mu (1 - \gamma^5) b | \bar{B}(p) \rangle \quad (2.10)$$

with

$$\begin{aligned} \mathcal{B}_{V,0}(q^2) &= \frac{(m_B + m_V)^2 (m_B^2 - m_V^2 - q^2) A_1(q^2) - \lambda A_2(q^2)}{2m_V \sqrt{\lambda} (m_B + m_V)}, \\ \mathcal{B}_{V,t}(q^2) &= A_0(q^2), \\ \mathcal{B}_{V,1}(q^2) &= -\frac{\mathcal{B}_{V,-} - \mathcal{B}_{V,+}}{\sqrt{2}} = \frac{\sqrt{2} q^2}{m_B + m_V} V(q^2), \\ \mathcal{B}_{V,2}(q^2) &= -\frac{\mathcal{B}_{V,-} + \mathcal{B}_{V,+}}{\sqrt{2}} = \frac{\sqrt{2} q^2 (m_B + m_V)}{\sqrt{\lambda}} A_1(q^2). \end{aligned} \quad (2.11)$$

Finally, the  $B \rightarrow V$  matrix elements with tensor currents are defined as

$$\mathcal{B}_{T,\sigma}(q^2) = \sqrt{\frac{1}{\lambda}} \sum_{\varepsilon(k)} \varepsilon_\sigma^{*\mu}(q) \langle V(k, \varepsilon(k)) | \bar{q} \sigma_{\mu\alpha} q^\alpha (1 + \gamma^5) b | \bar{B}(p) \rangle \quad (2.12)$$

giving rise to the form factors:

$$\begin{aligned} \mathcal{B}_{T,0}(q^2) &= \frac{\sqrt{q^2} (m_B^2 + 3m_V^2 - q^2)}{2m_V \sqrt{\lambda}} T_2(q^2) - \frac{\sqrt{q^2} \lambda}{2m_V (m_B^2 - m_V^2)} T_3(q^2), \\ \mathcal{B}_{T,1}(q^2) &= -\frac{\mathcal{B}_{V,-} - \mathcal{B}_{V,+}}{\sqrt{2}} = \sqrt{2} T_1(q^2), \end{aligned}$$

---

<sup>1</sup>The newly defined tensor form factor  $\mathcal{A}_{T,0}(q^2)$  vanishes as  $\sqrt{q^2}$  for  $q^2 \rightarrow 0$ , which might look somewhat artificial at first glance. However, the tensor current does not contribute to physical processes at  $q^2 = 0$  anyway.

## 2. Transition Form Factors

---

$$\mathcal{B}_{T,2}(q^2) = -\frac{\mathcal{B}_{V,-} + \mathcal{B}_{V,+}}{\sqrt{2}} = \frac{\sqrt{2}(m_B^2 - m_V^2)}{\sqrt{\lambda}} T_2(q^2). \quad (2.13)$$

Note that, in the following, we drop the explicit dependence of the form factors on  $q^2$  in our notation.

## 2.2 Symmetry Limits

In the limit of infinite  $b$  quark mass, for highly energetic light mesons or at the edges of the kinematically allowed  $q^2$  range, new symmetries arise which imply a redundancy among the hadronic matrix elements, and thus relations among the form factors. In this section, we summarize these useful properties of the helicity-based form factors, following from the definitions in eqs. (2.5, 2.8, 2.10, 2.12).

### 2.2.1 Kinematic Endpoints

From the equation of motion for vanishing momentum transfer,  $q^2 \rightarrow 0$ , it follows that

$$\mathcal{A}_{V,0}(0) = \mathcal{A}_{V,t}(0) = f_0(0) = f_+(0), \quad (2.14)$$

and

$$\begin{aligned} \mathcal{B}_{V,0}(0) &= \mathcal{B}_{V,t}(0) = A_0(0) = A_3(0), \\ \mathcal{B}_{T,1}(0) &= \mathcal{B}_{T,2}(0) = \sqrt{2} T_1(0) = \sqrt{2} T_2(0), \end{aligned} \quad (2.15)$$

while the other form factors  $\mathcal{A}_{T,0}$ ,  $\mathcal{B}_{V,1}$ ,  $\mathcal{B}_{V,2}$ , and  $\mathcal{B}_{T,0}$  behave as  $\sqrt{q^2}$  for  $q^2 \rightarrow 0$ . Similarly, at the kinematic endpoint  $q^2 = (m_B - m_L)^2$ , we obtain the relations

$$\lim_{q^2 \rightarrow (m_B - m_L)^2} \frac{\mathcal{B}_{V,2}(q^2)}{\mathcal{B}_{V,0}(q^2)} = \lim_{q^2 \rightarrow (m_B - m_L)^2} \frac{\mathcal{B}_{T,2}(q^2)}{\mathcal{B}_{T,0}(q^2)} = \sqrt{2}. \quad (2.16)$$

### 2.2.2 Heavy Quark Limit

In the infinite-mass limit  $m_b \rightarrow \infty$ , the number of independent form factors reduces from 7 to a single form factor  $\xi$ , usually called the Isgur-Wise function [6]. In this case the

vector form factors obey the following relations :

$$\xi(q^2) = \begin{cases} \sqrt{\frac{m_V}{m_B}} \mathcal{B}_{V,i} & \text{for } i = t, 0 \\ \sqrt{\frac{2m_B m_V}{q^2}} \mathcal{B}_{V,i} & \text{for } i = 1, 2 \end{cases} \quad (2.17)$$

Furthermore in this limit the form factors obey spin-symmetry relations [7] connecting vector and tensor form factors:

$$2m_B \sqrt{q^2} \mathcal{A}_{T,0} = \mathcal{A}_{V,t} (q^2 - m_B^2) + \mathcal{A}_{V,0} (m_B^2 + q^2) \quad (2.18)$$

$$2m_B \sqrt{q^2} \mathcal{B}_{T,0} = \mathcal{B}_{V,t} (m_B^2 - q^2) + \mathcal{B}_{V,0} (m_B^2 + q^2) \quad (2.19)$$

$$2m_B \sqrt{q^2} \mathcal{B}_{T,1} = \mathcal{B}_{V,1} (m_B^2 + q^2) + \mathcal{B}_{V,2} (m_B^2 - q^2) \quad (2.20)$$

$$2m_B \sqrt{q^2} \mathcal{B}_{T,2} = \mathcal{B}_{V,1} (m_B^2 - q^2) + \mathcal{B}_{V,2} (m_B^2 + q^2). \quad (2.21)$$

We note that the symmetric form of these relations is a further advantage of our choice of form factors.

### 2.2.3 Soft Collinear Limit

In the combined limit of infinite  $b$  quark mass and large recoil energy of the final state meson, the number of independent form factors reduces from 7 to 2 [8,9]. This reduction follows from the factorization of soft and collinear QCD dynamics [10–12]. In the case of  $B \rightarrow V$  decays, the two form factors correspond to the polarization of the daughter vector meson (transversal or longitudinal) and are usually denoted by  $\xi_{\perp}$  and  $\xi_{\parallel}$ :

$$\xi_{\parallel}(q^2) = \frac{m_V}{E} \mathcal{B}_{V,i} \quad \text{for } i = t, 0 \quad (2.22)$$

$$\xi_{\perp}(q^2) = \sqrt{\frac{m_B}{m_B - 2E}} \mathcal{B}_{V,i} \quad \text{for } i = 1, 2 \quad (2.23)$$

Here,  $E$  is the energy of the  $K^*$ , which is related to  $q^2$  by

$$E = \frac{m_B^2 + m_{K^*}^2 - q^2}{2m_B}. \quad (2.24)$$

## 2. Transition Form Factors

---

Furthermore, the tensor and vector form factors are related through

$$\mathcal{A}_{V,0} \simeq \mathcal{A}_{V,t} \simeq \frac{m_B}{\sqrt{q^2}} \mathcal{A}_{T,0} \quad (2.25)$$

and

$$\mathcal{B}_{V,0} \simeq \mathcal{B}_{V,t} \simeq \frac{m_B}{\sqrt{q^2}} \mathcal{B}_{T,0}, \quad \mathcal{B}_{V,1} \simeq \mathcal{B}_{V,2} \simeq \frac{\sqrt{q^2}}{m_B} \mathcal{B}_{T,1} \simeq \frac{\sqrt{q^2}}{m_B} \mathcal{B}_{T,2}. \quad (2.26)$$

## 2.3 Methods based on the Dispersive Relation

Besides the symmetry limits described above, other important sources of information on form factors are methods based on the dispersive relation<sup>2</sup>, like dispersive bounds, QCD sum rules<sup>3</sup> and LCSR. The crucial observation underlying these methods is the possibility to evaluate the correlator of two flavor-changing currents,

$$\Pi(q^2) = i \int d^4x e^{iq \cdot x} \langle X | T j_1(x) j_2^\dagger(0) | 0 \rangle, \quad (2.27)$$

by a short distance or a light cone expansion and alternatively by unitarity considerations. Note that  $|X\rangle$  is a generic hadronic state. In this section, for the sake of simplicity, we restrict ourselves to scalar currents. We extend the discussion to vector and tensor currents in chapter 5.

### 2.3.1 Unitary Representation

Unitarity allows to express the imaginary part of the correlator  $\Pi(q^2)$  as the positive definite sum over all hadronic states  $|n\rangle$  with allowed quantum numbers:

$$\text{Im} \Pi(q^2) = \frac{1}{2} \sum_n \langle X | j_1 | n \rangle \langle n | j_2 | 0 \rangle d\tau_n (2\pi)^4 \delta^{(4)}(q - p_n), \quad (2.28)$$

where  $p_n$  is the total momentum of the respective final state  $n$  and  $d\tau_n$  contains the appropriate phase space weighting. From a conceptual perspective, it is useful to split off the contribution of a generic ground state  $|Y\rangle$  and to summarize the remaining terms,

---

<sup>2</sup>See ref. [13] for an excellent review on the subject of QCD sum rules and LCSR

<sup>3</sup>With QCD sum rules we refer to the original method developed by Shifman, Vainshtein and Zakharov in [14]

including excited vector mesons and continuum states, as a continuous function  $\rho(q^2)$ :

$$\begin{aligned} \text{Im } \Pi(q^2) &= \frac{1}{2} \langle X | j_1 | Y \rangle \langle Y | j_2^\dagger | 0 \rangle d\tau_Y (2\pi)^4 \delta^{(4)}(q - p_Y) \\ &\quad + \rho(q^2) \theta(q^2 - s_0). \end{aligned} \quad (2.29)$$

The step function indicates that the continuous part contributes only above  $s_0$ , the so-called continuum threshold, which separates the ground-state from the continuum contribution.

Furthermore, Cauchy's theorem allows to express the full function  $\Pi(q^2)$  in terms of its imaginary part:

$$\Pi(q^2) = \frac{1}{\pi} \int_0^\infty ds \frac{\text{Im } \Pi(s)}{s - q^2 - i\epsilon}. \quad (2.30)$$

Depending on the choice of  $|Y\rangle$  and  $|X\rangle$  as well as the currents we end up with the basic equations (on the unitary side) of the three mentioned methods. In the following, we give three simple examples:

- **QCD sum rule for the  $B$  decay constant**

Using  $|Y\rangle = |B\rangle$  and  $|X\rangle = |0\rangle$  combined with the currents  $j_1 = j_2 = \bar{b}i\gamma_5 d$  and the definition of the  $B$  decay constant,

$$f_B m_B^2 = m_b \langle B | \bar{b}i\gamma_5 d | 0 \rangle, \quad (2.31)$$

we arrive after a trivial phase space integration at

$$\Pi(q^2) = \frac{f_B^2 m_B^4}{m_b^2 (m_B^2 - q^2)} + \int_{s_0}^\infty ds \frac{\rho(s)}{\pi (s - q^2)}. \quad (2.32)$$

- **Dispersive bounds for the  $B \rightarrow \pi$  form factor  $f_0(q^2)$**

The choice of  $|Y\rangle = |B\pi\rangle$ ,  $|X\rangle = |0\rangle$  and  $j_1 = j_2 = \bar{u}b$  yields

$$\Pi(q^2) > \int_0^\infty ds \frac{m_B^4 |m_B^2 - s|}{16\pi^2 s m_b^2 (s - q^2)} |f_0(s)|^2. \quad (2.33)$$

Here  $p$  and  $k$  are the momenta of the  $B$  and the  $\pi$ , respectively, and  $q^2 = (p - k)^2$  is the momentum transfer. Furthermore, we neglect the pion mass and drop the

## 2. Transition Form Factors

---

terms related to the continuous part, thus leading to the inequality in eq. (2.33).

- **Light Cone Sum Rule for the  $B \rightarrow \pi$  form factor  $f_0(q^2)$**

Alternatively, choosing  $|Y\rangle = |B\rangle$  and  $|X\rangle = |\pi\rangle$  as well as  $j_1 = \bar{u}i\gamma_5 b$   $j_2 = \bar{d}i\gamma_5 b$  leads to the starting point of the Light Cone Sum Rule for  $f_0(q^2)$ :

$$\Pi(q^2, p^2) = \frac{f_B m_B^4}{m_b^2 (p^2 - m_B^2)} f_0(q^2). \quad (2.34)$$

Here  $p$  and  $q$  are the momenta of the  $B$  and the  $\pi$ , respectively.

### 2.3.2 Short Distance and Light Cone Expansion

If the four-momentum squared transferred to the quarks is large, the integral in eq. (2.27) is dominated by small spatial distances and time intervals. In this case, the product of two currents can be expanded in a series of local operators  $O_k$ ,

$$\Pi(q^2) = \sum_{k=1}^{\infty} C_k(q^2) \langle O_k \rangle. \quad (2.35)$$

The short- and long-distance contributions are incorporated in the Wilson coefficients  $C_k(q^2)$  and the matrix elements of the operators  $\langle O_k \rangle$ , the so-called condensates, respectively. While the Wilson coefficients can be accessed perturbatively with techniques like position-space evaluation [15] or fixed gauge techniques [16], the condensates are non-perturbative and have to be evaluated with lattice QCD.

Alternatively, the correlation function can be calculated by expanding the quark currents near the light-cone  $x^2 = 0$ . This expansion is different from the local operator product expansion used before and incorporates summation of an infinite series of local operators. The correlator falls into a convolution of genuinely non-perturbative and universal light-cone hadron distribution amplitudes  $\phi^{(n)}$  and process-dependent amplitudes  $T_H^{(n)}$ , which, similarly to Wilson coefficients, can be calculated in perturbation theory:

$$\Pi(q^2) = \sum_n T_H^{(n)} \otimes \phi^{(n)}. \quad (2.36)$$

The sum runs over contributions with increasing twist  $n$  of the operators, which controls the relative size of contributions and is the analog of the dimension in the short distance expansion. The twist of an operator is given by the difference of its dimension and

spin. The “ $\otimes$ ” stands for an integration over the longitudinal momenta of the partons described by  $\phi^{(n)}$ .

### 2.3.3 Borel Transformation and Subtractions

In the framework of Light Cone Sum Rules and QCD sum rules, eqs. (2.35) and (2.32) are not used as they stand, but a Borel transformation is performed:

$$\Pi(M^2) = \lim_{\substack{-q^2, n \rightarrow \infty \\ -q^2/n = M^2}} \frac{(-q^2)^{(n+1)}}{n!} \left( \frac{d}{dq^2} \right)^n \Pi(q^2). \quad (2.37)$$

Here, the dependence on  $q^2$  is replaced by the dependence on the Borel-parameter  $M^2$ . This transformation enhances the ground-state  $B$  meson contribution to the dispersion-representation of  $\Pi(q^2)$ , while it damps the little known spectral function  $\rho(q^2)$  of excited and continuum states.

In the case of dispersive bounds, the so-called subtractions are more appropriate because they fit naturally in the structure of the Cauchy representation of  $\Pi(q^2)$ . As  $\Pi(q^2)$  is an analytic function, it satisfies the subtracted dispersion relation,

$$\chi(n) = \frac{1}{n!} \left. \frac{d^n \Pi(q^2)}{dq^{2n}} \right|_{q^2=0} = \frac{1}{\pi} \int_0^\infty dt \left. \frac{\text{Im} \Pi(t)}{(t - q^2)^{n+1}} \right|_{q^2=0}, \quad (2.38)$$

where the number of subtractions  $n$  is chosen to render the resulting function  $\chi(n)$  finite.

### 2.3.4 Resulting Information on the Form Factors

At the end of this section, we equate for each method the respective unitary representation and the results of the expansions (2.35) and (2.36).

- **QCD sum rule for the  $B$  decay constant**

Equating eq. (2.32) with an operator product expansion of the relevant correlator and subsequent application of the Borel transformation eq. (2.37), yields:

$$\sum_{k=1}^{\infty} C_k(M^2) \langle O_k \rangle = \frac{f_B^2 m_B^4}{m_b^2} \exp\left(-\frac{m_B^2}{M^2}\right) + \frac{1}{\pi} \int_{s_0}^{\infty} ds \rho(s) \exp\left(-\frac{s}{M^2}\right). \quad (2.39)$$

Solving this equation to  $f_B^2$ , truncating the expansion at a given order and using a lattice result for the condensates gives an estimate for the decay constant.

## 2. Transition Form Factors

---

- **Dispersive bounds for the  $B \rightarrow \pi$  form factor  $f_0(q^2)$**

Equating eq. (2.33) with an operator product expansion of the relevant correlator and subsequent application of the Borel transformation eq. (2.37), yields:

$$\sum_{k=1}^{\infty} \left( \frac{1}{n!} \frac{d^n C_k(q^2)}{dq^{2n}} \Big|_{q^2=0} \right) \langle O_k \rangle > \int_0^{\infty} ds \frac{m_B^4 |m_B^2 - s|}{16\pi^2 s m_b^2 (s - q^2)^n} |f_0(s)|^2. \quad (2.40)$$

Again, the left-hand side can be estimated using lattice results for the condensates and gives thus an upper bound on the form factors. The form factor parametrization in terms of a special series expansion, discussed in detail in chapter 5, allows to transform the bound in eq. (2.40) directly to the bound on the expansion coefficients.

- **Light Cone Sum Rule for the  $B \rightarrow \pi$  form factor  $f_0(q^2)$**  The result for the LCSR for the  $B \rightarrow \pi$  form factor is due to the additional momentum more difficult than the result of the dispersive bound, but works in principle very similar: The light cone expansion (2.37) gives combined with the eq. (2.35) (and after a Borel transformation) an estimate of the form factor. A detailed derivation can be found in ref. [13].

## 2.4 Lattice QCD versus Light Cone Sum Rules

Both methods start from first principles, but introduce additional approximations, which leads to systematic errors. These systematic errors are in the case of Lattice QCD for example discretization errors, chiral errors and quenching errors. In the case of LCSR the modeling of the continuum introduces systematic errors reflected in the choice of the continuum threshold and the Borel parameter.

The two methods are complementary with respect to the momentum transfer  $q^2$  between the initial and final state mesons: In Lattice QCD, results are more easily obtainable at high values of  $q^2$ , as discretization effects can only be controlled for small momenta of the final state in units of the Lattice spacing. This is in contrast to the LCSR method, which involves an expansion in inverse powers of the energy of the light daughter meson that is valid for low values of  $q^2$ .

## 2.5 Parametrization of Form Factors

In the preceding sections, the analytic structure of the form factors in  $q^2$  was not discussed. In this regard, it is useful to write down a similar dispersion relation for the form factors themselves, as it was done for the current correlator. Consider for example the form factor for the transition of  $B \rightarrow \pi$ :

$$f_{B\pi}^+(q^2) = \frac{f_{B^*} g_{B^* B\pi}}{m_{B^*}^2 - q^2} + \frac{1}{\pi} \int_{(m_B+m_\pi)^2}^{\infty} ds \frac{\text{Im} f_{B\pi}^+(q^2)}{s - q^2}. \quad (2.41)$$

Here  $f_B^* \sim \langle 0 | \bar{u} \gamma_\mu | B^* \rangle$  is the decay constant of the lowest resonance  $B^*$  and  $g_{B^* B\pi} \sim \langle B^* | B\pi \rangle$  its coupling to  $B$  and  $\pi$ . Different form factor parametrizations, which can be used to interpolate between the results for small and large momentum transfer, have been suggested in the literature; a good review can be found in [17]. A common assumption is that the integral has the shape of an effective pole leading to the following representation [18]:

$$f_{B\pi}^+(q^2) = \frac{r_1}{1 - q^2/m_{B^*}^2} + \frac{r_2}{1 - q^2/m_{B_{fit}}^2} \quad (2.42)$$

The parameters  $r_1$ ,  $r_2$  and  $m_{B_{fit}}$  have to be determined by one of the above discussed methods (e.g. LCSR), while the mass of the low-lying resonance  $m_{B^*}$  is usually extracted from experimental data [19] and/or theoretical estimates from heavy-quark/chiral symmetry [20]. A summary of the relevant resonance masses, which are used in the course of this work, is provided in table 2.1. Both the variations with different pole shapes and generalizations to  $N$  poles are discussed in the literature [18, 21, 22]. Another interesting parametrization is motivated by the relation between  $f_{B\pi}(q^2)$  and the elastic phase of the  $\pi B \rightarrow \pi B$  strong scattering amplitude [23, 24].

However, in chapter 5 we will concentrate on a parametrization advocated in refs. [5, 21, 25–27]. It has two main advantages: first, the parameters are organized as coefficients in a systematic expansion and, second, it is possible to impose bounds on these coefficients. These so-called dispersive bounds allow to obtain a third theoretical constraint in addition to Lattice QCD at high  $q^2$  and Light Cone Sum Rules at low  $q^2$ .

## 2. Transition Form Factors

---

**Table 2.1:** Summary of the masses of low-lying  $B_d$  and  $B_s$  resonances, using PDG values [28] and/or theoretical estimates from heavy-quark/chiral symmetry [20]. Notice that the mass values for  $(0^+, 1^+)$  predicted in [20] have not been confirmed experimentally, yet. Instead the PDG quotes “effective” resonances  $B_J^*(5698)$  and  $B_{s,J}^*(5853)$  with undetermined spin/parity.

Transition	$J^P$	Mass (GeV)	$J^P$	Mass (GeV)	Ref.
$b \rightarrow d$	$0^-$	5.28	$1^-$	5.33	[28]
	$0^+$	5.63	$1^+$	5.68	[20]
	$1^+$	5.72	$2^+$	5.75	[28]
$b \rightarrow s$	$0^-$	5.37	$1^-$	5.42	[28]
	$0^+$	5.72	$1^+$	5.77	[20]
	$1^+$	5.83	$2^+$	5.84	[28]



# Chapter 3

## $B \rightarrow K\nu\bar{\nu}$ , $B \rightarrow K^*\nu\bar{\nu}$ and $B \rightarrow X_s\nu\bar{\nu}$

### 3.1 Introduction

In this chapter we define the observables that can in principle be measured in  $B \rightarrow K^*(\rightarrow K\pi)\nu\bar{\nu}$ ,  $B \rightarrow K\nu\bar{\nu}$  and  $B \rightarrow X_s\nu\bar{\nu}$  and discuss their interplay originating from their common underlying quark level transition  $b \rightarrow s\nu\bar{\nu}$ . We review the present experimental status and present a numerical analysis of these decays, first within the SM and then beyond, both model-independently and within concrete extensions of the SM.

### 3.2 Effective Hamiltonian

The effective Hamiltonian for  $b \rightarrow s\nu\bar{\nu}$  transitions is described by

$$\mathcal{H}_{\text{eff}} = -\frac{4G_F}{\sqrt{2}}V_{tb}V_{ts}^*(C_L^\nu\mathcal{O}_L^\nu + C_R^\nu\mathcal{O}_R^\nu) + \text{h.c.}, \quad (3.1)$$

with the operators

$$\mathcal{O}_L^\nu = \frac{e^2}{16\pi^2}(\bar{s}\gamma_\mu P_L b)(\bar{\nu}\gamma^\mu(1 - \gamma_5)\nu), \quad \mathcal{O}_R^\nu = \frac{e^2}{16\pi^2}(\bar{s}\gamma_\mu P_R b)(\bar{\nu}\gamma^\mu(1 - \gamma_5)\nu). \quad (3.2)$$

Here,  $V_{tb}V_{ts}^*$  is the relevant combination of CKM matrix elements and  $e$  is the elementary charge.

In the SM, the Wilson coefficient  $C_R^\nu$  of the right-handed operator is negligible, while its left-handed counterpart  $C_L^\nu$  is dominated by  $Z$ -penguin and box diagrams involving

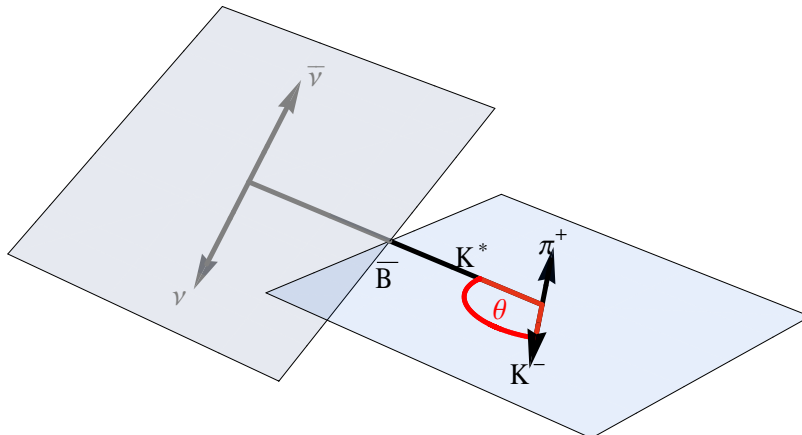


**Figure 3.1:** Kinematics of the decay  $B \rightarrow K^*(\rightarrow K\pi)\nu\bar{\nu}$

top quark exchanges. The SM calculation for  $C_L^\nu$  at the next-to-leading order in QCD can be found in ref. [29,30]. Combined with the latest top mass measurement from the Tevatron [31], we obtain the SM prediction

$$(C_L^\nu)_{\text{SM}} = -6.38 \pm 0.06 , \quad (3.3)$$

where the error is dominated by the top mass uncertainty. Since  $C_L^\nu$  is scale independent, the renormalization scale dependence enters  $C_L^\nu$  through the running top quark mass, which is however largely cancelled through next-to-leading order QCD corrections.

### 3.3 Observables

#### 3.3.1 $B \rightarrow K^*\nu\bar{\nu}$

While in the decay  $B \rightarrow K^*\nu\bar{\nu}$  the neutrinos escape the detector unmeasured, it is possible to extract information on the polarization of the  $K^*$  by including the subsequent decay of  $K^* \rightarrow K\pi$  in the analysis.

The starting point of an experimental analysis is the double differential decay distribution in the invariant mass of the neutrino-antineutrino pair  $q^2$  and the angle  $\theta$  between the  $K^*$  flight direction in the  $B$  rest frame and the  $K$  flight direction in the  $K\pi$  rest frame (see fig. 3.1).

The differential decay distribution can be efficiently and systematically expressed in

### 3. $B \rightarrow K^{(*)}\nu\nu$ and $B \rightarrow X_s\nu\nu$

---

terms of  $B \rightarrow K^*$  transversity amplitudes  $A_{\perp,\parallel,0}$ , which are given in terms of form factors  $\mathcal{B}_{V,i}(q^2)$  and Wilson coefficients as

$$\begin{aligned} A_0(q^2) &= N\mathcal{B}_{V,0}(q^2)(C_R^\nu - C_L^\nu), \\ A_\perp(q^2) &= N\mathcal{B}_{V,1}(q^2)(C_R^\nu + C_L^\nu), \\ A_\parallel(q^2) &= N\mathcal{B}_{V,2}(q^2)(C_R^\nu - C_L^\nu). \end{aligned}$$

Here  $N$  is a common pre-factor containing the Fermi constant  $G_F$ , the fine-structure constant  $\alpha$ , the  $B$  meson mass  $m_B$ , CKM matrix elements and phase space factors (for the definition of  $\lambda$  see, eq. (2.6) ),

$$N = \frac{G_F V_{tb} V_{ts}^* \alpha \lambda^{3/4}}{16\sqrt{3}\pi^{5/2} m_B^{3/2}}. \quad (3.4)$$

The subscript symbols,  $m = \perp, \parallel, 0$ , indicate the polarization of the  $K^*$ , respectively, and become clearer in the light of the connection of the matrix element and the transversity amplitudes:

$$A_m = \epsilon_{K^*}^{*\mu}(m) M_{\mu\nu}(B \rightarrow K^* V^*) \epsilon_{V^*}^{*\nu}(m). \quad (3.5)$$

By replacing the transversity amplitudes by the helicity amplitudes,

$$H_{\pm 1} = \frac{A_\parallel \pm A_\perp}{\sqrt{2}}, \quad H_0 = A_0, \quad (3.6)$$

it is possible to formulate the decay distribution in the following compact form:

$$\frac{d^2\Gamma(B \rightarrow K^*\nu\bar{\nu})}{dq^2 d\cos\theta} = \int_0^{2\pi} \left| \sum_{m=-1,0,1} H_m Y_m^1(\phi, \theta) \right|^2 d\phi. \quad (3.7)$$

Here the spherical harmonics<sup>1</sup>  $Y_{0,\pm}^1(\phi, \theta)$  describe the decay  $K^* \rightarrow K\pi$  and the integration over the angle  $\phi$  reflects the fact that no information on the dineutrino pair is available.

A necessary, but for the decay in question legitimate, assumption for the above factorization is the narrow-width approximation, which is implemented by the following

---

<sup>1</sup>The spherical harmonics enter via the  $D$  rotation matrices introduced in most quantum mechanics textbooks. For a review on the spin formalism in the context of particle physics see, ref. [32].

replacement of the squared propagator of the intermediate  $K^*$ :

$$\frac{1}{(k^2 - m_{K^*}^2)^2 + (m_{K^*}\Gamma_{K^*})^2} \xrightarrow{\Gamma_{K^*} \ll m_{K^*}} \frac{\pi}{m_{K^*}\Gamma_{K^*}} \delta(k^2 - m_{K^*}^2). \quad (3.8)$$

In this way, the form factors are independent of the  $K^*K\pi$  coupling  $g_{K^*K\pi}$  [33, 34], because it cancels between the vertex factor and the width

$$\Gamma_{K^*} = \frac{g_{K^*K\pi}^2}{48\pi} m_{K^*} \beta^3, \quad (3.9)$$

where

$$\beta = \frac{1}{m_{K^*}^2} [m_{K^*}^4 + m_K^4 + m_\pi^4 - 2(m_{K^*}^2 m_K^2 + m_K^2 m_\pi^2 + m_{K^*}^2 m_\pi^2)]^{1/2}. \quad (3.10)$$

Using the explicit expressions for the functions  $Y_{0,\pm}^1(\phi, \theta)$  in the  $K\pi$  restframe,

$$Y_{\pm}^1(\phi, \theta) = \mp \sqrt{\frac{3}{8\pi}} e^{\pm i\phi} \sin \theta ,$$

$$Y_0^1(\phi, \theta) = \sqrt{\frac{3}{4\pi}} \cos \theta ,$$

and integrating over  $\phi$ , the double differential spectrum can be written as:

$$\frac{d^2\Gamma(B \rightarrow K^* \nu \bar{\nu})}{dq^2 d\cos\theta} = \frac{3}{4} \frac{d\Gamma_T}{dq^2} \sin^2 \theta + \frac{3}{2} \frac{d\Gamma_L}{dq^2} \cos^2 \theta . \quad (3.11)$$

Here,  $d\Gamma_{L/T}/dq^2$  are the invariant mass spectra with a longitudinally/transversely polarized  $K^*$ . They are given in terms of transversity amplitudes as

$$\frac{d\Gamma_L}{dq^2} = 3|A_0|^2 , \quad \frac{d\Gamma_T}{dq^2} = 3(|A_{\perp}|^2 + |A_{\parallel}|^2) , \quad (3.12)$$

where the factor of 3 stems from the sum over neutrino flavors<sup>2</sup>. Instead of these two observables, we use combinations of these as observables in our analysis: The total differential spectrum,

$$\frac{d\Gamma}{dq^2} = \int_{-1}^1 d\cos\theta \frac{d^2\Gamma}{dq^2 d\cos\theta} = \frac{d\Gamma_L}{dq^2} + \frac{d\Gamma_T}{dq^2} = 3(|A_{\perp}|^2 + |A_{\parallel}|^2 + |A_0|^2) , \quad (3.13)$$

---

<sup>2</sup>Here we assume that the Wilson coefficients do not depend on the neutrino flavor, which is an excellent approximation in all the models we consider in sec. 3.6.

### 3. $B \rightarrow K^{(*)}\nu\nu$ and $B \rightarrow X_s\nu\nu$

---

and one of the  $K^*$  longitudinal and transverse polarization fractions  $F_{L,T}$ , defined as

$$F_{L,T} = \frac{d\Gamma_{L,T}/dq^2}{d\Gamma/dq^2}, \quad F_L = 1 - F_T. \quad (3.14)$$

This choice has two main advantages: First, the normalization of  $F_{L,T}$  on the total dineutrino spectrum  $d\Gamma/dq^2$  strongly reduces the hadronic uncertainties associated with the form factors as well as the parametric uncertainties associated with CKM elements. Second, in absence of right-handed currents ( $C_R^\nu = 0$ ), the dependence on the remaining Wilson coefficient  $C_L^\nu$  cancels out in  $F_L$ . In this case both observables become particularly simple:

$$\frac{d\Gamma}{dq^2} = 3N^2 C_L^\nu (\mathcal{B}_{V,0}^2 + \mathcal{B}_{V,1}^2 + \mathcal{B}_{V,2}^2), \quad (3.15)$$

$$F_L(q^2) = \frac{\mathcal{B}_{V,0}^2}{\mathcal{B}_{V,0}^2 + \mathcal{B}_{V,1}^2 + \mathcal{B}_{V,2}^2}. \quad (3.16)$$

Thus, in the case of vanishing right-handed currents,  $F_L$  is entirely determined by a ratio of form factors. The compact results illustrate explicitly our appropriate choice of form factors, since they naturally fit the problem and thus reduce the size of expressions. This becomes even more evident for the decay into charged leptons,  $B \rightarrow K^*\ell^+\ell^-$ , discussed in the next chapter.

Finally, note that the values of  $F_L$  at the kinematic endpoints are fixed to

$$F_L(0) = 1 \quad \text{and} \quad F_L((m_B - m_K^*)^2) = 1/3. \quad (3.17)$$

The first identity can be understood on the grounds of helicity conservation, allowing the  $B$  meson to decay only into a longitudinal  $K^*$ . The other kinematical endpoint at  $q^2 = (m_B - m_K^*)^2$  corresponds to the case of zero spatial momentum of the  $K^*$  in the  $B$  restframe. The absence of a preferential direction at this point explains the value of  $1/3$  as the ratio of the single longitudinal polarization state to the total number of 3 states<sup>3</sup>. The corresponding  $q^2$ -integrated observables are defined as

$$\langle F_{L,T} \rangle = \frac{\Gamma_{L,T}}{\Gamma}, \quad \text{where} \quad \Gamma_{(L,T)} = \int_0^{(m_B - m_{K^*})^2} dq^2 \frac{d\Gamma_{(L,T)}}{dq^2}. \quad (3.18)$$

---

<sup>3</sup>Alternatively, the values of  $F_L$  at the kinematic endpoints can be illustrated with eq. (3.16). At the lower endpoint all form factors but  $\mathcal{B}_{V,0}$  vanish and at the upper endpoint all form factors become equal, resulting in the values given in the text.

### 3.3.2 $B \rightarrow K\nu\bar{\nu}$

The dineutrino invariant mass distribution for the exclusive decay  $B \rightarrow K\nu\bar{\nu}$  can be written as<sup>4</sup> [36]

$$\frac{d\Gamma(B \rightarrow K\nu\bar{\nu})}{dq^2} = 3|N|^2 \mathcal{A}_{V,0}^2(q^2) |C_L^\nu + C_R^\nu|^2 . \quad (3.19)$$

We use the  $B \rightarrow K$  form factor  $\mathcal{A}_{V,0}(q^2)$  given in ref. [37]. As argued by the authors of [37], we assume that the maximum uncertainty is at  $q^2 = 0$  and, to be conservative, we adopt this uncertainty for the full  $q^2$  range. Note that the normalization factor  $N$  in eq. (3.19) can be obtained from the expression given in eq. (3.4) by replacing  $m_{K^*}$  by  $m_K$ .

### 3.3.3 $B \rightarrow X_s\nu\nu$

The inclusive decay  $B \rightarrow X_s\nu\bar{\nu}$  offers the theoretically most direct constraint on the Wilson coefficients  $C_L^\nu$  and  $C_R^\nu$  as its theoretical treatment is easier than for the exclusive decays. This is due to the absence of non-perturbative hadronic binding effects in the final state. The dineutrino invariant mass distribution can be written as

$$\begin{aligned} \frac{d\Gamma(B \rightarrow X_s\nu\bar{\nu})}{dq^2} &= 6N^2 \kappa(0) (|C_L^\nu|^2 + |C_R^\nu|^2) \\ &\times \left[ \frac{3q^2}{\lambda(m_b^2, m_s^2, q^2)} \left( m_b^2 + m_s^2 - q^2 - 4m_s m_b \frac{\text{Re}(C_L^\nu C_R^{\nu*})}{|C_L^\nu|^2 + |C_R^\nu|^2} \right) + 1 \right] , \quad (3.20) \end{aligned}$$

where  $m_s$  and  $m_b$  are the strange and the beauty quark masses, respectively,  $\kappa(0) = 0.83$  represents the QCD correction to the  $b \rightarrow s\nu\bar{\nu}$  matrix element [38–40] and the factor  $N$  is related to the above defined normalization constant (3.4) by the obvious replacement of the  $B$  meson mass by the  $b$  quark mass and  $K^*$  meson mass by the  $s$  quark mass. For the numerical evaluation we also include non-perturbative  $1/m_b^2$  corrections to the matrix element of the operators given in [38, 41] with the HQET parameters taken from [42].

In previous analyses of  $B \rightarrow X_s\nu\bar{\nu}$ , similarly to the practice in the calculation of  $\text{BR}(B \rightarrow X_s\gamma)$  [43], the common approach to reduce the theoretical uncertainties was to normalize eq. (3.20) to the inclusive semileptonic decay rate  $\Gamma(B \rightarrow X_c e \bar{\nu}_e)$ . This normalization avoids the overall dependence on  $m_b$  in the normalization  $N$ . However, in this approach the  $m_b$  dependence does not cancel fully, leaving an additional uncertainty

---

<sup>4</sup>The charged decay  $B^+ \rightarrow K^+\nu\bar{\nu}$  mode receives an additional background from the process  $B^+ \rightarrow K^+\nu\bar{\nu}$  with a resonant  $\tau$ . The branching ratio amounts to roughly one fourth of the branching ratio of  $B^+ \rightarrow K^+\nu\bar{\nu}$ . Further details can be found in [35]

### 3. $B \rightarrow K^{(*)}\nu\nu$ and $B \rightarrow X_s\nu\nu$

---

Observable	SM prediction	Experiment
$\text{BR}(B \rightarrow K^*\nu\bar{\nu})$	$(6.8_{-1.1}^{+1.0}) \times 10^{-6}$	$< 80 \times 10^{-6}$ [47]
$\text{BR}(B^+ \rightarrow K^+\nu\bar{\nu})$	$(4.5 \pm 0.7) \times 10^{-6}$	$< 14 \times 10^{-6}$ [48]
$\text{BR}(B \rightarrow X_s\nu\bar{\nu})$	$(2.7 \pm 0.2) \times 10^{-5}$	$< 64 \times 10^{-5}$ [49]
$\langle F_L(B \rightarrow K^*\nu\bar{\nu}) \rangle$	$0.54 \pm 0.01$	–

**Table 3.1:** SM predictions and experimental bounds (all at the 90% C.L.) for the four  $b \rightarrow s\nu\bar{\nu}$  observables.

introduced through the dependence of the semileptonic phase space factor on the charm quark mass.

As an alternative to this approach we abandon this normalization in favor of a direct use of eq. (3.20) in combination with the  $b$  quark mass in the 1S scheme. This approach reduces the uncertainty of  $m_b$  to about 1% [42, 44–46] and allows to reduce the estimated uncertainty of the integrated branching ratio to less than 10%. This constitutes a considerable improvement relative to the conventional approach.

## 3.4 Experimental Bounds and Standard Model Predictions

It should be stressed that neither the inclusive nor the exclusive decay modes have been observed in experiment so far. However, experimental upper bounds on the branching ratios have been set by the BaBar, Belle and ALEPH collaborations. We summarize them together with our predictions for their SM values in table 3.1. In fig. 3.2 we show our SM predictions for the differential branching ratios of all three decays and for  $F_L(q^2)$ .

Note that we omit the  $O(1/m_b^2)$  corrections to the inclusive dineutrino mass spectrum in fig. 3.2, since they are well known to become singular at the kinematical endpoint. In contrast, we keep it for the integrated branching ratio, as the integration yields a finite result.

Of particular interest is the size of the uncertainties reflected by the intervals in table 3.1 and the bands in fig. 3.2. While the inclusive and the exclusive decays both suffer from errors coming from CKM elements, as listed in table 3.2, and an uncertainty in the SM Wilson coefficient as given in eq. (3.3), the origin of the remaining uncertainties is rather diverse. For the inclusive decay, the uncertainty is dominated by the theory error

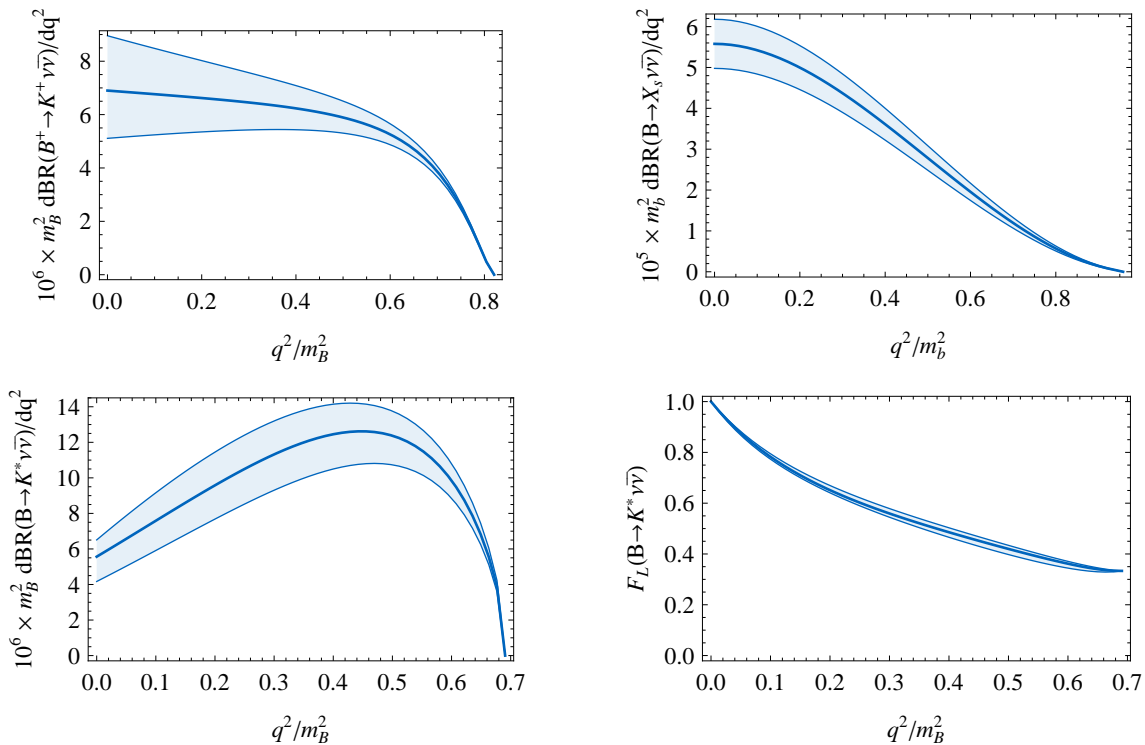


**Figure 3.2:** Dependence of the four  $b \rightarrow s\nu\bar{\nu}$  observables on the normalized neutrino invariant masses squared  $q^2$  within the SM. The error bands reflect the theoretical uncertainties. In the lower plots, the black dashed lines and dotted red lines are the results based on the form factor sets  $B$  and  $C$ , respectively. (See the text for more details.)

of  $m_b^{1S}$ . These errors together with the additional, less dominant errors of  $\lambda_{1,2}$  are given in table 3.2. To be conservative, we assume an additional uncertainty of the inclusive branching ratio of 5% to account for neglected higher order corrections. We account an additional error of 10% for the neglected  $1/m_b^2$  correction in the differential observable of the inclusive decay. These errors of the form factors of the decay  $B \rightarrow K\nu\bar{\nu}$  were already discussed in section 3.3.2. The form factor errors in  $B \rightarrow K^*\nu\bar{\nu}$  are relatively small due to the correlation of the form factors.

### 3.5 Model-independent Analysis of New Physics Effects

In the following section, we discuss the three decays in the context of three effective theories. This analysis is model-independent in the sense that the effective theories studied here cover certain classes of specific NP models as special cases. First, we

### 3. $B \rightarrow K^{(*)}\nu\nu$ and $B \rightarrow X_s\nu\nu$

Parameter	Value	Ref.	Parameter	Value	Ref.
$m_b^{1S}$	$(4.68 \pm 0.03)$ GeV	[42, 46]	$\lambda$	0.2255(7)	[50]
$m_s(2 \text{ GeV})$	0.1 GeV	[19]	$ V_{cb} $	$(4.13 \pm 0.05) \times 10^{-2}$	[51]
$m_t(m_t)$	$(162.3 \pm 1.2)$ GeV	[31]	$\bar{\rho}$	$0.154 \pm 0.022$	[51]
$\tau_{B^+}$	1.638 ps	[19]	$\bar{\eta}$	$0.342 \pm 0.014$	[51]
$\tau_{B^0}$	1.530 ps	[19]	$\lambda_1$	$(-0.27 \pm 0.04)$ GeV <sup>2</sup>	[42]
			$\lambda_2$	$(0.12 \pm 0.01)$ GeV <sup>2</sup>	[19]

**Table 3.2:** Parameters used in the numerical analysis.  $\lambda_{1,2}$  are the HQET parameters needed for the evaluation of the  $\Lambda^2/m_b^2$  corrections to  $\text{BR}(B \rightarrow X_s\nu\bar{\nu})$  [38].

analyze the dependence of the observables on the Wilson coefficients themselves. In the next step we assume that physics beyond the SM modifies only the  $\bar{b}sZ$  coupling and analyze the implications of this assumption. In the last framework, we assume that a light additional scalar singlet under the SM gauge group is coupled via an effective vertex to the  $b \rightarrow s$  current and thus enters the observables as missing energy.

#### 3.5.1 Model-independent constraints on Wilson coefficients

The two complex Wilson coefficients  $C_L^\nu$  and  $C_R^\nu$ , giving rise to three different  $b \rightarrow s\nu\bar{\nu}$  decays, enter the four observables only through two combinations<sup>5</sup>. These real quantities are [38, 52]

$$\epsilon = \frac{\sqrt{|C_L^\nu|^2 + |C_R^\nu|^2}}{|(C_L^\nu)^{\text{SM}}|}, \quad \text{and} \quad \eta = \frac{-\text{Re}(C_L^\nu C_R^{\nu*})}{|C_L^\nu|^2 + |C_R^\nu|^2}. \quad (3.21)$$

They are normalized such that  $\eta$  lies in the range  $[-\frac{1}{2}, \frac{1}{2}]$  and the SM corresponds to  $(\epsilon, \eta) = (1, 0)$ . The integrated observables discussed in section 3.3.1 and expressed in terms of  $\epsilon$  and  $\eta$  as well as combined with the numerical values of the input parameter and form factors read as follows:

$$\text{BR}(B \rightarrow K^*\nu\bar{\nu}) = \text{BR}(B \rightarrow K^*\nu\bar{\nu})_{\text{SM}}(1 + 1.31\eta)\epsilon^2, \quad (3.22)$$

$$\text{BR}(B \rightarrow K\nu\bar{\nu}) = \text{BR}(B \rightarrow K\nu\bar{\nu})_{\text{SM}}(1 - 2\eta)\epsilon^2, \quad (3.23)$$

$$\text{BR}(B \rightarrow X_s\nu\bar{\nu}) = \text{BR}(B \rightarrow X_s\nu\bar{\nu})_{\text{SM}}(1 + 0.09\eta)\epsilon^2, \quad (3.24)$$

$$\langle F_L \rangle = \langle F_L \rangle_{\text{SM}} \frac{(1 + 2\eta)}{(1 + 1.31\eta)}. \quad (3.25)$$

<sup>5</sup>The situation is very similar to the muon decay  $\mu^+ \rightarrow e^+\nu_e\bar{\mu}_e$ , where a broader set of Wilson coefficients enters the observables via four Michel parameters.

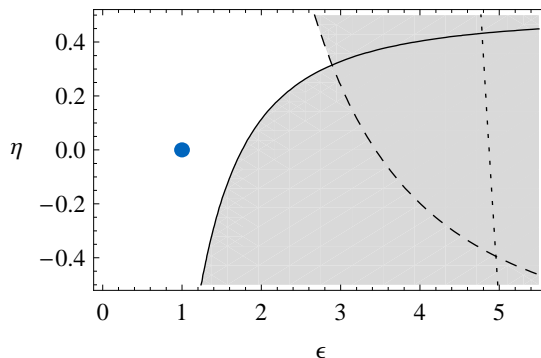


**Figure 3.3:** Existing experimental constraints on  $\epsilon$  and  $\eta$ . Dashed line: constraint from  $\text{BR}(B \rightarrow K^* \nu \bar{\nu})$ , solid line: constraint from  $\text{BR}(B \rightarrow K \nu \bar{\nu})$ , dotted line: constraint from  $\text{BR}(B \rightarrow X_s \nu \bar{\nu})$ . The shaded area is ruled out experimentally at the 90% confidence level. The blue circle represents the SM point.

These equations can be considered as the fundamental set of relations connecting the experiment and the theory of the decays in question: On the one hand  $\epsilon$  and  $\eta$  can be calculated in any model which has the low energy operator structure of the effective theory (3.1) by means of eq. (3.21) and can be used in eqs. (3.22-3.25). On the other hand, a measurement of the observables translates directly into constraints on  $\epsilon$  and  $\eta$ . Since  $\epsilon$  and  $\eta$  are real quantities, it is possible to visualize these experimental results in a two dimensional plot. We show this kind of plot in fig. 3.3 for the experimental bounds given in table 3.1 and note that the exclusive decays are presently more constraining than the inclusive one. To evaluate the theoretical cleanliness of the various observables, we show in fig. 3.4 the combined constraints after hypothetical measurements with infinite precision, assuming the SM and a hypothetical NP example.

A special role is played by the observable  $\langle F_L \rangle$ : since it depends only on  $\eta$ , cf. eq. (3.25), it leads to a horizontal line in the  $\epsilon$ - $\eta$  plane. In the right-hand panel of fig. 3.5, we show the value of  $\langle F_L \rangle$  as a function of  $\eta$ . Especially for negative  $\eta$ ,  $\langle F_L \rangle$  constitutes a very clean observable to probe the value of  $\eta$ .

As mentioned in section 3.3.1,  $F_L$  is universal for all models where  $C_R^\nu = 0$  and consequently  $\eta = 0$ , in the SM and those models with minimal flavor violation (MFV) [53–55]. Every experimentally observed deviation from this curve clearly signals the presence of right-handed currents. In the left-hand panel of fig. 3.5, we plot  $F_L(q^2)$  in the kinematically allowed range of  $q^2$  for several values of  $\eta$ . The blue curve is the universal curve for  $\eta = 0$ .

### 3. $B \rightarrow K^{(*)}\nu\nu$ and $B \rightarrow X_s\nu\nu$

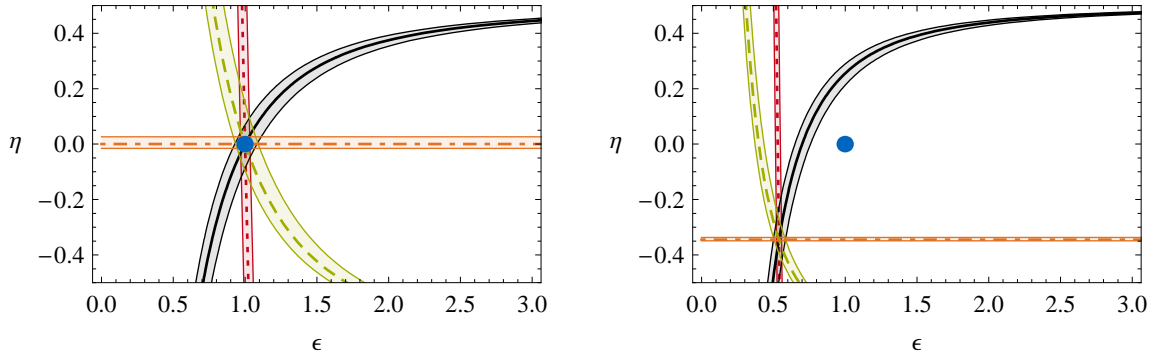


**Figure 3.4:** Hypothetical constraints on the  $\epsilon$ - $\eta$ -plane, assuming all four observables have been measured with infinite precision. The error bands reflect the theoretical uncertainty as described in section 3.3.1. The green band (dashed line) represents  $\text{BR}(B \rightarrow K^*\nu\bar{\nu})$ , the black band (solid line)  $\text{BR}(B \rightarrow K\nu\bar{\nu})$ , the red band (dotted line)  $\text{BR}(B \rightarrow X_s\nu\bar{\nu})$  and the orange band (dot-dashed line)  $\langle F_L \rangle$ . Left: SM values for the Wilson coefficients, right: assuming  $C_L^\nu = 0.5(C_L^\nu)^{\text{SM}}$  and  $C_R^\nu = 0.2(C_L^\nu)^{\text{SM}}$ . The blue circle represents the SM point.

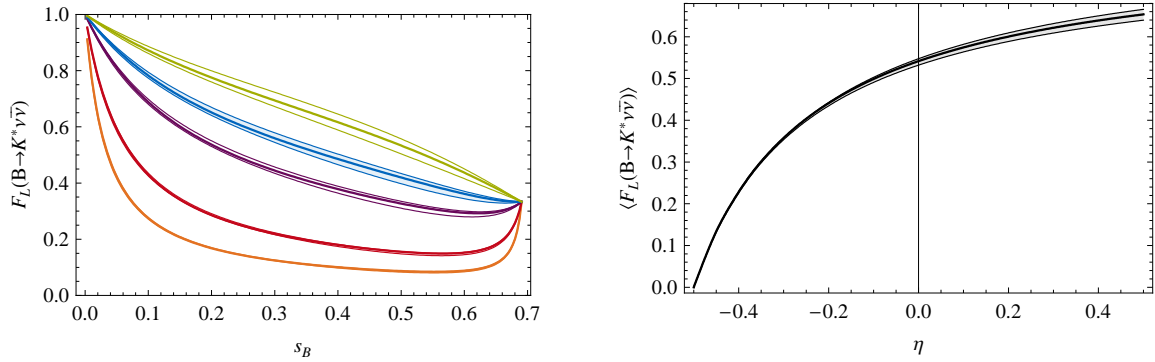


**Figure 3.5:** Left:  $F_L(q^2)$  for different values of  $\eta$ , from top to bottom:  $\eta = 0.5, 0, -0.2, -0.4, -0.45$ . Right: Dependence of the  $q^2$ -integrated  $\langle F_L \rangle$  on  $\eta$ .

#### 3.5.2 Modified $Z$ penguins

In many models beyond the SM, NP effects in the Wilson coefficients  $C_{L,R}^\nu$  are dominated by  $Z$  penguins. This can be discussed model-independently by assuming an effective flavor violating  $\bar{b}sZ$  coupling [56], which will not only modify the Wilson coefficients  $C_{L,R}^\nu$ , but also the Wilson coefficients  $C_{9,10}^{(\prime)}$  of the semi-leptonic operators governing  $b \rightarrow s\ell^+\ell^-$  transitions. Therefore, interesting correlations between these processes and the  $b \rightarrow s\nu\bar{\nu}$  transitions are to be expected in this scenario. Note that a detailed discussion of the weak hamiltonian for  $b \rightarrow s\ell^+\ell^-$ , including the definition of the Wilson coefficients  $C_{9,10}^{(\prime)}$ , is given in chapter 4.

The effective Lagrangian [56] describing such a framework is given by

$$\mathcal{L}_{\text{eff}}^{\bar{b}sZ} = \frac{G_F}{\sqrt{2}} \frac{e}{\pi^2} m_Z^2 c_w s_w V_{tb}^* V_{ts} Z^\mu (Z_L \bar{b} \gamma_\mu P_L s + Z_R \bar{b} \gamma_\mu P_R s) , \quad (3.26)$$

with  $s_w = \sin \theta_w$  and  $c_w = \cos \theta_w$ . In the SM, the right-handed coupling is negligible, while  $Z_L = C_0(x_t)/s_w^2$ . The function  $C_0$  can be found e.g. in [39]. In models with MFV,  $Z_L$  is a real function of the model parameters and  $Z_R$  is strongly suppressed, while in general NP models  $Z_L$  and  $Z_R$  can be arbitrary complex functions.

A modification of the type (3.26) affects other flavor changing transitions involving  $Z$  penguins such as  $B \rightarrow X_s \ell^+ \ell^-$ ,  $B_s \rightarrow \mu^+ \mu^-$  and  $B_s$ - $\bar{B}_s$  mixing. The impact of NP effects in the  $\bar{b}sZ$  couplings  $Z_{L,R}$  on the Wilson coefficients contributing to those processes is given by:

$$C_L^\nu = (C_L^\nu)^{\text{SM}} - Z_L^{\text{NP}} , \quad C_R^\nu = -Z_R , \quad (3.27)$$

$$C_{10} = C_{10}^{\text{SM}} - Z_L^{\text{NP}} , \quad C'_{10} = -Z_R , \quad (3.28)$$

$$C_9 = C_9^{\text{SM}} + Z_L^{\text{NP}} (1 - 4s_w^2) , \quad C'_9 = Z_R (1 - 4s_w^2) . \quad (3.29)$$

The contributions to  $C_9^{(\prime)}$  are strongly suppressed by the small vector coupling of the  $Z$  to charged leptons  $(1 - 4s_w^2) \approx 0.08$ .

In the following, we compile the constraints imposed by the experimental information on the couplings  $Z_L$  and  $Z_R$ :

- The experimental branching ratio of the inclusive decay  $B \rightarrow X_s \ell^+ \ell^-$  in the low- $q^2$  region,  $1 \text{ GeV}^2 < q^2 < 6 \text{ GeV}^2$  [57, 58],

$$\text{BR}(B \rightarrow X_s \ell^+ \ell^-)_{\text{exp.}} = (1.60 \pm 0.51) \times 10^{-6} , \quad (3.30)$$

can be translated into a bound on the flavor-changing  $Z$  couplings,

$$4.3 < |Z_L|^2 + |Z_R|^2 < 28.8 , \quad (3.31)$$

at the  $1\sigma$  level.

- The experimental upper bound on the branching ratio of  $B_s \rightarrow \mu^+ \mu^-$  [59],

$$\text{BR}(B_s \rightarrow \mu^+ \mu^-)_{\text{exp.}} < 5.8 \times 10^{-8} \text{ at } 95\% \text{ C.L.} , \quad (3.32)$$

### 3. $B \rightarrow K^{(*)}\nu\nu$ and $B \rightarrow X_s\nu\nu$

---

leads to

$$|Z_L - Z_R|^2 < 261 . \quad (3.33)$$

Here we assume that the scalar or pseudoscalar operator contributions to  $B_s \rightarrow \mu^+\mu^-$  are negligible.

- The mass difference in  $B_s$ - $\bar{B}_s$  mixing has been measured to be [60]

$$(\Delta M_s)_{\text{exp.}} = (17.77 \pm 0.12) \text{ ps}^{-1} . \quad (3.34)$$

$Z_L$  and  $Z_R$  contribute to the mixing via double  $Z$  penguin diagrams, which give an additional term to the amplitude:

$$\frac{\langle B_s | \mathcal{H} | \bar{B}_s \rangle^{\bar{b}sZ}}{\langle B_s | \mathcal{H} | \bar{B}_s \rangle^{\text{SM}}} = \frac{4\alpha_s^2}{\pi S_0(x_t)} (Z_L^2 + xZ_L Z_R + Z_R^2) , \quad (3.35)$$

where the function  $S_0$  and details about the evaluation of the hadronic parameter  $x$  can be e.g. found in [61]. The amplitude is usually parametrized as

$$\langle B_s | \mathcal{H} | \bar{B}_s \rangle = \frac{\Delta M_s}{2} e^{2i(\phi_{B_s} + \beta_s)} . \quad (3.36)$$

However, the theory prediction is afflicted with an uncertainty of roughly 30% due to uncertainties in hadronic parameters. While the  $B_s$  mixing phase predicted by the SM is tiny,  $\beta_s \approx 1^\circ$ , recent Tevatron data seem to indicate the presence of a sizable phase  $\phi_{B_s}$  [62–66].

In principle, large complex  $\bar{b}sZ$  couplings  $Z_{L,R}$  could give rise to a such a phase. However, taking into account the constraint in eq. (3.31), the double penguin contribution is too small to generate a sizable phase.

An analogous representation through a minimal set of two independent parameters for  $Z_L$  and  $Z_R$ , as it was possible for  $C_L^\nu$  and  $C_R^\nu$ , is impossible due to the fact that  $B_s$  mixing depends on an additional independent combination of  $Z_L$  and  $Z_R$ . However, it is possible to visualize the constraints from  $B \rightarrow X_s \ell^+ \ell^-$ ,  $B_s \rightarrow \mu^+ \mu^-$  and from  $B_s$  mixing for the case of vanishing  $Z_R$ , as shown in fig. 3.6. In the general case of nonzero and complex  $Z_L$  and  $Z_R$ , the correlation is more complicated (e.g., for  $Z_L = Z_R$  the constraint from  $B_s \rightarrow \mu^+ \mu^-$  disappears). However, we find that it is never possible to bring the stringent constraint from  $B \rightarrow X_s \ell^+ \ell^-$  into agreement with a large  $B_s$  mixing phase.

In fig. 3.7, we present the correlation between the three  $b \rightarrow s\nu\bar{\nu}$  branching ratios

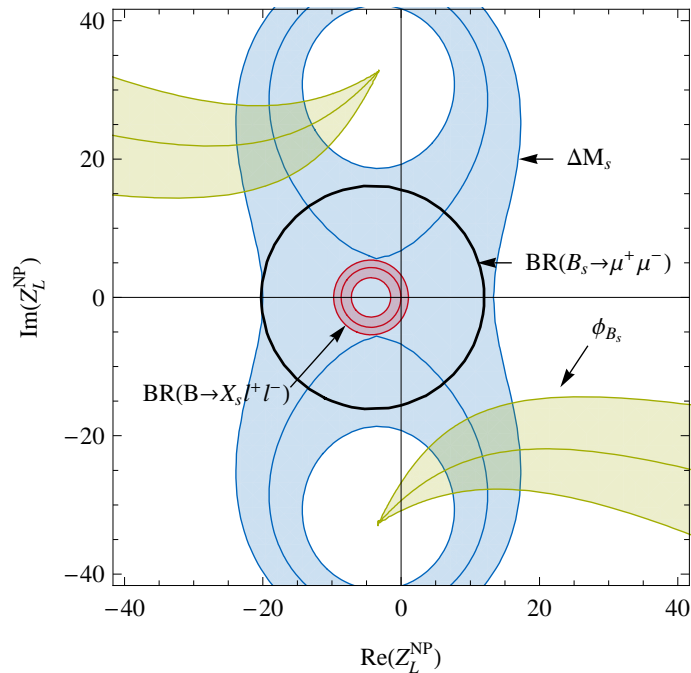


**Figure 3.6:** Constraints on the real and imaginary parts of  $Z_L^{\text{NP}}$  coming from  $\Delta M_s$  (blue, assuming 30% theory uncertainty),  $\text{BR}(B \rightarrow X_s \ell^+ \ell^-)$  (red) and  $\text{BR}(B_s \rightarrow \mu^+ \mu^-)$  (black) assuming  $Z_R = 0$ . The green lines correspond to values of the  $B_s$  mixing phase  $\phi_{B_s} = -11^\circ$ ,  $-19^\circ$  and  $-27^\circ$ , respectively [62].

and  $\text{BR}(B \rightarrow X_s \ell^+ \ell^-)$ . Assuming  $Z_R = 0$  and real  $Z_L$ , which holds in MFV models, there are clear correlations, indicated as black curves, between the neutrino modes and the charged lepton mode. In the general case of arbitrary and complex  $Z_{L,R}$ , the entire shaded areas are accessible. However, it is interesting to note that, in all three  $b \rightarrow s \nu \bar{\nu}$  decay modes, an enhancement of the branching ratio by more than a factor of two with respect to the SM is excluded by the measurement of  $\text{BR}(B \rightarrow X_s \ell^+ \ell^-)$  in eq. (3.30). By construction, this statement is valid for all models in which NP contributions to  $b \rightarrow s \nu \bar{\nu}$  and  $b \rightarrow s \ell^+ \ell^-$  processes enter dominantly through flavor-changing  $Z$  penguins.

For example large enhancements are possible in  $Z'$  models, where the  $B \rightarrow X_s \ell^+ \ell^-$  constrained can be circumvented by an appropriate choice of  $U(1)'$  charges (see also section 4.6.1).

### 3.5.3 Decay to invisible scalars

The last model independent framework we consider differs structurally from the previous ones, since we do not only assume the modification of the high energy physics with respect to the SM, but assume also an extension of the low energy particle content of the SM.

### 3. $B \rightarrow K^{(*)}\nu\nu$ and $B \rightarrow X_s\nu\nu$

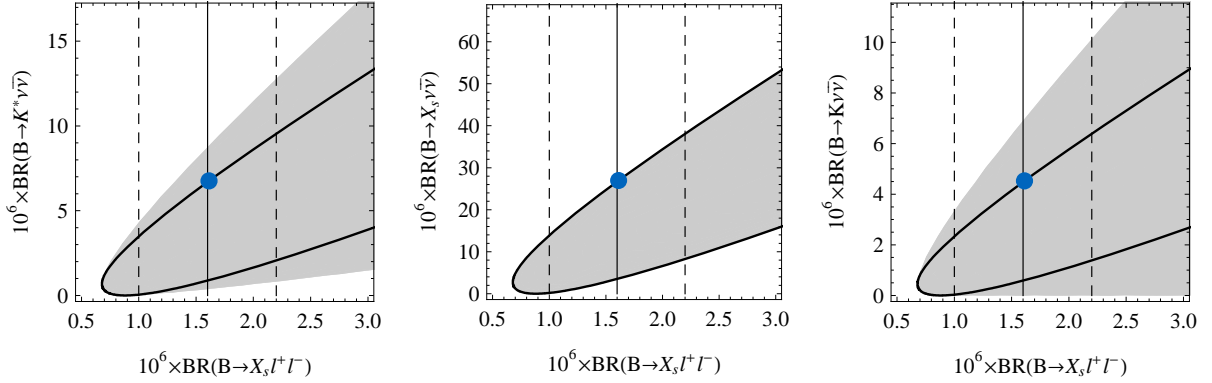


**Figure 3.7:** Correlations between  $b \rightarrow s\nu\bar{\nu}$  branching ratios and  $\text{BR}(B \rightarrow X_s\ell^+\ell^-)$ . The black curves correspond to  $Z_R = 0$  and real  $Z_L$ ; The shaded areas are accessible for arbitrary  $Z_{L,R}$ ; The blue dots represent the SM. The solid and dashed vertical lines correspond to the experimental central value and  $1\sigma$  error, respectively, of  $\text{BR}(B \rightarrow X_s\ell^+\ell^-)$ .

We assume the existence of a light gauge singlet scalar  $S$  with mass  $m_S < m_b/2$  which is coupled to the  $b \rightarrow s$  current via an effective coupling. Effects of these scalars superpose with the SM contribution to the  $b \rightarrow s\nu\bar{\nu}$  observables, since the two final states could not be distinguished experimentally. The effective theory approach covers, for instance, specific NP models of dark matter [67].

The effective Hamiltonian describing the flavor-changing quark-scalar interaction can be written as

$$\mathcal{H}_{eff} = C_L^S \frac{m_b}{2} (\bar{s}P_L b) S^2 + C_R^S \frac{m_b}{2} (\bar{s}P_R b) S^2. \quad (3.37)$$

The mass of the scalar particle  $m_S$  enters, in addition to the two Wilson coefficients  $C_L^S$  and  $C_R^S$ , the observables as third parameter through the phase space integration.

The differential decay amplitude for the inclusive decay is in this framework given by

$$\frac{d\Gamma(B \rightarrow X_s \cancel{f})}{dq^2} = \frac{d\Gamma(B \rightarrow X_s \nu\bar{\nu})}{dq^2} + \frac{d\Gamma(B \rightarrow X_s SS)}{dq^2}, \quad (3.38)$$

and by the corresponding sum for the exclusive decays. The differential decay widths of the scalar modes read

$$\frac{d^2\Gamma(B \rightarrow K^*(\rightarrow K\pi)SS)}{dq^2 d\cos\theta} = \frac{3}{2} N_S(m_B, m_K^*) \mathcal{B}_{V,t}^2(q^2) |C_L^S - C_R^S|^2 \cos^2\theta, \quad (3.39)$$

$$\frac{d\Gamma(B \rightarrow KSS)}{dq^2} = N_S(m_B, m_K) \mathcal{A}_{V,t}^2(q^2) |C_L^S + C_R^S|^2, \quad (3.40)$$

$$\frac{d\Gamma(B \rightarrow X_s SS)}{dq^2} = N_S(m_b, m_s)(|C_R^S|^2 + |C_L^S|^2) \quad (3.41)$$

$$\times \frac{m_B^4}{\lambda} \left[ \frac{m_b^2 + m_s^2 - q^2}{4} - m_b m_s \frac{\text{Re}(C_L^S C_R^{S*})}{|C_R^S|^2 + |C_L^S|^2} \right]. \quad (3.42)$$

Here  $N_S(m_1, m_2)$  is a kinematic function,

$$N_S(m_1, m_2) = \frac{1}{2^{11} m_1} \left( 1 - \frac{4m_S^2}{q^2} \right)^{1/2} \left( \frac{\lambda(m_1^2, m_2^2, q^2)}{\pi^2} \right)^{3/2}, \quad (3.43)$$

and  $\mathcal{B}_{V,t}(q^2)$  and  $\mathcal{A}_{V,t}(q^2)$  are the time-like  $B \rightarrow K^*$  and  $B \rightarrow K$  form factors, respectively. We obtain  $\mathcal{B}_{V,t}(q^2)$  by the procedure described in section (2.4), while  $\mathcal{A}_{V,t}(q^2)$  is taken from ref. [37].

The observable  $F_L$ , as it is extracted from the angular distribution of  $B \rightarrow K^*(\rightarrow K\pi)\not{E}$  according to the formula (cf. eq. (3.11))

$$\frac{d^2\Gamma}{dq^2 d\cos\theta} \Big/ \frac{d\Gamma}{dq^2} = \frac{3}{4}(1 - F_L) \sin^2\theta + \frac{3}{2}F_L \cos^2\theta, \quad (3.44)$$

is modified according to

$$F_L(B \rightarrow K^* \not{E}) = \frac{d\Gamma_L(B \rightarrow K^* \nu \bar{\nu})/dq^2 + d\Gamma(B \rightarrow K^* SS)/dq^2}{d\Gamma(B \rightarrow K^* \nu \bar{\nu})/dq^2 + d\Gamma(B \rightarrow K^* SS)/dq^2}, \quad (3.45)$$

since the  $K^*$  is always produced with longitudinal polarization in the  $B \rightarrow K^* SS$  decay, which is also the reason for the factor of  $\cos^2\theta$  in eq. (3.39).

The superposition of the two decay modes with different but experimentally indistinguishable final states leads to characteristic edges at the production threshold  $q^2 = m_S^2/4$  of two scalars. In fig. 3.8, we show the differential branching ratios of all three decays as well as  $F_L(q^2)$  for an exemplary scenario which is compatible with experimental upper bounds on the integrated branching ratios given in table 3.1.

Since the transition  $b \rightarrow sSS$  is partly induced by operators beyond the set given in eq. (3.1), the direct relations of observables to the parameters  $\epsilon$  and  $\eta$  (eqs. (3.22)–(3.25)) are no longer valid. An attempt to nevertheless extract  $\epsilon$  and  $\eta$  from the measurements leads to an inconsistency, signaled by the absence of an intersection point of the four bands. This situation is made explicit in fig. 3.9. Inversion of this argument in this specific case is even more interesting: incompatibility of the measurements in the  $\epsilon$ - $\eta$ -plane indicates the presence of operators beyond those in eq. (3.1).

### 3. $B \rightarrow K^{(*)}\nu\nu$ and $B \rightarrow X_s\nu\nu$

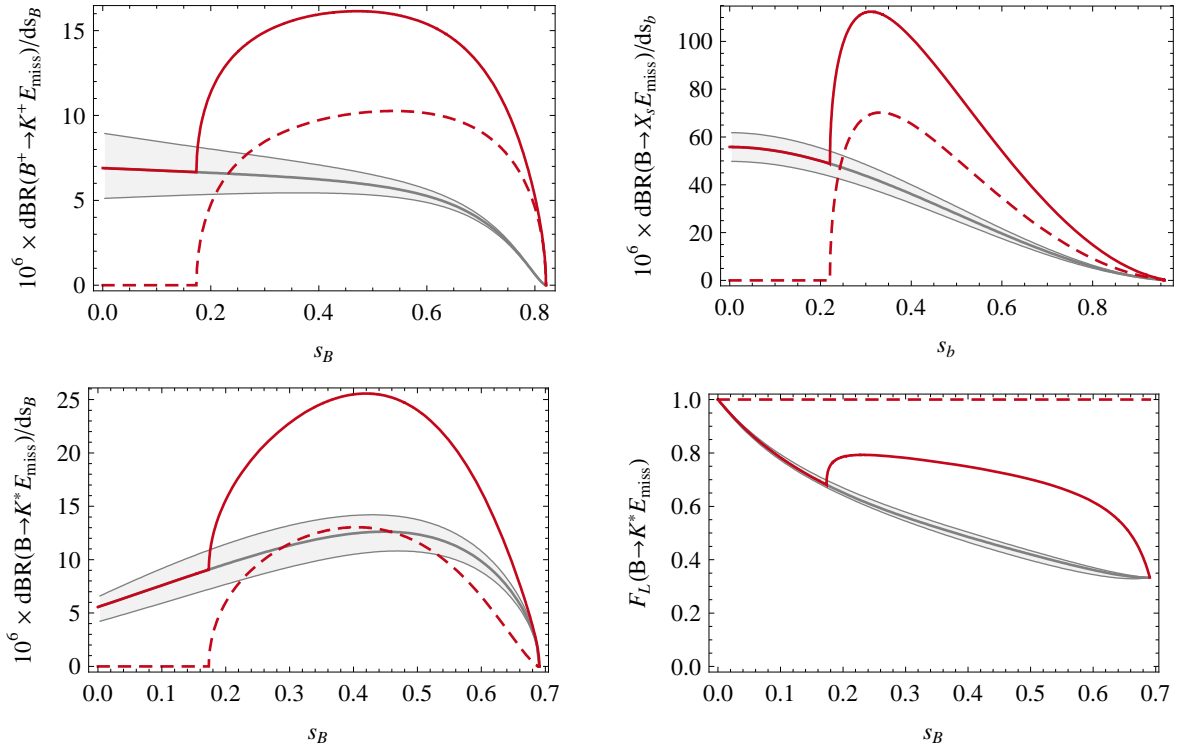


**Figure 3.8:** Dependence of the four observables on the normalized missing energy invariant mass squared in a scenario in which SM-like  $b \rightarrow s\nu\bar{\nu}$  processes overlap with  $b \rightarrow sSS$  decays. The parameters chosen are  $m_S = 1.1$  GeV,  $C_L^S = 0$  and  $C_R^S = 2.8 \times 10^{-8}$  GeV $^{-2}$ . The grey curves show the pure  $b \rightarrow s\nu\bar{\nu}$  (i.e. SM) contribution with theoretical uncertainties, the red dashed curves the pure  $b \rightarrow sSS$  contribution and the red solid curves the resulting combination.

## 3.6 Effects in specific New Physics Models

### 3.6.1 Heavy $Z'$

A popular extension of the SM is to include a heavy  $Z'$  gauge boson of an additional  $U(1)'$  gauge symmetry. This field is coupled to the relevant SM particles as

$$\mathcal{L}^{\bar{b}sZ'} = \frac{G_F}{\sqrt{2}} \frac{e}{\pi^2} m_{Z'}^2 c_w s_w V_{tb}^* V_{ts} Z'^{\mu} (Z'_L \bar{b} \gamma_{\mu} P_L s + Z'_R \bar{b} \gamma_{\mu} P_R s) . \quad (3.46)$$

While these couplings can arise at tree level (as fundamental vertices) in the case of generation non-universal  $U(1)'$  charges of the quarks [68], they can also be induced by loop effects of particles charged under the  $U(1)'$ . The presence of such couplings gives

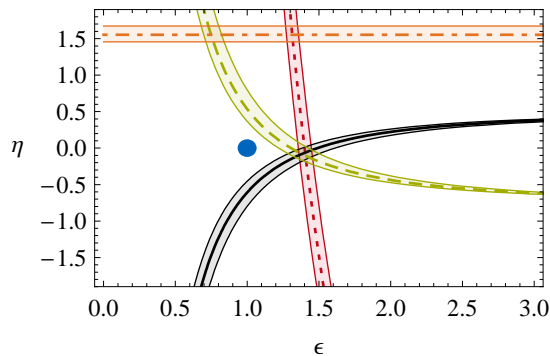


**Figure 3.9:** Constraints on the  $\epsilon$ - $\eta$ -plane obtained by applying eqs. (3.22)–(3.25) in a scenario in which SM-like  $b \rightarrow s\nu\bar{\nu}$  processes overlap with  $b \rightarrow sSS$  decays. The parameters are chosen as in fig. 3.8. The coloring and dasheding is as in fig. 3.4.

rise to shift of the Wilson coefficients similar to the analogues in eqs. (3.27)–(3.29):

$$C_L^\nu = (C_L^\nu)^{\text{SM}} - \frac{g_V^{\nu}}{2} Z'_L, \quad C_R^\nu = -\frac{g_V^{\nu}}{2} Z'_R, \quad (3.47)$$

$$C_{10} = C_{10}^{\text{SM}} + \frac{g_A^{\ell}}{2} Z'_L, \quad C'_{10} = +\frac{g_A^{\ell}}{2} Z'_R, \quad (3.48)$$

$$C_9 = C_9^{\text{SM}} - \frac{g_V^{\ell}}{2} Z'_L, \quad C'_9 = -\frac{g_V^{\ell}}{2} Z'_R, \quad (3.49)$$

where the couplings  $g_{V,A}^{\nu,\ell}$  denote the vector and axial vector couplings of the  $Z'$  to neutrinos and charged leptons, respectively. The contribution to the  $B_s$  mixing amplitude is independent of the  $g'$  couplings and is simply given by eq. (3.35) after the replacements  $Z_{L,R} \rightarrow Z'_{L,R}$ . Therefore in a general  $Z'$  model, by choosing small or zero  $U(1)'$  charges for the charged leptons it is in principle possible to completely suppress the NP contributions to  $b \rightarrow s\ell^+\ell^-$  as well as  $B_s \rightarrow \ell^+\ell^-$  decays. It is at the same time possible to obtain a strong enhancement of  $b \rightarrow s\nu\bar{\nu}$  modes and/or a sizable, potentially complex, contribution to the  $B_s$  mixing amplitude.

### 3.6.2 Littlest Higgs with T-Parity (LHT)

Right-handed currents are absent or suppressed in most NP models. One example is the Littlest Higgs model with T-parity, where  $C_R^\nu$  is negligible by construction and NP effects in  $C_L^\nu$  are rather small [69]. A scan over the parameter space shows that  $(C_L^\nu)^{\text{NP}}$  typically amounts to 10% of the SM value if experimental constraints from other flavor physics observables are imposed. Consequently, it will be difficult to distinguish this model from the SM on the basis of the decays considered here.

### 3.6.3 Randall-Sundrum model with custodial protection

Recently the decays  $B \rightarrow K^*\nu\bar{\nu}$ ,  $B \rightarrow K\nu\bar{\nu}$  and  $B \rightarrow X_{s,d}\nu\bar{\nu}$  have been analyzed in a Randall-Sundrum model with a custodial protection of the left-handed  $Z$  couplings to down-quarks [70]. In this model the NP contributions to the decays in questions are dominated then by tree level  $Z$  boson exchanges governed by right-handed couplings to down-quarks. In spite of  $C_R^\nu$  being non-vanishing in this model, the deviations from the SM for the three decays considered here are found to be even smaller than in the LHT model<sup>6</sup>. Interestingly, when the custodial protection of left-handed  $Z$  couplings is removed, NP effects in  $b \rightarrow s\nu\bar{\nu}$  transitions can be enhanced relative to the SM by as much as a factor of three which is not possible in the LHT model and in several NP scenarios considered here. However, in such a scenario a strong violation of the experimental constraint on the  $Zb_L\bar{b}_L$  coupling is also predicted and a consistent analysis should take into account also electroweak precision observables.

### 3.6.4 Minimal Supersymmetric Standard Model

In this section, we discuss the effects in the MSSM with a generic flavor violating soft sector. This model gives rise to various new contributions to the  $b \rightarrow s\nu\bar{\nu}$  transition [40, 72–75] and one might expect that large effects are possible. To be specific, effects of virtual gluinos, neutralinos, charged Higgs bosons and charginos contribute potentially to the observables as well as to other already experimentally accessible FCNCs, which we will use as additional constraints.

- As neutralino and gluino contributions are generally sensitive to the same mass insertions and gluinos are strongly interacting, neutralino contributions are always negligible relative to the gluino contributions. Gluino contributions to both  $C_L^\nu$  and  $C_R^\nu$  are in turn highly constrained by the  $b \rightarrow s\gamma$  decay and indeed have only negligible impact [75].
- The charged Higgs contributions to  $C_L^\nu$  scale as  $1/\tan^2\beta$  and even for low values of  $\tan\beta$  they play only a marginal role. The charged Higgs contributions to the right-handed coefficient  $C_R^\nu$  are proportional to  $m_s m_b \tan^2\beta$  at leading order and therefore negligible even for large values of  $\tan\beta$ .

Although non-holomorphic corrections to the Higgs couplings can potentially lead

---

<sup>6</sup>See also [71] for the discussion of the inclusive  $B \rightarrow X_s\nu\bar{\nu}$  in the context of slightly different Randall-Sundrum setup.

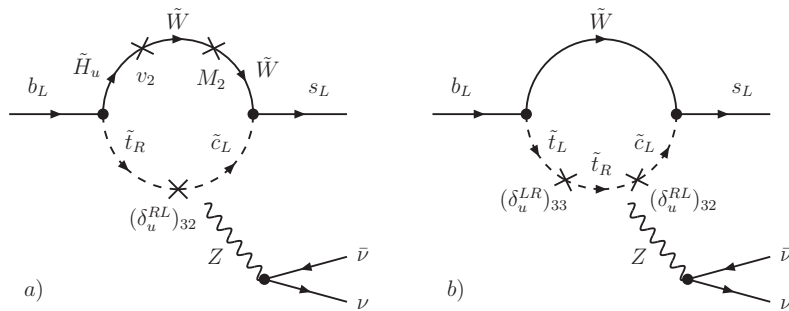


**Figure 3.10:** Dominant chargino contributions to the Wilson coefficient  $C_L^\nu$  in the mass insertion approximation. Concerning its structure, we note that among the required two  $SU(2)_L$  breaking insertions in the  $Z$  penguin, one is formally provided by the helicity and flavor changing mass insertion  $(\delta_u^{RL})_{32}$  and the other one by a Higgsino-Wino mixing (diagram *a*) or a flavor conserving helicity flip for the stop (diagram *b*), respectively.

to important effects in the large  $\tan\beta$  regime<sup>7</sup>, the size of these effects is negligible due to the experimental data on  $B_s \rightarrow \mu^+\mu^-$  [61, 75].

- The chargino contributions to the right-handed coefficient  $C_R^\nu$  have at the leading order the same suppression factor as the Higgs contributions and are therefore negligible, too. However, chargino contributions to the left-handed coefficient  $C_L^\nu$  are still possible. In fact, the largest of these can be generated by a  $Z$  penguin with a  $(\delta_u^{RL})_{32}$  mass insertion [56, 77, 78], that is not strongly constrained by existing data [77, 79–81]. The  $Z$  penguin diagrams giving that contribution are shown in fig. 3.10 in the mass insertion approximation<sup>8</sup>

In summary, all the discussed contributions to  $C_R^\nu$  in the MSSM are small or in addition very constrained by other observables. Consequently, the longitudinal polarization fraction in the  $B \rightarrow K^*\nu\bar{\nu}$  decay,  $F_L(q^2)$ , is always SM like. The chargino contributions to the left-handed coefficient  $C_L^\nu$ , however, can potentially lead to sizable effects.

After this qualitative discussion we analyze the possible impact of chargino contributions in  $C_L^\nu$  within a scan of the parameter space in a domain where such chargino effects are pronounced. Due to the fact that these chargino contributions are not sensitive to the value of  $\tan\beta$ , we choose to work in the low  $\tan\beta$  regime. In fact, this avoids possible large Higgs effects in  $B_s \rightarrow \mu^+\mu^-$  and the corresponding constraint from this decay. We

<sup>7</sup>This effect is well-known in the case of  $s \rightarrow d\nu\bar{\nu}$  transitions [76].

<sup>8</sup>In our numerical analysis, we work with mass eigenstates and include the complete set of SUSY contributions as given in [74].

### 3. $B \rightarrow K^{(*)}\nu\nu$ and $B \rightarrow X_s\nu\nu$

---

Parameter Set	$\tan\beta$	$\mu$	$M_2$	$m_{\tilde{Q}}$	$m_{\tilde{U}}$	$A_t$	$(\delta_u^{RL})_{32}$
I	5	500	800	500	400	-800	0.75
II	5	120	700	400	800	-700	-0.5

**Table 3.3:** Two example MSSM parameter sets giving large effects in  $b \rightarrow s\nu\bar{\nu}$  transitions. Dimensionful quantities are expressed in GeV.

scan the relevant MSSM parameters in the following ranges

$$\begin{aligned}
5 < \tan\beta < 10 & \quad , \quad m_{\tilde{Q}}, m_{\tilde{U}}, M_2 < 1\text{TeV} \quad , \\
-1\text{TeV} < \mu < 1\text{TeV} & \quad , \quad -3 < A_t/\sqrt{m_{\tilde{Q}}m_{\tilde{U}}} < 3 \quad , \\
0 < |(\delta_u^{RL})_{32}| < 1 & \quad , \quad 0 < \text{Arg} [(\delta_u^{RL})_{32}] < 2\pi
\end{aligned} \tag{3.50}$$

and fix the remaining mass parameters to 1 TeV.

We apply constraints imposed by:

- direct searches for SUSY particles
- the lower bound on the Higgs mass
- the absence of charge and color breaking minima in the scalar potential
- the measurements of various FCNC processes like  $B \rightarrow X_s\gamma$ ,  $B \rightarrow X_s\ell^+\ell^-$ ,  $\Delta M_s/\Delta M_d$ ,  $\epsilon_K$  and  $\Delta M_K$ .

Applying the outlined procedure, we end up with the following ranges for the branching ratios of the decays  $B \rightarrow K^*\nu\bar{\nu}$ ,  $B \rightarrow K\nu\bar{\nu}$  and  $B \rightarrow X_s\nu\bar{\nu}$

$$5.3 \times 10^{-6} \lesssim \text{BR}(B \rightarrow K^*\nu\bar{\nu}) \lesssim 8.7 \times 10^{-6} \quad , \tag{3.51}$$

$$3.5 \times 10^{-6} \lesssim \text{BR}(B \rightarrow K\nu\bar{\nu}) \lesssim 5.8 \times 10^{-6} \quad , \tag{3.52}$$

$$2.1 \times 10^{-5} \lesssim \text{BR}(B \rightarrow X_s\nu\bar{\nu}) \lesssim 3.6 \times 10^{-5} \quad . \tag{3.53}$$

We emphasize that, disregarding the negligible effects in  $C_R^\nu$ , these three branching ratios are perfectly correlated.

The effects in the corresponding differential branching ratios for these decays are shown in fig. 3.11 for the two example MSSM parameter sets found in table 3.3.

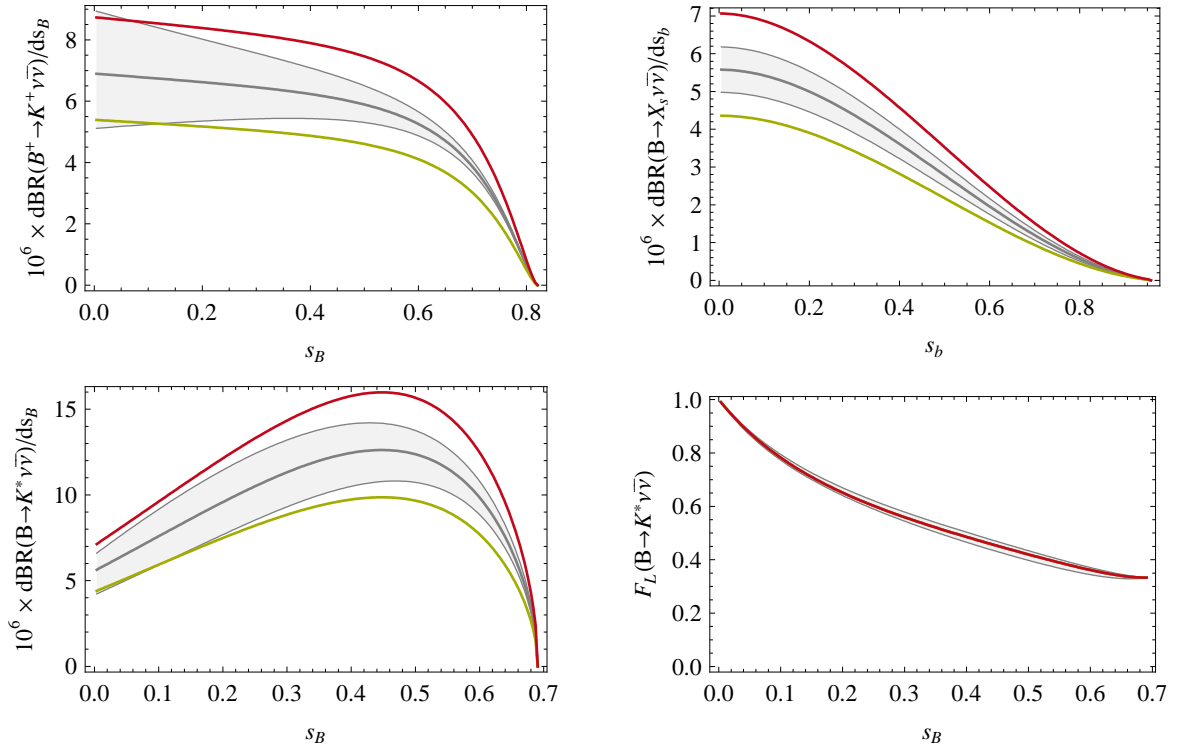


**Figure 3.11:** Dependence of the four  $b \rightarrow s \nu \bar{\nu}$  observables on the normalized neutrino invariant masses squared  $s_{b,B}$  for two MSSM parameter points that give large effects within the considered scenario. The upper red lines correspond to the MSSM parameter set I of table 3.3, while the lower green ones correspond to parameter set II. The gray bands represent the SM predictions and the corresponding theory uncertainty.

Before closing this section, we note the correlation between the branching ratios of  $B \rightarrow K^* \nu \bar{\nu}$  and  $B_s \rightarrow \mu^+ \mu^-$  shown in fig. 3.12. It illustrates explicitly the common dominant contributions of  $Z$  penguins to these two processes. Both Higgs penguin and box contributions to  $B_s \rightarrow \mu^+ \mu^-$  are negligible, since in our framework  $\tan \beta$  is small and the heavy Higgs and the slepton masses are fixed to 1 TeV. A deviation from this correlation would correspondingly signal either sizable box contributions to  $B \rightarrow K^* \nu \bar{\nu}$  or  $B_s \rightarrow \mu^+ \mu^-$ , being possible with a very light slepton spectrum, or in the presence of Higgs penguins in the  $B_s \rightarrow \mu^+ \mu^-$  decay.

### 3. $B \rightarrow K^{(*)}\nu\nu$ and $B \rightarrow X_s\nu\nu$

---

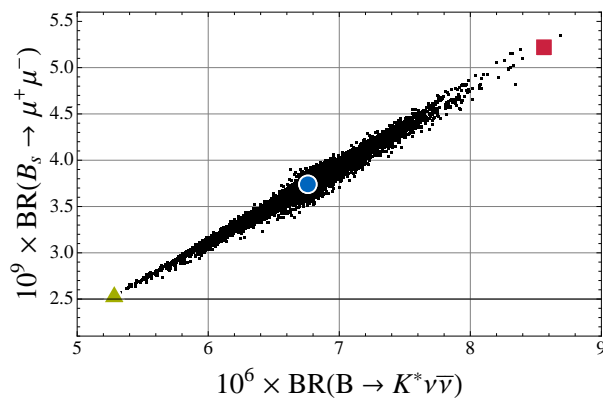


**Figure 3.12:** Correlation between  $\text{BR}(B \rightarrow K^*\nu\bar{\nu})$  and  $\text{BR}(B_s \rightarrow \mu^+\mu^-)$  in the considered MSSM scenario. The blue circle represents the SM point, while the red square (green diamond) corresponds to the MSSM parameter set I (II).



# Chapter 4

## $B \rightarrow K^* \mu^+ \mu^-$

### 4.1 Introduction

The decay  $B \rightarrow K^*(\rightarrow K\pi)\mu^+\mu^-$ , based on the quark level decay  $b \rightarrow s\mu^+\mu^-$ , is regarded as one of the crucial channels for B physics. This has mainly two reasons: First the all-charged final state of the decay gives access to a vast number of observables sensitive to NP. Second, combined with its charge conjugated counterpart, it is possible to construct observables which sensitive are sensitive to CP violation.

This chapter is is organized as follows: We review the effective Hamiltonian governing the decay  $B \rightarrow K^*(\rightarrow K\pi)\mu^+\mu^-$  and discuss the resulting differential (angular) distribution of the decay products. Furthermore we discuss non-factorizable QCD effects and define the basic set of observables which have the advantage of high theoretical cleanliness and likewise high sensitivity to NP effects. Then we perform a phenomenological analysis of those observables in the SM, in a model-independent way and in several selected NP scenarios.

### 4.2 Effective Hamiltonian

The decay  $B \rightarrow K^*\mu^+\mu^-$  is induced by the weak effective Hamiltonian given by [82, 83]

$$\mathcal{H}_{\text{eff}} = -\frac{4G_F}{\sqrt{2}} \left( \lambda_t \mathcal{H}_{\text{eff}}^{(t)} + \lambda_u \mathcal{H}_{\text{eff}}^{(u)} \right) , \quad (4.1)$$

with the CKM matrix element combinations  $\lambda_i = V_{ib}V_{is}^*$  and

$$\mathcal{H}_{\text{eff}}^{(t)} = C_1\mathcal{O}_1^c + C_2\mathcal{O}_2^c + \sum_{i=3}^6 C_i\mathcal{O}_i + \sum_{i=7,8,9,10,P,S} (C_i\mathcal{O}_i + C'_i\mathcal{O}'_i),$$

$$\mathcal{H}_{\text{eff}}^{(u)} = C_1(\mathcal{O}_1^c - \mathcal{O}_1^u) + C_2(\mathcal{O}_2^c - \mathcal{O}_2^u).$$

We keep the contribution of  $\mathcal{H}_{\text{eff}}^{(u)}$ , although it is doubly Cabibbo-suppressed with respect to that of  $\mathcal{H}_{\text{eff}}^{(t)}$ , as certain observables we consider are sensitive to the induced complex phases in the decay amplitudes. The operators  $\mathcal{O}_i$  are given by [82]

$$\mathcal{O}_1^q = 4(\bar{s}\gamma_\mu T^a P_L q)(\bar{q}\gamma^\mu T^a P_L b), \quad \mathcal{O}_2^q = 4(\bar{s}\gamma_\mu P_L q)(\bar{q}\gamma^\mu P_L b), \quad (4.2)$$

$$\mathcal{O}_3 = 4(\bar{s}\gamma_\mu P_L b)\sum_q(\bar{q}\gamma^\mu P_L q), \quad \mathcal{O}_4 = 4(\bar{s}\gamma_\mu T^a P_L b)\sum_q(\bar{q}\gamma^\mu T^a P_L q), \quad (4.3)$$

$$\mathcal{O}_5 = 4(\bar{s}\gamma_{\mu_1}\gamma_{\mu_2}\gamma_{\mu_3}P_L b)\sum_q(\bar{q}\gamma_{\mu_1}\gamma^{\mu_2}\gamma^{\mu_3}P_L q), \quad (4.4)$$

$$\mathcal{O}_6 = 4(\bar{s}\gamma_{\mu_1}\gamma_{\mu_2}\gamma_{\mu_3}T^a P_L b)\sum_q(\bar{q}\gamma^{\mu_1}\gamma^{\mu_2}\gamma^{\mu_3}T^a P_L q), \quad (4.5)$$

$$\mathcal{O}_7 = \frac{e}{g^2}m_b(\bar{s}\sigma_{\mu\nu}P_R b)F^{\mu\nu}, \quad \mathcal{O}'_7 = \frac{e}{g^2}m_b(\bar{s}\sigma_{\mu\nu}P_L b)F^{\mu\nu}, \quad (4.6)$$

$$\mathcal{O}_8 = \frac{1}{g}m_b(\bar{s}\sigma_{\mu\nu}T^a P_R b)G^{\mu\nu a}, \quad \mathcal{O}'_8 = \frac{1}{g}m_b(\bar{s}\sigma_{\mu\nu}T^a P_L b)G^{\mu\nu a}, \quad (4.7)$$

$$\mathcal{O}_9 = \frac{e^2}{g^2}(\bar{s}\gamma_\mu P_L b)(\bar{\mu}\gamma^\mu\mu), \quad \mathcal{O}'_9 = \frac{e^2}{g^2}(\bar{s}\gamma_\mu P_R b)(\bar{\mu}\gamma^\mu\mu), \quad (4.8)$$

$$\mathcal{O}_{10} = \frac{e^2}{g^2}(\bar{s}\gamma_\mu P_L b)(\bar{\mu}\gamma^\mu\gamma_5\mu), \quad \mathcal{O}'_{10} = \frac{e^2}{g^2}(\bar{s}\gamma_\mu P_R b)(\bar{\mu}\gamma^\mu\gamma_5\mu), \quad (4.9)$$

$$\mathcal{O}_S = \frac{e^2}{16\pi^2}m_b(\bar{s}P_R b)(\bar{\mu}\mu), \quad \mathcal{O}'_S = \frac{e^2}{16\pi^2}m_b(\bar{s}P_L b)(\bar{\mu}\mu), \quad (4.10)$$

$$\mathcal{O}_P = \frac{e^2}{16\pi^2}m_b(\bar{s}P_R b)(\bar{\mu}\gamma_5\mu), \quad \mathcal{O}'_P = \frac{e^2}{16\pi^2}m_b(\bar{s}P_L b)(\bar{\mu}\gamma_5\mu), \quad (4.11)$$

where  $g$  is the strong coupling constant,  $T^a$  are the generators of  $SU(3)$  and  $P_{L,R} = (1 \mp \gamma_5)/2$ .  $m_b$  denotes the running  $b$  quark mass in the  $\overline{\text{MS}}$  scheme. The primed operators with opposite chirality to the unprimed ones vanish or are highly suppressed in the SM, as are  $\mathcal{O}_{S,P}$ . We neglect the contributions of  $\mathcal{O}'_i$  for  $1 \leq i \leq 6$ .

In tab. 4.1 we give all the SM values of the Wilson coefficients to NNLL accuracy. As

#### 4. $B \rightarrow K^* \mu^+ \mu^-$

---

we shall see below, in eqs. (4.50-4.54),  $C_{7,9}$  always appear in a particular combination with other  $C_i$  in matrix elements. It hence proves convenient to define effective coefficients  $C_{7,9}^{(\prime)\text{eff}}$ , and also  $C_{8,10}^{(\prime)\text{eff}}$ , which are given by [84]

$$\begin{aligned} C_7^{\text{eff}} &= \frac{4\pi}{\alpha_s} C_7 - \frac{1}{3} C_3 - \frac{4}{9} C_4 - \frac{20}{3} C_5 - \frac{80}{9} C_6, \\ C_8^{\text{eff}} &= \frac{4\pi}{\alpha_s} C_8 + C_3 - \frac{1}{6} C_4 + 20C_5 - \frac{10}{3} C_6, \\ C_9^{\text{eff}} &= \frac{4\pi}{\alpha_s} C_9 + Y(q^2), \\ C_{10}^{\text{eff}} &= \frac{4\pi}{\alpha_s} C_{10}, \quad C_{7,8,9,10}^{\prime,\text{eff}} = \frac{4\pi}{\alpha_s} C_{7,8,9,10}^{\prime}, \end{aligned} \quad (4.12)$$

$$\begin{aligned} \text{with } Y(q^2) &= h(q^2, m_c) \left( \frac{4}{3} C_1 + C_2 + 6C_3 + 60C_5 \right) \\ &\quad - \frac{1}{2} h(q^2, m_b) \left( 7C_3 + \frac{4}{3} C_4 + 76C_5 + \frac{64}{3} C_6 \right) \\ &\quad - \frac{1}{2} h(q^2, 0) \left( C_3 + \frac{4}{3} C_4 + 16C_5 + \frac{64}{3} C_6 \right) \\ &\quad + \frac{4}{3} C_3 + \frac{64}{9} C_5 + \frac{64}{27} C_5. \end{aligned} \quad (4.13)$$

The function

$$h(q^2, m_q) = -\frac{4}{9} \left( \ln \frac{m_q^2}{\mu^2} - \frac{2}{3} - z \right) - \frac{4}{9} (2+z) \sqrt{|z-1|} \times \begin{cases} \arctan \frac{1}{\sqrt{z-1}} & z > 1 \\ \ln \frac{1 + \sqrt{1-z}}{\sqrt{z}} - \frac{i\pi}{2} & z \leq 1 \end{cases} \quad (4.14)$$

with  $z = 4m_q^2/q^2$ , is related to the basic fermion loop.

We shall see below that  $B \rightarrow K^*(\rightarrow K\pi)\mu^+\mu^-$  does not allow to access all the above coefficients separately: for instance, only the combinations  $C_S - C'_S$  and  $C_P - C'_P$  enter the decay amplitude.

### 4.3 Differential Decay Distribution

In this section we discuss the angular distribution of the decay products of the decay  $B \rightarrow K^*(\rightarrow K\pi)(\ell^+\ell^-)$ . We begin our discussion with the case of massless final state

$C_1(\mu)$	$C_2(\mu)$	$C_3(\mu)$	$C_4(\mu)$	$C_5(\mu)$	$C_6(\mu)$	$C_7^{\text{eff}}(\mu)$	$C_8^{\text{eff}}(\mu)$	$C_9^{\text{eff}}(\mu) - Y(q^2)$	$C_{10}^{\text{eff}}(\mu)$
-0.257	1.009	-0.005	-0.078	0.000	0.001	-0.304	-0.167	4.211	-4.103
$\bar{C}_1(\mu)$	$\bar{C}_2(\mu)$	$\bar{C}_3(\mu)$	$\bar{C}_4(\mu)$	$\bar{C}_5(\mu)$	$\bar{C}_6(\mu)$	$C_7^{\prime\text{eff}}(\mu)$	$C_8^{\prime\text{eff}}(\mu)$		
-0.128	1.052	0.011	-0.032	0.009	-0.037	-0.006	-0.003		

**Table 4.1:** SM Wilson coefficients at the scale  $\mu = m_b = 4.8$  GeV, to NNLL accuracy. All other Wilson coefficients are heavily suppressed in the SM. The “barred”  $\bar{C}_i$  are related to  $C_i$  as defined in ref. [85]. Input:  $\alpha_s(m_W) = 0.120$ ,  $\alpha_s(m_b) = 0.214$ , obtained from  $\alpha_s(m_Z) = 0.1176$  [19], using three-loop evolution. We also use  $m_t(m_t) = 162.3$  GeV [31],  $m_W = 80.4$  GeV and  $\sin^2 \theta_W = 0.23$ .

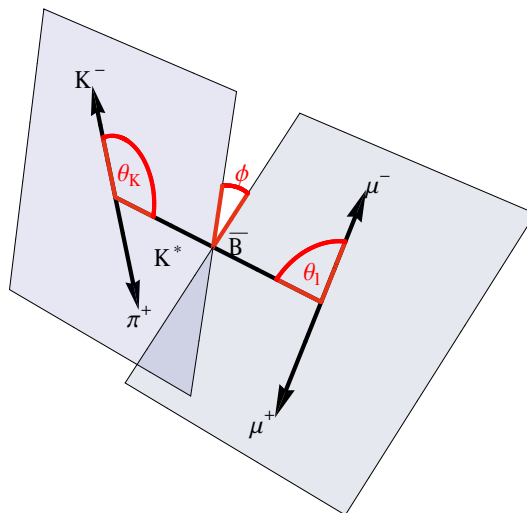


**Figure 4.1:** The kinematics of  $B \rightarrow K^*(\rightarrow K\pi)(\ell^+\ell^-)$ .

leptons, where we use and extend the formalism of helicity amplitudes, introduced in last chapter. In a second step we keep the lepton mass finite and give a summary of the associated new features relative to the case of massless leptons.

### 4.3.1 Massless leptons

In the limit of vanishing lepton mass, helicity and chirality of the final state leptons coincide and operators (containing chiral projectors) relate leptons with definite helicity. In this case, it is possible to factorize the matrix element  $B \rightarrow K^*(\rightarrow K\pi)(\ell^+\ell^-)_L$  into three matrix elements of the subprocesses, the so-called helicity amplitudes. This fact considerably facilitates the discussion of the kinematics [86] because the helicity amplitudes can be evaluated separately in the relevant rest frames<sup>1</sup>.

The factorization for the process  $B \rightarrow K^*(\rightarrow K\pi)(\ell^+\ell^-)_L$ , again in the narrow-width approximation (see section 3.3.1), reads:

$$\mathcal{M}_L \propto \sum_{\lambda=0,\pm 1} L_\lambda^L H_\lambda^L Y_\lambda^1 \quad (4.15)$$

and analogously for  $\mathcal{M}_R$ , where the index  $L(R)$  indicates the decay in a left-handed (right-handed) lepton and right-handed (left-handed) anti-lepton. The individual factors have the following meaning:

- $H_\lambda^{L,R}$  describes the decay  $B \rightarrow K_\lambda^* V_\lambda^*$ . The helicities of the bosonic vector state are denoted by the same symbol  $\lambda$  because they coincide due to angular momentum conservation. In principle, four helicities are possible:  $+, -, 0$  and  $s$  for scalar. However, the matrix element for the decay  $V_s^* \rightarrow (\ell^+\ell^-)_{L,R}$  vanishes in the limit of zero lepton masses.
- $L_\lambda^{L,R}$  describes the decay  $V_\lambda^* \rightarrow (\ell^+\ell^-)_{L,R}$ . In the massless case, the lepton and the anti-lepton share the helicity, again due to angular momentum conservation. The leptonic amplitudes are evaluated in the  $V^*$  rest frame, and  $\theta_l$  is the angle between  $\vec{p}_B$  and  $\vec{p}_{\ell^-}$ . For example,  $L_\lambda^L$  corresponds to the Lorentz product of the left handed lepton current and the polarization vector,  $\varepsilon_\lambda^\mu \bar{u} \gamma_\mu P_L v$ . In the massless case, it is possible to square the expression (using the completeness relation) and to take the square root afterwards. Using this technique, the explicit result for

---

<sup>1</sup>See [87] for an alternative discussion of the kinematics of four-body decays.

leptonic amplitudes in the  $V^*$  rest frame can be written as:

$$\begin{aligned} L_1^L &= -\cos^2(\theta_l/2), & L_1^R &= \sin^2(\theta_l/2), \\ L_0^L &= \sin(\theta_l), & L_0^R &= \sin(\theta_l), \\ L_{-1}^L &= -\sin^2(\theta_l/2), & L_{-1}^R &= \cos^2(\theta_l/2). \end{aligned} \quad (4.16)$$

The techniques for the case of non-vanishing lepton mass are given in [32, 86].

- The amplitudes  $Y_\lambda^1$  describe the decay  $K_\lambda^* \rightarrow K\pi$  (c.f. section 3.3.1) and have the explicit form:

$$\begin{aligned} Y_\pm^1(\phi, \theta_{K^*}) &= \mp \sqrt{\frac{3}{8\pi}} e^{\pm i\phi} \sin \theta_{K^*}, \\ Y_0^1(\phi, \theta_{K^*}) &= \sqrt{\frac{3}{4\pi}} \cos \theta_{K^*}. \end{aligned}$$

The angles  $\phi$  and  $\theta_{K^*}$  are specified in the  $K^*$  rest frame.  $\theta_{K^*}$  is the angle between  $-\vec{p}_B$  and  $\vec{p}_\pi$  and  $\phi$  is given by the angle of the two planes  $(\vec{p}_B, \vec{p}_K)$  and  $(\vec{p}_B, \vec{p}_\pi)$ .

The angular distribution follows immediately from the above amplitudes by taking the square of the left- and right-handed amplitudes separately:

$$\frac{d^4\Gamma}{dq^2 d\cos\theta_l d\cos\theta_{K^*} d\phi} = \frac{9}{32\pi} I(q^2, \theta_l, \theta_{K^*}, \phi), \quad (4.17)$$

where

$$I(q^2, \theta_l, \theta_{K^*}, \phi) = \frac{8\pi}{3} \left( \left| \sum_{\lambda=0, \pm 1} L_\lambda^L H_\lambda^L Y_\lambda^1 \right|^2 + \left| \sum_{\lambda=0, \pm 1} L_\lambda^R H_\lambda^R Y_\lambda^1 \right|^2 \right). \quad (4.18)$$

Before we proceed, we note that it is instructive to reexpress the last equation in terms of a so-called spin density matrix,

$$\rho_{\lambda\lambda'}^L = L_\lambda^L H_\lambda^L Y_\lambda^1 (L_{\lambda'}^L H_{\lambda'}^L Y_{\lambda'}^1)^*, \quad (4.19)$$

which is obviously Hermitian,  $\rho_{\lambda\lambda'} = \rho_{\lambda'\lambda}^*$ , and has 9 independent components, 3 being absolute values, 3 real parts and 3 being imaginary parts<sup>2</sup>. The differential decay

<sup>2</sup>For an interesting, alternative explanation of the number of observables see [88].

#### 4. $B \rightarrow K^* \mu^+ \mu^-$

---

amplitude takes the form

$$I(q^2, \theta_l, \theta_{K^*}, \phi) = \frac{8\pi}{3} \sum_{\lambda, \lambda'=0, \pm 1} (\rho_{\lambda\lambda'}^L + \rho_{\lambda\lambda'}^R). \quad (4.20)$$

The number of 9 independent observables is reflected by the 9 coefficients  $I_i$  in the differential decay amplitude

$$\begin{aligned} I(q^2, \theta_l, \theta_{K^*}, \phi) &= I_1 \sin^2 \theta_{K^*} - I_2 \cos^2 \theta_{K^*} + (I_1/3 \sin^2 \theta_{K^*} + I_2 \cos^2 \theta_{K^*}) \cos 2\theta_l \\ &+ I_3 \sin^2 \theta_{K^*} \sin^2 \theta_l \cos 2\phi + I_4 \sin 2\theta_{K^*} \sin 2\theta_l \cos \phi \\ &+ I_5 \sin 2\theta_{K^*} \sin \theta_l \cos \phi \\ &+ I_6^s \sin^2 \theta_{K^*} \cos \theta_l + I_7 \sin 2\theta_{K^*} \sin \theta_l \sin \phi \\ &+ I_8 \sin 2\theta_{K^*} \sin 2\theta_l \sin \phi + I_9 \sin^2 \theta_{K^*} \sin^2 \theta_l \sin 2\phi. \end{aligned} \quad (4.21)$$

Expressed in terms of the transversity amplitudes,

$$A_{\perp, \parallel}^{L,R} = (H_{+1}^{L,R} \mp H_{-1}^{L,R})/\sqrt{2}, \quad A_0^{L,R} = H_0^{L,R}, \quad (4.22)$$

the coefficients read

$$I_1 = \frac{3}{4} [ |A_{\perp}^L|^2 + |A_{\parallel}^L|^2 + (L \rightarrow R) ] \quad (4.23)$$

$$I_2 = |A_0^L|^2 + (L \rightarrow R), \quad (4.24)$$

$$I_3 = \frac{1}{2} [ |A_{\perp}^L|^2 - |A_{\parallel}^L|^2 + (L \rightarrow R) ], \quad (4.25)$$

$$I_4 = \frac{1}{\sqrt{2}} [ \text{Re}(A_0^L A_{\parallel}^{L*}) + (L \rightarrow R) ], \quad (4.26)$$

$$I_5 = \sqrt{2} [ \text{Re}(A_0^L A_{\perp}^{L*}) - (L \rightarrow R) ] \quad (4.27)$$

$$I_6^s = 2 [ \text{Re}(A_{\parallel}^L A_{\perp}^{L*}) - (L \rightarrow R) ], \quad (4.28)$$

$$I_7 = \sqrt{2} [ \text{Im}(A_0^L A_{\parallel}^{L*}) - (L \rightarrow R) ], \quad (4.29)$$

$$I_8 = \frac{1}{\sqrt{2}} [ \text{Im}(A_0^L A_{\perp}^{L*}) + (L \rightarrow R) ], \quad (4.30)$$

$$I_9 = \text{Im}(A_{\parallel}^{L*} A_{\perp}^L) + (L \rightarrow R). \quad (4.31)$$

### 4.3.2 Massive leptons

In comparison to the massless case, the matrix element for non-vanishing lepton mass has three main new features: occurrence of a timelike mode  $A_t$ , mixing terms of  $A_L$  and  $A_R$  and non-factorization of the leptonic matrix elements in the (schematic) form  $L^*L$ . This means that the factorization can still be done at the level of the amplitude, i.e. the squared matrix element:

$$|\mathcal{M}|^2 = |Y_0^1 H_t|^2 + \sum_{\substack{\lambda=0,\pm 1 \\ X=L,R \\ Y=L,R}} H_{\lambda'}^X (H_{\lambda}^Y)^* Y_{\lambda}^1 (Y_{\lambda'}^1)^* L_{\lambda\lambda'}^{YX} \quad (4.32)$$

where

$$L^{LL,RR} = \frac{1}{4} \begin{pmatrix} (\beta_l \cos \theta_l \pm 1)^2 & 2\beta_l(\beta_l \cos \theta_l \mp 1) \sin \theta_l & \beta_l^2 \sin^2 \theta_l \\ 2\beta_l(\beta_l \cos \theta_l \mp 1) \sin \theta_l & 2(1 - \beta_l^2 \cos 2\theta_l) & 2\beta_l(\beta_l \cos \theta_l \mp 1) \sin \theta_l \\ \beta_l^2 \sin^2 \theta_l & 2\beta_l(\beta_l \cos \theta_l \mp 1) \sin \theta_l & (\beta_l \cos \theta_l \mp 1)^2 \end{pmatrix}, \quad (4.33)$$

and

$$L^{RL} = L^{LR} = \frac{m_\ell^2}{q^2} \times \text{diag}(1, 2, 1). \quad (4.34)$$

For example,  $L_{\lambda,\lambda'}^{LR}$  corresponds to the expression  $(\varepsilon_{\lambda}^{\mu} \bar{u} \gamma_{\mu} P_L v)(\varepsilon_{\lambda'}^{\nu} \bar{u} \gamma_{\nu} P_R v)^*$ . These expressions are no helicity amplitudes, since the projectors  $P_R$  and  $P_L$  are chirality projectors and the produced leptons are no helicity eigenstates. While this fact is not of importance for the final result, since the sum goes over the final state spins, it prevents factorization of the leptonic part of the squared amplitude.

The resulting coefficient functions for  $\bar{B}^0 \rightarrow \bar{K}^{*0} (\rightarrow K^- \pi^+) \mu^+ \mu^-$  read:

$$I_1^s = \frac{(2 + \beta_{\mu}^2)}{4} [ |A_{\perp}^L|^2 + |A_{\parallel}^L|^2 + (L \rightarrow R) ] + \frac{4m_{\mu}^2}{q^2} \text{Re} (A_{\perp}^L A_{\perp}^{R*} + A_{\parallel}^L A_{\parallel}^{R*}), \quad (4.35)$$

$$I_1^c = |A_0^L|^2 + |A_0^R|^2 + \frac{4m_{\mu}^2}{q^2} [ |A_t|^2 + 2\text{Re}(A_0^L A_0^{R*}) ] + \beta_{\mu}^2 |A_S|^2, \quad (4.36)$$

$$I_2^s = \frac{\beta_{\mu}^2}{4} [ |A_{\perp}^L|^2 + |A_{\parallel}^L|^2 + (L \rightarrow R) ], \quad (4.37)$$

$$I_2^c = -\beta_{\mu}^2 [ |A_0^L|^2 + (L \rightarrow R) ], \quad (4.38)$$

$$I_3 = \frac{1}{2} \beta_{\mu}^2 [ |A_{\perp}^L|^2 - |A_{\parallel}^L|^2 + (L \rightarrow R) ], \quad (4.39)$$

#### 4. $B \rightarrow K^* \mu^+ \mu^-$

---

$$I_4 = \frac{1}{\sqrt{2}} \beta_\mu^2 [\text{Re}(A_0^L A_{\parallel}^{L*}) + (L \rightarrow R)], \quad (4.40)$$

$$I_5 = \sqrt{2} \beta_\mu \left[ \text{Re}(A_0^L A_{\perp}^{L*}) - (L \rightarrow R) - \frac{m_\mu}{\sqrt{q^2}} \text{Re}(A_{\parallel}^L A_S^* + A_{\parallel}^R A_S^*) \right], \quad (4.41)$$

$$I_6^s = 2\beta_\mu [\text{Re}(A_{\parallel}^L A_{\perp}^{L*}) - (L \rightarrow R)], \quad (4.42)$$

$$I_6^c = 4\beta_\mu \frac{m_\mu}{\sqrt{q^2}} \text{Re} [A_0^L A_S^* + (L \rightarrow R)], \quad (4.43)$$

$$I_7 = \sqrt{2} \beta_\mu \left[ \text{Im}(A_0^L A_{\parallel}^{L*}) - (L \rightarrow R) + \frac{m_\mu}{\sqrt{q^2}} \text{Im}(A_{\perp}^L A_S^* + A_{\perp}^R A_S^*) \right], \quad (4.44)$$

$$I_8 = \frac{1}{\sqrt{2}} \beta_\mu^2 [\text{Im}(A_0^L A_{\perp}^{L*}) + (L \rightarrow R)], \quad (4.45)$$

$$I_9 = \beta_\mu^2 [\text{Im}(A_{\parallel}^{L*} A_{\perp}^L) + (L \rightarrow R)]. \quad (4.46)$$

#### 4.3.3 The CP-conjugated mode

The differential decay distribution for the CP-conjugated mode  $B^0 \rightarrow K^{*0} (\rightarrow K^+ \pi^-) \mu^+ \mu^-$  is

$$\frac{d^4 \bar{\Gamma}}{dq^2 d \cos \theta_l d \cos \theta_{K^*} d \phi} = \frac{9}{32\pi} \bar{I}(q^2, \theta_l, \theta_{K^*}, \phi). \quad (4.47)$$

The function  $\bar{I}(q^2, \theta_l, \theta_{K^*}, \phi)$  is obtained from (4.21) by the replacements [33]

$$I_{1,2,3,4,7}^{(a)} \longrightarrow \bar{I}_{1,2,3,4,7}^{(a)}, \quad I_{5,6,8,9}^{(a)} \longrightarrow -\bar{I}_{5,6,8,9}^{(a)}, \quad (4.48)$$

where  $\bar{I}_i^{(a)}$  equals  $I_i^{(a)}$  with all weak phases conjugated. The minus sign in (4.48) is a result of our convention that, while  $\theta_{K^*}$  is the angle between the  $\bar{K}^{*0}$  and the  $K^-$  flight direction or between the  $K^{*0}$  and the  $K^+$ , respectively, the angle  $\theta_l$  is measured between the  $\bar{K}^{*0}$  ( $K^{*0}$ ) and the lepton  $\mu^-$  in *both* modes. Thus, a CP transformation interchanging lepton and antilepton leads to the transformations  $\theta_l \rightarrow \theta_l - \pi$  and  $\phi \rightarrow -\phi$ , as can be seen from eqs. (4.16) and (4.17). This convention agrees with refs. [33, 89, 90], but differs from the convention used in some experimental publications [91], where  $\theta_l$  is defined as the angle between  $K^{*0}$  and  $\mu^+$  in the  $B^0$  decay, but between  $\bar{K}^{*0}$  and  $\mu^-$  in the  $\bar{B}^0$  decay.

Finally we remark that the differential decay distribution in  $q^2$  is given by the quadratic sum of the transversity amplitudes:

$$\frac{d\Gamma(B \rightarrow K^* \mu^+ \mu^-)}{dq^2} = |A_{0L}|^2 + |A_{0R}|^2 + |A_{\perp L}|^2 + |A_{\perp R}|^2 + |A_{\parallel L}|^2 + |A_{\parallel R}|^2. \quad (4.49)$$

## 4.4 Transversity amplitudes

Here we give the explicit form of the eight transversity amplitudes up to corrections of  $O(\alpha_s)$ , whose discussion we postpone until the section 5:

$$A_{0L/R} = N \left( \frac{1}{2} \mathcal{B}_{V,0} ((C_9^{\text{eff}'} - C_9^{\text{eff}}) \mp (C_{10}^{\text{eff}'} - C_{10}^{\text{eff}})) + \mathcal{B}_{T,0} (C_7^{\text{eff}'} - C_7^{\text{eff}}) \frac{m_b}{\sqrt{q^2}} \right), \quad (4.50)$$

$$A_{\perp L/R} = N \left( \frac{1}{2} \mathcal{B}_{V,1} ((C_9^{\text{eff}'} + C_9^{\text{eff}}) \mp (C_{10}^{\text{eff}'} + C_{10}^{\text{eff}})) + \mathcal{B}_{T,1} (C_7^{\text{eff}'} + C_7^{\text{eff}}) \frac{m_b}{\sqrt{q^2}} \right), \quad (4.51)$$

$$A_{\parallel L/R} = N \left( \frac{1}{2} \mathcal{B}_{V,2} ((C_9^{\text{eff}'} - C_9^{\text{eff}}) \mp (C_{10}^{\text{eff}'} - C_{10}^{\text{eff}})) + \mathcal{B}_{T,2} (C_7^{\text{eff}'} - C_7^{\text{eff}}) \frac{m_b}{\sqrt{q^2}} \right), \quad (4.52)$$

$$A_t = N \mathcal{B}_{V,t} \left( (C_{10}^{\text{eff}} - C_{10}^{\text{eff}'}) + (C_P - C'_P) \frac{q^2}{4m_\mu} \right), \quad (4.53)$$

$$A_S = \frac{N}{2} \mathcal{B}_{V,t} (C'_S - C_S) \sqrt{q^2} \quad (4.54)$$

where

$$N = \frac{G_F V_{tb} V_{ts}^* \alpha \sqrt{\beta_\mu} \lambda^{3/4}}{16\sqrt{3}\pi^{5/2} m_B^{3/2}}, \quad (4.55)$$

with  $\lambda = m_B^4 + m_{K^*}^4 + q^4 - 2(m_B^2 m_{K^*}^2 + m_{K^*}^2 q^2 + m_B^2 q^2)$  and  $\beta_\mu = \sqrt{1 - 4m_\mu^2/q^2}$ .

With the explicit form of the transversity amplitudes and under the assumption of the SM (i.e. vanishing primed Wilson coefficients), the differential decay distribution in  $q^2$  is given by:

$$\begin{aligned} \frac{d\Gamma(B \rightarrow K^* \mu^+ \mu^-)}{dq^2} = N^2 & \left[ \frac{1}{2} (\mathcal{B}_{V,0}^2 + \mathcal{B}_{V,1}^2 + \mathcal{B}_{V,2}^2) (|C_{10}^{\text{eff}}|^2 + |C_9^{\text{eff}}|^2) \right. \\ & + 2 (\mathcal{B}_{V,0} \mathcal{B}_{T,0} + \mathcal{B}_{V,1} \mathcal{B}_{T,1} + \mathcal{B}_{V,2} \mathcal{B}_{T,2}) \frac{m_b}{\sqrt{q^2}} \text{Re}(C_7^{\text{eff}} C_9^{\text{eff}}) \\ & \left. + 2 (\mathcal{B}_{T,0}^2 + \mathcal{B}_{T,1}^2 + \mathcal{B}_{T,2}^2) \frac{m_b^2}{q^2} |C_7^{\text{eff}}|^2 \right]. \quad (4.56) \end{aligned}$$

The distribution has, as in the case of  $B \rightarrow K^* \nu \bar{\nu}$ , a very symmetric dependence on the helicity form factors, although it is more complicated due to the dependence on the

tensor form factors<sup>3</sup>.

## 4.5 Additional Corrections to Transversity Amplitudes

In addition to terms proportional to the form factors, the  $B \rightarrow K^* \mu^+ \mu^-$  amplitude contains also certain “non-factorizable” effects that do not correspond to form factors. Effects from spectator interactions induce two classes of corrections,  $O(\alpha_s)$  corrections and corrections from weak annihilation (WA). These effects have been calculated within the QCD factorization (QCDF) framework in refs. [85] and [92] in terms of the soft form factors  $\xi_\perp$  and  $\xi_\parallel$  discussed in sec. 2.2.3.

Before discussing the “non-factorizable” QCDF it is instructive to discuss the (schematic) factorization formula for the  $B \rightarrow K^*$  decay form factors:

$$F(q^2) = D\xi(E) + \phi_B \otimes T_H \otimes \phi_{K^*} + O(1/m_b), \quad (4.58)$$

where  $D = 1 + O(\alpha_s)$  includes hard corrections to the weak vertex and  $E$  is the energy of the  $K^*$  meson. However, the above formula is not exact, but will receive corrections (both soft and hard) which are suppressed by powers of  $m_b$ . These corrections are unknown to date.

The non-factorizable corrections to  $B \rightarrow K^* \mu^+ \mu^-$  can be included in a factorization formula very similar to that for form factors: apart from overall factors and the Lorentz structure, the relevant terms in the decay amplitude can be written as [92]

$$\mathcal{T}_a^{(i)} = \xi_a C_a^{(i)} + \phi_B \otimes T_a^{(i)} \otimes \phi_{a,K^*} + O(1/m_b), \quad (4.59)$$

with  $a = \perp, \parallel$  and  $i = u, t$ . Note that the  $C_a^{(i)}$  in the above formula are *not* Wilson coefficients.

According to ref. [85] there are two types of  $O(\alpha_s)$  corrections, factorizable and non-factorizable. A part of the factorizable  $O(\alpha_s)$  has to be disregarded in our approach, since they amount to the difference between the soft form factors  $\xi_\parallel$  and  $\xi_\perp$  and the full

---

<sup>3</sup> We mention for completeness that in our notation the decay width of  $B \rightarrow K^* \gamma$  is given by

$$\Gamma(B \rightarrow K^* \gamma) = 3 \left( \frac{4\pi}{\alpha} \right) \left( \frac{4\pi}{\alpha_s} \right)^2 N^2 |C_7|^2 m_b^2 \mathcal{B}_{T,1}^2(0), \quad (4.57)$$

where  $N$  and  $\mathcal{B}_{T,1}$  should be evaluated at  $q^2 = 0$ .

set of form factors and are thus already included in our approach. Furthermore, the other part vanishes using the  $b$  quark mass in the  $\overline{\text{MS}}$  scheme. For the non-factorizable  $O(\alpha_s)$  corrections non of these arguments applies and they have to be fully considered.

The second class of corrections, the weak annihilation induced corrections, is given by  $T_{\parallel,-}^{(0)}(u, \omega)$  in the notation of ref. [85]. We include these corrections that are induced by the penguin operators  $\mathcal{O}_3$  and  $\mathcal{O}_4$  although they are numerically small due to the smallness of the corresponding Wilson coefficients (see tab. 4.1). Further WA corrections discussed in ref. [92] are even smaller and can be neglected or do not arise in the case of the decay of a neutral  $B$  meson, which is considered in the following.

On introducing the chirality-flipped operators, the  $\mathcal{T}_{\perp,\parallel}^{(t,u)}$  introduced above are promoted to  $\mathcal{T}_{\perp,\parallel}^{\pm(t,u)}$  corresponding to the notations of ref. [93]. In terms of these quantities, we can define the additional corrections to the transversity amplitudes<sup>4</sup>:

$$\begin{aligned}\Delta A_{\perp L,R}^{\text{QCDF}} &= \sqrt{2}N \frac{m_b}{\sqrt{q^2}} (\mathcal{T}_{\perp}^{+(t),\text{WA+nf}} + \hat{\lambda}_u \mathcal{T}_{\perp}^{+(u)}), \\ \Delta A_{\parallel L,R}^{\text{QCDF}} &= -\sqrt{2}N \frac{m_b}{\sqrt{q^2}} (\mathcal{T}_{\perp}^{-(t),\text{WA+nf}} + \hat{\lambda}_u \mathcal{T}_{\perp}^{-(u)}), \\ \Delta A_{0L,R}^{\text{QCDF}} &= \frac{N(m_B^2 - q^2)}{2m_{K^*}m_B^2} m_b (\mathcal{T}_{\parallel}^{-(t),\text{WA+nf}} + \hat{\lambda}_u \mathcal{T}_{\parallel}^{-(u)}).\end{aligned}\tag{4.60}$$

The superscript, WA+nf, on  $\mathcal{T}_{\perp}^{\pm(t)}$  indicates that only contributions from WA and non-factorizable  $O(\alpha_s)$  corrections are to be included. In accordance with ref. [89], we define  $\hat{\lambda}_u = \lambda_u/\lambda_t$ . The total transversity amplitudes are given by the expressions in eqs. (4.50–4.53) plus the above terms  $\Delta A^{\text{QCDF}}$ . Note, that there are no corrections to  $A_t$  or  $A_S$ .

## 4.6 Observables

As discussed in the previous section, the decay distribution is fully described by the coefficients  $I_i$ . As these coefficients suffer large hadronic uncertainties they are not suited directly as observables. The observables defined in this section do not show this disadvantage and allow furthermore to separate CP conserving and CP violating effects. Independently of the final choice of observables, all observables are functions of  $q^2$ . A useful and important way to quantify statements about their behavior in a single number

---

<sup>4</sup>It should be noted that the functions  $F_{1,2,u}^{(7,9)}$  entering the non-factorizable corrections are defined with a different overall sign in refs. [92] and [94].

#### 4. $B \rightarrow K^* \mu^+ \mu^-$

---

	$m_\mu = 0$	$m_\mu \neq 0$
SM	18	22
SM + $\mathcal{O}_S^{(l)}$	20	24

**Table 4.2:** Number of independent observables in  $B \rightarrow K^*(\rightarrow K\pi)\mu^+\mu^-$ , depending on whether lepton mass effects and/or scalar operators are taken into account.

is to give the position of the zero crossings in  $q^2$  of certain observables or to consider the integrated observable over the kinematically allowed  $q^2$  range.

##### 4.6.1 Differential Observables

The 12 angular coefficient functions  $I_i^{(a)}$  of the angular distribution of  $\bar{B}^0 \rightarrow \bar{K}^{*0}(\rightarrow K^-\pi^+)\mu^+\mu^-$  constitute, together with the corresponding coefficients  $\bar{I}_i^{(a)}$  of the CP conjugate mode, a complete set of accessible observables. The obvious advantage of these coefficients – their simple connection to the angular distribution – is unfortunately compensated by the inability to separate CP-conserving and CP-violating NP effects and their large theoretical errors. To cure these shortcomings, we find it more convenient to consider the twelve CP averaged angular coefficients,

$$S_i^{(a)} = \left( I_i^{(a)} + \bar{I}_i^{(a)} \right) \Big/ \frac{d(\Gamma + \bar{\Gamma})}{dq^2}, \quad (4.61)$$

as well as the twelve CP asymmetries<sup>5</sup>

$$A_i^{(a)} = \left( I_i^{(a)} - \bar{I}_i^{(a)} \right) \Big/ \frac{d(\Gamma + \bar{\Gamma})}{dq^2}. \quad (4.62)$$

The normalization to the CP-averaged dilepton mass distribution reduces or even cancels both experimental and theoretical uncertainties. The CP asymmetries are particularly relevant in the context of CP-violating phases in NP models. This is a consequence of their smallness in the SM [89], which is in turn due to the fact that the only CP-violating phase affecting the decay enters via  $\lambda_u$  in eq. (4.1) and is doubly Cabibbo-suppressed.

It should be stressed that out of these 24 observables, two vanish in the SM, namely  $S_6^c$  and  $A_6^c$ , which are generated only by scalar operators, and four are related to others in the limit of massless leptons through  $S_1^s = 3S_2^s$ ,  $S_1^c = -S_2^c$  and  $A_1^s = 3A_2^s$ ,  $A_1^c = -A_2^c$ . Table 4.2 summarizes the number of independent observables in these limits.

In addition, even for non-zero lepton mass, only three of the four  $S_{1,2}^{s,c}$  are independent,

---

<sup>5</sup> Note that our definition of the CP asymmetries differs from ref. [89] by a factor of  $\frac{3}{2}$ .

which is due to the normalization (4.61), leading to the relation

$$\frac{3}{4}(2S_1^s + S_1^c) - \frac{1}{4}(2S_2^s + S_2^c) = 1. \quad (4.63)$$

Consequently, the complete set of 24 independent observables would be given by the twelve  $A_i^{(a)}$ , eleven  $S_i^{(a)}$  and the CP-averaged dilepton mass distribution  $d(\Gamma + \bar{\Gamma})/dq^2$ . However, in contrast to the other observables, the latter is not normalized to a quantity containing the form factors and thus it is not as clean.

In principle there are two ways to extract the observables  $S_i^{(a)}$  and  $A_i^{(a)}$  from experimental data. First, a fit of the angular distributions eqs. (4.17) and (4.47) to data, and the subsequent combination of the found  $I_i^{(a)}$  and  $\bar{I}_i^{(a)}$  in the observables. Second, a integration of the  $d^4(\Gamma \pm \bar{\Gamma})$  over certain parts of the angles  $\theta_l$ ,  $\theta_{K^*}$  and  $\phi$ , as for example:

$$S_5 = -\frac{4}{3} \left[ \int_{\pi/2}^{3\pi/2} - \int_0^{\pi/2} - \int_{3\pi/2}^{2\pi} \right] d\phi \left[ \int_0^1 - \int_{-1}^0 \right] d \cos \theta_K \frac{d^3(\Gamma - \bar{\Gamma})}{dq^2 d \cos \theta_K d\phi} \bigg/ \frac{d(\Gamma + \bar{\Gamma})}{dq^2}. \quad (4.64)$$

Both ways were shown to be viable for several similar observables in ref. [88, 89].

Since  $S_i^{(a)}$  and  $A_i^{(a)}$  constitute a complete set of possible observables for the decay  $B \rightarrow K^*(\rightarrow K\pi)\mu^+\mu^-$ , all established observables can be expressed in terms of these quantities. For example, the CP asymmetry in the dilepton mass distribution is given by (see eq. (4.63))

$$A_{\text{CP}} = \frac{d(\Gamma - \bar{\Gamma})}{dq^2} \bigg/ \frac{d(\Gamma + \bar{\Gamma})}{dq^2} = \frac{3}{4}(2A_1^s + A_1^c) - \frac{1}{4}(2A_2^s + A_2^c). \quad (4.65)$$

We prefer to define the normalized forward-backward asymmetry as a ratio of CP-averaged quantities,

$$A_{\text{FB}} = \left[ \int_0^1 - \int_{-1}^0 \right] d \cos \theta_l \frac{d^2(\Gamma - \bar{\Gamma})}{dq^2 d \cos \theta_l} \bigg/ \frac{d(\Gamma + \bar{\Gamma})}{dq^2} = \frac{3}{8}(2S_6^s + S_6^c). \quad (4.66)$$

The CP average is numerically irrelevant in the SM, but makes the connection to experiment more transparent. In addition, this definition is complementary to the forward-backward CP asymmetry [56],

$$A_{\text{FB}}^{\text{CP}} = \left[ \int_0^1 - \int_{-1}^0 \right] d \cos \theta_l \frac{d^2(\Gamma + \bar{\Gamma})}{dq^2 d \cos \theta_l} \bigg/ \frac{d(\Gamma + \bar{\Gamma})}{dq^2} = \frac{3}{8}(2A_6^s + A_6^c). \quad (4.67)$$

Additional well-established observables are the  $K^*$  longitudinal and transverse po-

#### 4. $B \rightarrow K^* \mu^+ \mu^-$

---

larization fractions  $F_L$  and  $F_T$ , already discussed in the context of the neutral decay  $B \rightarrow K^* \nu \bar{\nu}$  in chapter 3. They read in terms of  $S_i^{(a)}$  and  $A_i^{(a)}$

$$F_L = -S_2^c, \quad F_T = 4S_2^s. \quad (4.68)$$

The well-known relation  $F_T = 1 - F_L$  is then a consequence of the fact that in the limit of vanishing lepton mass, no scalar polarizations are allowed and thus the  $K^*$  has to be either longitudinally or transversally polarized.

In refs. [88, 90], the transverse asymmetries  $A_T^{(i)}$  have been introduced, which have a less direct relation to the experimentally observable angular coefficients. They can be expressed in terms of our observables as

$$\begin{aligned} A_T^{(2)} &= \frac{S_3}{2S_2^s}, \\ A_T^{(3)} &= \left( \frac{4S_4^2 + S_7^2}{-2S_2^c(2S_2^s + S_3)} \right)^{1/2}, \\ A_T^{(4)} &= \left( \frac{S_5^2 + 4S_8^2}{4S_4^2 + S_7^2} \right)^{1/2}. \end{aligned} \quad (4.69)$$

### 4.6.2 Integrated Observables

For experimental reasons it is sometimes useful to define integrated observables:

$$\langle S_i^{(a)} \rangle = \int_{1 \text{ GeV}^2}^{6 \text{ GeV}^2} dq^2 \left( I_i^{(a)} + \bar{I}_i^{(a)} \right) / \int_{1 \text{ GeV}^2}^{6 \text{ GeV}^2} dq^2 \frac{d(\Gamma + \bar{\Gamma})}{dq^2}, \quad (4.70)$$

$$\langle A_i^{(a)} \rangle = \int_{1 \text{ GeV}^2}^{6 \text{ GeV}^2} dq^2 \left( I_i^{(a)} - \bar{I}_i^{(a)} \right) / \int_{1 \text{ GeV}^2}^{6 \text{ GeV}^2} dq^2 \frac{d(\Gamma + \bar{\Gamma})}{dq^2}. \quad (4.71)$$

There are two reasons for choosing the upper bound  $q^2 \leq 6 \text{ GeV}^2$ : First, at higher  $q^2$  the charmonium resonances with  $B \rightarrow K^* \psi^{(\prime)} (\rightarrow \ell^+ \ell^-)$  dominate the distribution. Second, QCD factorization (see chapter (4.5)) does not work for large  $q^2$ . The lower bound,  $1 \text{ GeV}^2 \leq q^2$ , avoids (unknown) resonance contributions from  $\rho$  or other mesons.

### 4.6.3 Zero crossings

The zero crossings of the differential observables are largely insensitive to uncertainties in the hadronic form factors, making them powerful observables [95]. In the SM, to

leading order only  $S_4$ ,  $S_5$  and  $S_{6s}$  have zero crossings, which are implicitly given by the following simple relations:

- $S_4$ :

$$C_{10}^2 q^2 + \left( 2C_7 m_b \frac{\mathcal{B}_{T,0}}{\mathcal{B}_0} + C_9^{\text{eff}} \sqrt{q^2} \right) \left( 2C_7 m_b \frac{\mathcal{B}_{T,2}}{\mathcal{B}_2} + C_9^{\text{eff}} \sqrt{q^2} \right) = 0 \quad (4.72)$$

- $S_5$ :

$$C_7 m_b \left( \frac{\mathcal{B}_{T,0}}{\mathcal{B}_0} + \frac{\mathcal{B}_{T,1}}{\mathcal{B}_1} \right) + C_9^{\text{eff}} \sqrt{q^2} = 0 \quad (4.73)$$

- $S_{6s}$ :

$$C_7 m_b \left( \frac{\mathcal{B}_{T,1}}{\mathcal{B}_1} + \frac{\mathcal{B}_{T,2}}{\mathcal{B}_2} \right) + C_9^{\text{eff}} \sqrt{q^2} = 0 \quad (4.74)$$

Using the SCET relations, eq. (2.26) yields immediately the following predictions:

$$q_0^2(S_4) = -\frac{2C_7 m_b m_B (2C_7 m_b + C_9 m_B)}{m_B (C_{10}^2 + C_9^2) + 2C_7 C_9 m_b}, \quad (4.75)$$

$$q_0^2(S_5) = -\frac{C_7 m_b m_B^2}{C_7 m_b + C_9 m_B}, \quad (4.76)$$

$$q_0^2(S_{6s}) = -\frac{2C_7 m_b m_B}{C_9}. \quad (4.77)$$

We note that the zero crossings of our observables are related to those of the alternative set proposed in [88, 90]:

$$\frac{m_B^2 q_0^2(S_6)}{2m_B^2 - q_0^2(S_6)} = q_0^2(A_T^3), \quad (4.78)$$

$$q_0^2(S_4) = q_0^2(A_T^3), \quad (4.79)$$

$$q_0^2(S_5) = q_0^2(A_T^4). \quad (4.80)$$

The zero of the forward-backward asymmetry has been the focus of many experimental and theoretical studies (see for example refs. [91, 96]) as it is established as being an observable free from hadronic effects and capable of distinguishing between NP scenarios.

## 4.7 Standard Model

In this section we will discuss features of the CP-averaged angular coefficients and the CP asymmetries in the context of the SM. We put special focus on the impact of QCDF

#### 4. $B \rightarrow K^* \mu^+ \mu^-$

---

corrections and the uncertainties and furthermore compare our results to existing studies in the literature. Our predictions for the CP-averaged angular coefficients  $S_i^{(a)}$  in the SM are shown in fig. 4.2.<sup>6</sup> We note the following features:

- $S_1^s$  and  $S_1^c$  have been omitted since the relations  $S_1^s = 3S_2^s$  and  $S_1^c = -S_2^c$  are fulfilled up to lepton-mass effects, which amount to at most 1%.
- $S_{1,2}^{s,c}$  are numerically large as expected.
- $S_3$  is numerically small in the SM since it is approximately proportional to the chirality-flipped Wilson coefficient  $C_7'$ , which is suppressed by a factor  $m_s/m_b$ .
- $S_4, S_5, S_6^s$  are similar in magnitude, but are particularly interesting as they each have a zero in  $q^2$ . The predictions of the zero crossings and  $q^2$  distributions are seen to have small uncertainties, as the normalization results in a cancellation of hadronic effects. In tab. 4.4, we show our predictions for the positions of the zeros of  $S_4, S_5$  and  $S_6^s$ , denoted by  $q_0^2(S_i^{(a)})$  from now on.
- $S_7, S_8$  and  $S_9$  are small as well and have a larger error band as they arise from the imaginary part of the transversity amplitudes.

The impact of the radiative QCDF corrections varies extremely. While, in the observables  $S_{2,3,4,5,6}$ , they are mere corrections to the leading-order result, they are the dominant contribution in  $S_{7,8,9}$  and  $A_i$ . This is due to the fact that the first class of observables is largely independent of weak or strong phases, the latter are built of imaginary parts and thus sensitive to the strong phases induced by  $O(\alpha_s)$  corrections in QCDF. The impact of lepton mass effects is similarly diverse. For the most observables they are corrections in the 1 % range, others, like  $I_{6c}$ , are only present if the lepton mass is kept finite.

We proceed by listing all sources of uncertainties and our respective treatment and assumptions:

- The uncertainty due to the form factors is estimated by varying the Borel parameter and continuum threshold as discussed in sec. 2.3.
- The renormalization scale uncertainty is found by varying  $\mu$  between 4.0 and 5.6 GeV, where  $\mu$  is the scale at which the Wilson coefficients,  $\alpha_s$  and the  $\overline{\text{MS}}$  masses are evaluated.

---

<sup>6</sup>The discontinuity in some of the error bands just below 6 GeV<sup>2</sup> is an unphysical artifact resulting from small charm quark masses  $\sim 1.2$  GeV allowed in the estimation of the error. This feature was already observed in ref. [85].

$B$ parameters			
$f_B$ [97]	$\lambda_B(\mu_h)$ [98]	$\mu_h$	
200(25) MeV	0.51(12) GeV	2.2 GeV	
$K^*$ parameters			
$f_{K^*}^{\parallel}$	$f_{K^*}^{\perp}(2\text{GeV})$	$a_1^{\perp,\parallel}(2\text{GeV})$	$a_2^{\perp,\parallel}(2\text{GeV})$
220(5) MeV	163(8) MeV	0.03(3)	0.08(6)
quark masses			
$m_b(m_b)$ [99]	$m_c(m_c)$ [99]	$m_t(m_t)$ [31]	
4.20(4) GeV	1.30(2) GeV	162.3(1.1) GeV	

**Table 4.3:** Numerical values of hadronic input parameters.  $a_i^{\perp,\parallel}$  are parameters of the twist-2  $K^*$  distribution amplitudes and are taken from ref. [100], from where we also take all higher-twist parameters not included in the table.

- The effect of parametric uncertainties are estimated by varying the hadronic parameters as indicated in tab. 4.3.
- The ratio  $m_c/m_b$  is varied between 0.25 and 0.33.
- The CKM angle  $\gamma$ , which is particularly important for the doubly Cabibbo-suppressed contribution to the CP asymmetries, is considered in the interval between  $60^\circ$  and  $80^\circ$ .

For completeness, in the last row of fig. 4.2 we also show the CP averaged dilepton mass distribution  $d(\Gamma + \bar{\Gamma})/dq^2$  and the observables  $A_T^{(3)}$  and  $A_T^{(4)}$  defined in ref. [88], see sec. 4.6.3. Our results for all these observables compare well to those in the literature. However, we stress that the peak in  $A_T^{(4)}$  indicates a severe shortcoming of its definition. It originates in the zero crossing of the denominator of  $A_T^{(4)}$  (c.f. eq. (4.69)) and results in a strong amplification of the theoretical uncertainty both in the position of the peak and its height.

Our observables  $S_i$  and  $A_i$ , in contrast, are not affected by accidental and delicate cancellations in the denominator, as the normalization of  $d\Gamma/dq^2$  has by definition no zeros in the range of  $q^2$  considered. In particular, no complications arise if the observables  $S_4$  and  $S_5$  are considered instead of  $A_T^{(3)}$  and  $A_T^{(4)}$ .

As explained in sec. 4.6.1, the CP asymmetries are close to zero in the SM, which is evident from fig. 4.3, where we show all the  $A_i^{(a)}$  (again except for  $A_1^{s,c}$ ) and the CP asymmetry in the decay distribution,  $A_{\text{CP}}$ . Our results are in good agreement with

#### 4. $B \rightarrow K^* \mu^+ \mu^-$

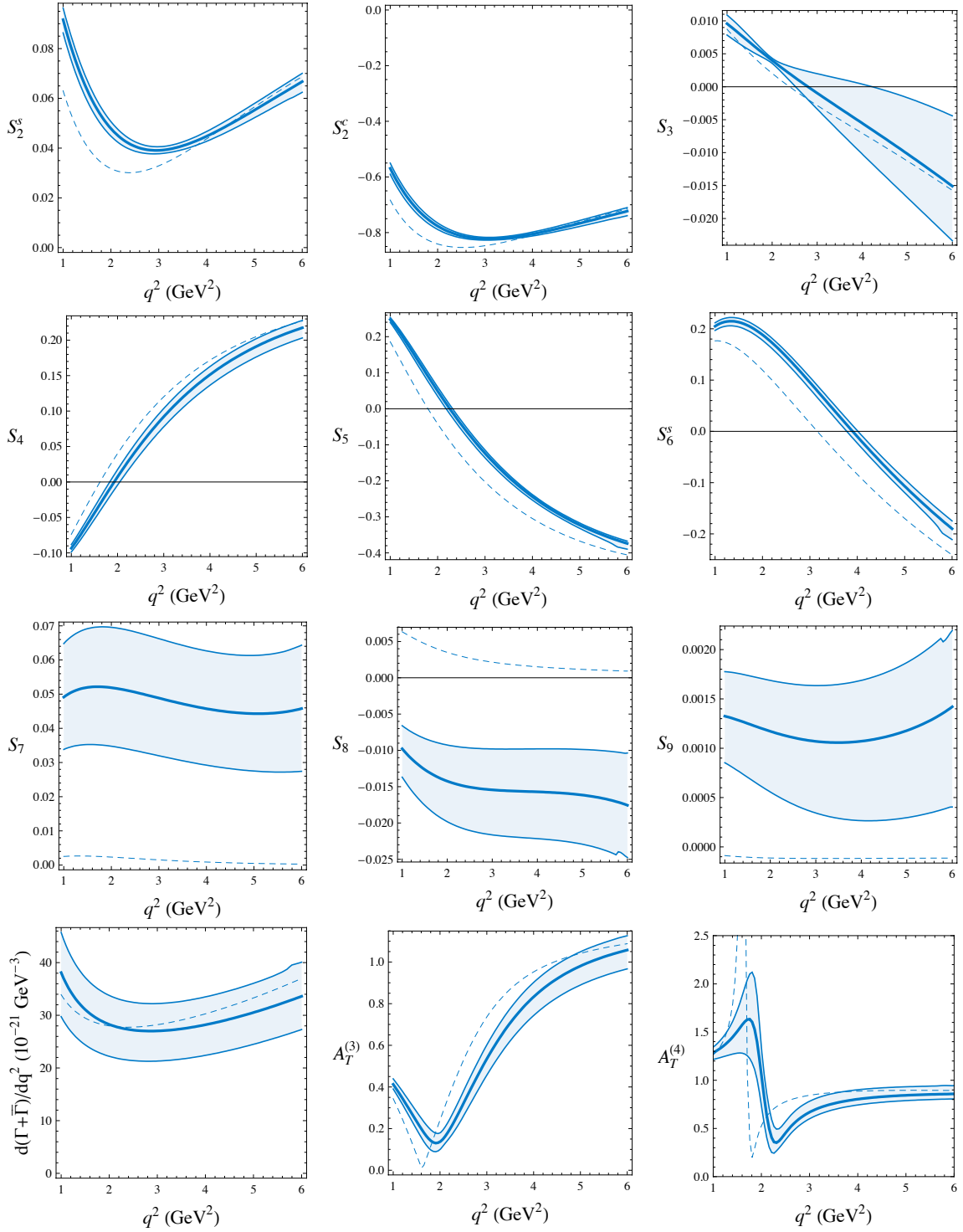


**Figure 4.2:** CP-averaged angular coefficients  $S_i^{(a)}$ , CP-averaged dilepton mass distribution  $d(\Gamma + \bar{\Gamma})/dq^2$  and transverse asymmetries  $A_T^{(3,4)}$  in the SM as a function of  $q^2$ . The dashed lines are the leading-order (LO) contributions, obtained in naïve factorization. The thick solid lines are the full next-to-leading order (NLO) predictions from QCD factorization (QCDF), as described in sec. 4.5. The blue band defines the total error for the NLO result as described in the text.

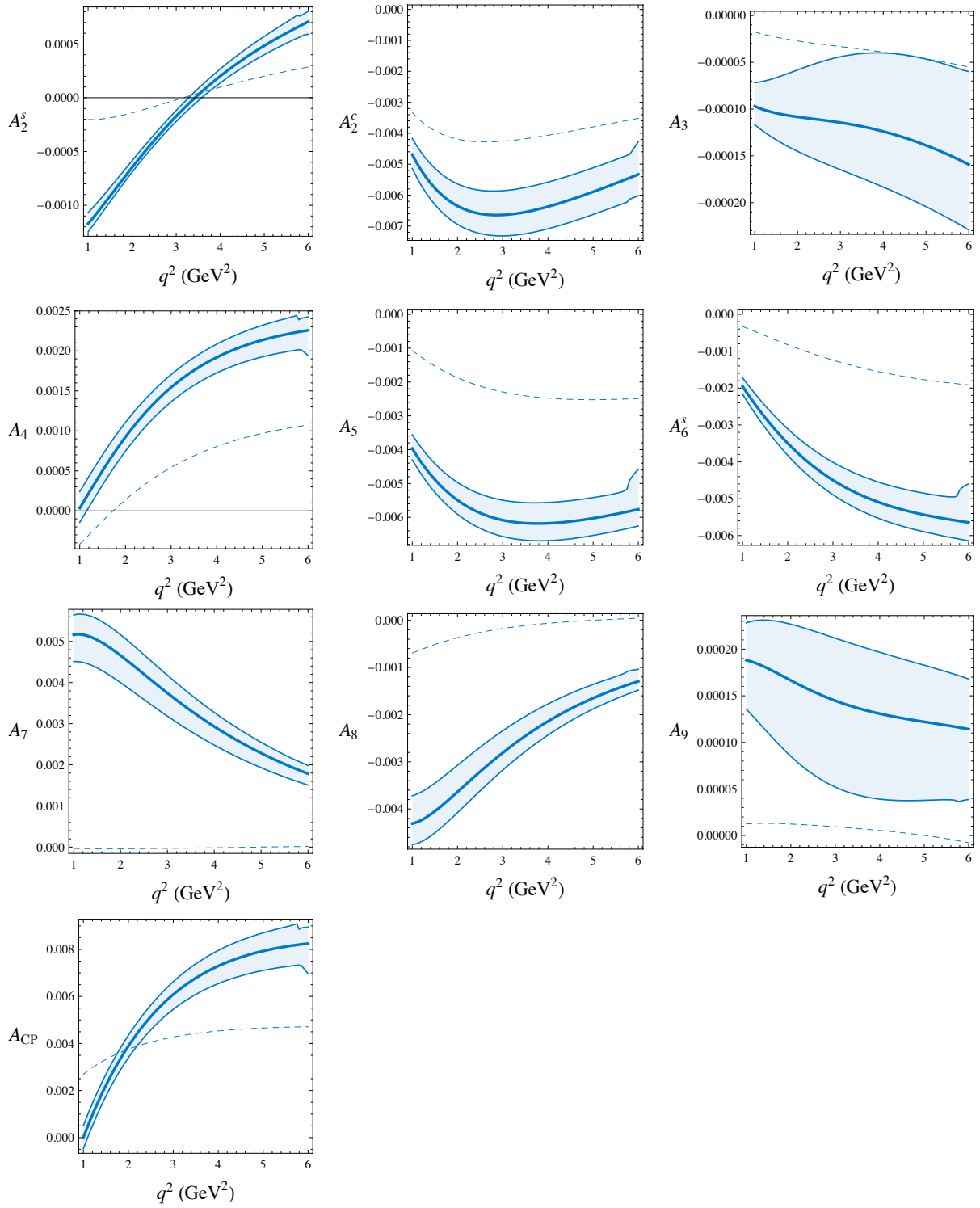


**Figure 4.3:** CP asymmetries  $A_i^{(a)}$  and  $A_{CP}$  in the SM as a function of  $q^2$ . The meaning of the curves and bands is as in fig. 4.2.

ref. [89], but do not coincide exactly. This is mainly due to the use of the full form factors in this analysis instead of the soft form factors and partly due to minor deviation in numerical input parameters. In view of the relative smallness of the differences and the absolute smallness of the CP asymmetries in the SM, these discrepancies become irrelevant once large NP contributions dominate these observables.

In tab. 4.5, we list our predictions for the  $q^2$ -integrated CP-averaged angular coefficients and CP asymmetries as defined in eqs. (4.70) and (4.71).  $\langle S_2^c \rangle$ ,  $\langle S_6^s \rangle$  and  $\langle A_{CP} \rangle$  can be directly compared to existing experimental results from BaBar and Belle [101, 102].

## 4.8 Model-independent Analysis

The Wilson coefficients in the effective theory (4.1) parametrize most generally NP effects under the assumption of a SM like low energy particle content. Before entering a model specific discussion of the observables, it is instructive to investigate which statements can be made already on the ground of the Wilson coefficients.

In the context of this discussion the Wilson coefficients can be grouped into three classes:

- Dipole coefficients:  $C_7$ ,  $C_7'$ ,  $C_8$  and  $C_8'$ . The role of the gluon dipole operators is subleading in the decay considered.
- Semileptonic coefficients:  $C_9$ ,  $C_9'$ ,  $C_{10}$  and  $C_{10}'$ .
- Scalar coefficients:  $C_S - C_S'$  and  $C_P - C_P'$ .

In tab. 4.6 we compile the observables being most affected by a significant change of a given coefficient. In tab. 4.7 we show, on the other hand, which Wilson coefficients should be altered to produce a large effect in specific observables.

We observe:

- $C_7$ ,  $C_7'$ ,  $C_9$ ,  $C_9'$ ,  $C_{10}$  and  $C_{10}'$  can induce large effects in many observables, or at least in those that do not require the presence of strong phases. To be precise, the  $A_i$  are mainly induced by imaginary parts of the Wilson coefficients, while the  $S_i$  are induced by their real parts.

Obs.	$S_4$	$S_5$	$S_6^s$
$q_0^2$ [GeV <sup>2</sup> ]	$1.94_{-0.10}^{+0.12}$	$2.24_{-0.08}^{+0.06}$	$3.90_{-0.12}^{+0.11}$

**Table 4.4:** Predictions for the zero positions  $q_0^2(S_i^{(a)})$  of  $S_4$ ,  $S_5$  and  $S_6^s$  in the SM.

Obs.	$10^{-2} \times \dots$	Obs.	$10^{-2} \times \dots$	Obs.	$10^{-3} \times \dots$	Obs.	$10^{-3} \times \dots$
$\langle S_1^s \rangle$	$16.0_{-0.6}^{+0.6}$	$\langle S_5 \rangle$	$-14.2_{-1.2}^{+0.8}$	$\langle A_1^s \rangle$	$-0.2_{-0.1}^{+0.2}$	$\langle A_5 \rangle$	$-5.7_{-0.5}^{+0.6}$
$\langle S_1^c \rangle$	$79.3_{-0.8}^{+0.8}$	$\langle S_6^s \rangle$	$3.5_{-1.1}^{+0.8}$	$\langle A_1^c \rangle$	$6.3_{-0.8}^{+0.7}$	$\langle A_6^s \rangle$	$-4.5_{-0.4}^{+0.5}$
$\langle S_2^s \rangle$	$5.3_{-0.2}^{+0.2}$	$\langle S_7 \rangle$	$4.8_{-1.7}^{+1.7}$	$\langle A_2^s \rangle$	$-0.1_{-0.0}^{+0.1}$	$\langle A_7 \rangle$	$3.4_{-0.5}^{+0.4}$
$\langle S_2^c \rangle$	$-76.6_{-0.7}^{+0.7}$	$\langle S_8 \rangle$	$-1.5_{-0.6}^{+0.6}$	$\langle A_2^c \rangle$	$-6.1_{-0.6}^{+0.7}$	$\langle A_8 \rangle$	$-2.6_{-0.3}^{+0.4}$
$\langle S_3 \rangle$	$-0.3_{-0.3}^{+0.4}$	$\langle S_9 \rangle$	$0.1_{-0.1}^{+0.1}$	$\langle A_3 \rangle$	$-0.1_{-0.1}^{+0.1}$	$\langle A_9 \rangle$	$0.1_{-0.1}^{+0.1}$
$\langle S_4 \rangle$	$10.1_{-1.2}^{+1.0}$			$\langle A_4 \rangle$	$1.5_{-0.2}^{+0.2}$	$\langle A_{CP} \rangle$	$5.9_{-0.6}^{+0.6}$

**Table 4.5:** Predictions for the integrated CP-averaged angular coefficients  $\langle S_i^{(a)} \rangle$  (in units of  $10^{-2}$ ) and the integrated CP asymmetries  $\langle A_i^{(a)} \rangle$  (in units of  $10^{-3}$ ) in the SM. Note the different normalization of the  $\langle A_i^{(a)} \rangle$  with respect to ref. [89], see footnote 5.

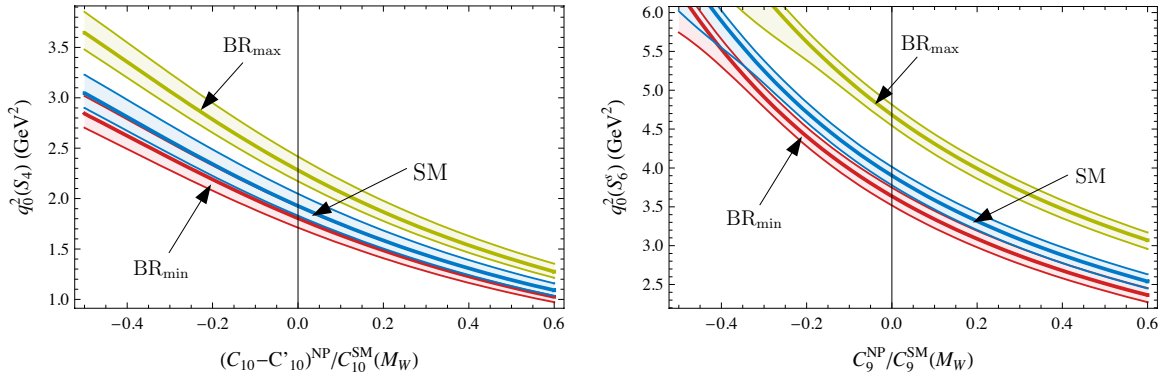


**Figure 4.4:** Left: correlation between  $q_0^2(S_4)$ , the position of the zero of  $S_4$ , and the NP contribution to  $C_{10} - C'_{10}$ . Right: correlation between  $q_0^2(S_6^s)$  and the NP contribution to  $C_9$ . We use the branching ratio for  $B \rightarrow X_s \gamma$  to constrain the NP contributions to  $C_7$ . The green (red) band corresponds to a value of  $\text{BR}(B \rightarrow X_s \gamma)$  at the upper (lower) end of the experimental  $2\sigma$  range, the blue band to SM values for  $C_7$ .

- Only the primed coefficients  $C'_7$ ,  $C'_9$  and  $C'_{10}$  can significantly affect the observables  $S_3$  and  $A_9$ . As can be seen from eq. (4.69),  $S_3$  corresponds to the transverse asymmetry  $A_T^{(2)}$  and the impact of NP physics contributions to  $C'_7$  on this observable has been studied for example in refs. [88, 90, 93].
- The scalar operators affect mainly  $S_6^c$  and the branching ratio for  $B_s \rightarrow \mu^+ \mu^-$ . This implies interesting correlations between these two observables as discussed below.

As mentioned before (tab. 4.7) the zero-crossing of  $S_4$ ,  $q_0^2(S_4)$ , is largely sensitive to  $C_7$ ,  $C'_7$ ,  $C_{10}$  and  $C'_{10}$ . These Wilson coefficients of course enter other observables,

#### 4. $B \rightarrow K^* \mu^+ \mu^-$

Wilson coefficients	largest effect in
$C_7, C_7'$	$S_1^s, S_1^c, S_2^s, S_2^c, S_3, S_4, S_5, S_6^s,$ $A_7, A_8, A_9,$ $\text{BR}(B \rightarrow X_s \gamma), \text{BR}(B \rightarrow X_s \mu^+ \mu^-)$
$C_9, C_9', C_{10}, C_{10}'$	$S_1^s, S_1^c, S_2^s, S_2^c, S_3, S_4, S_5, S_6^s,$ $A_7, A_8, A_9,$ $\text{BR}(B \rightarrow X_s \mu^+ \mu^-)$
$C_S - C_S'$	$S_6^c,$ $\text{BR}(B_s \rightarrow \mu^+ \mu^-)$
$C_P - C_P'$	$S_1^c + S_2^c,$ $\text{BR}(B_s \rightarrow \mu^+ \mu^-)$

**Table 4.6:** The Wilson coefficients relevant in  $B \rightarrow K^* \mu^+ \mu^-$  and the observables they have the largest impact on.

in particular the experimentally constrained decays  $B \rightarrow X_s \gamma$  and  $B \rightarrow X_s \mu^+ \mu^-$ . We consider in the following the implication of these constraints, first under the assumption of a real  $C_7$  and then for complex  $C_7$ . We neglect in both cases the effects in  $C_7'$ .

For real  $C_7$ , the current experimental value of the branching ratio of  $B \rightarrow X_s \gamma$  provides a constraint on  $C_7$ , while it leaves  $C_{10}$  and  $C_{10}'$  unconstrained. In fig. 4.4, we show the dependence of the zero of  $S_4$  on the potential NP modifications to  $C_{10} - C_{10}'$ , which is the only combination of Wilson coefficients entering the observable. Its strong dependence on  $C_{10} - C_{10}'$  translates a future measurement of the zero crossing directly in very interesting information about these Wilson coefficients. A similar reasoning holds for  $S_6^s$ , where the role of  $C_{10}$  and  $C_{10}'$  is played by  $C_9$ . We find again a strong dependence on  $C_9$ , and for real values of  $C_7$  this would be a clean way to determine information about a possible NP contribution to  $C_9$  as seen in fig. 4.4.

For complex  $C_7$ , the bound from  $B \rightarrow X_s \gamma$  is weakened, allowing large effects in the zero-crossings. In fact, large values of  $\text{Im}(C_7)$  require large positive contributions to  $\text{Re}(C_7)$  that interfere destructively with  $C_7^{\text{SM}}$  to fulfill the constraint of  $B \rightarrow X_s \gamma$ . In such kind of setup  $B \rightarrow X_s \mu^+ \mu^-$  is largely enhanced, thus effectively setting a new upper bound on  $\text{Re}(C_7)$ . In the left-hand plot in fig. 4.5, we show these combined constraints in the complex  $C_7$  plane. In the right-hand plot in fig. 4.5, we show the dependence of  $q_0^2(S_6^s)$  on  $\text{Re}(C_7)$  in the thus constrained allowed range. Exactly the large positive contributions to  $\text{Re}(C_7)$ , which are allowed in the presence of phases in  $C_7^{\text{NP}}$ , then unambiguously shift

Observable	mostly affected by
$S_1^s, S_1^c, S_2^s, S_2^c$	$C_7, C_7', C_9, C_9', C_{10}, C_{10}'$
$S_3$	$C_7', C_9', C_{10}'$
$S_4$	$C_7, C_7', C_{10}, C_{10}'$
$S_5$	$C_7, C_7', C_9, C_{10}'$
$S_6^s$	$C_7, C_9$
$A_7$	$C_7, C_7', C_{10}, C_{10}'$
$A_8$	$C_7, C_7', C_9, C_9', C_{10}'$
$A_9$	$C_7', C_9', C_{10}'$
$S_6^c$	$C_S - C_S'$

**Table 4.7:** The most interesting angular observables in  $B \rightarrow K^* \mu^+ \mu^-$  and the Wilson coefficients they are most sensitive to.

the zeros of  $S_4$ ,  $S_5$  and  $S_6^s$  towards lower values. We observe that the allowed range for  $q_0^2(S_6^s)$  is greatly enhanced in the case of complex  $C_7$ .

In contrast to  $S_4$  and  $S_6^s$ ,  $S_5$  depends on Wilson Coefficients –  $C_7$ ,  $C_7'$ ,  $C_9$  and  $C_{10}'$  – which do not enter  $B \rightarrow X_s \gamma$  and  $B \rightarrow X_s \mu^+ \mu^-$  directly. Thus a measurement of  $q_0^2(S_5)$  does not provide immediate access to a specific form factor combination, but could provide a consistency check with  $C_{10} - C_{10}'$  and  $C_9$  determined from  $S_4$  and  $S_6$ , provided  $C_7, C_7'$  are real. In addition, this might allow to disentangle the effects of  $C_{10}^{\text{NP}}$  and  $C_{10}'^{\text{NP}}$  in fig. 4.4.

Previous studies of scalar operators in the context of  $B \rightarrow K^*(\rightarrow K\pi)\mu^+\mu^-$  neglected lepton mass effect and came to the conclusion that these operators have an irrelevant impact. Keeping the lepton mass finite, however, induces an extra observable sensitive to scalar currents. This observable can serve as a precision null-test of the SM and allows in principle to distinguish between different NP models.

As seen in the case of  $S_4$  and  $S_6$  it is very useful to combine information on the Wilson coefficients from other decays. The most stringent constraint on  $C_{S,P}^{(\prime)}$  comes from the measurement of  $B_s \rightarrow \mu^+ \mu^-$ , which is strongly helicity suppressed in the SM, with a predicted branching ratio of [103]

$$\text{BR}(B_s \rightarrow \mu^+ \mu^-) = (3.2 \pm 0.3) \times 10^{-9}. \quad (4.81)$$

The most recent published experimental upper bound still lies, at the 95% confidence

#### 4. $B \rightarrow K^* \mu^+ \mu^-$

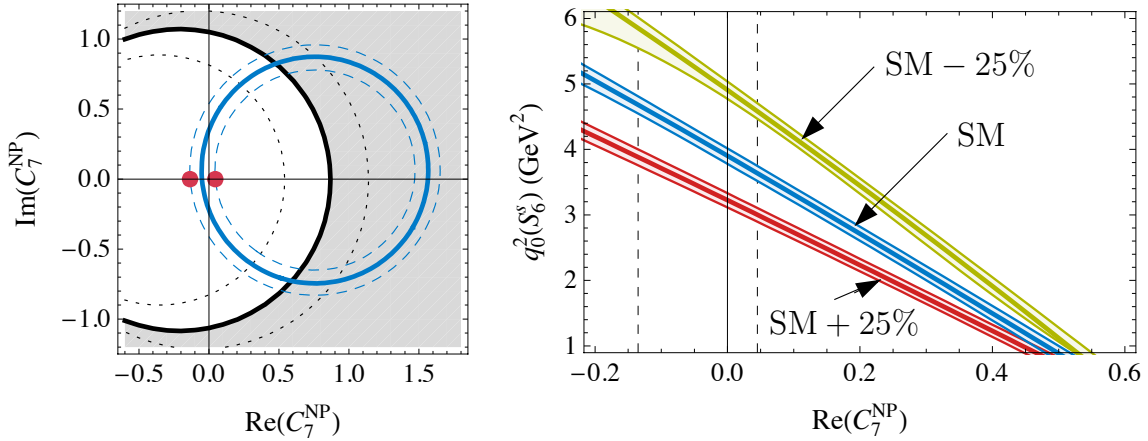


**Figure 4.5:** Left: Experimental constraints on the NP contribution to  $C_7$ . The blue circles show the constraint from the central and  $\pm 2\sigma$  values of  $\text{BR}(B \rightarrow X_s \gamma)$ , assuming  $C_7^{\prime \text{NP}} = 0$ . The black circle corresponds to the  $2\sigma$  bound from  $\text{BR}(B \rightarrow X_s \ell^+ \ell^-)$ , assuming  $C_{10}^{(\prime) \text{NP}} = 0$ . The solid thick and the dotted lines have been obtained assuming SM and SM $\pm 25\%$  values for  $C_9$ , respectively. Right: Correlation of the zero in  $S_6^s$  with the NP contribution to  $\text{Re}(C_7)$ . The blue, red and green bands indicate SM, SM+25% and SM-25% values for  $C_9$  with the associated theoretical uncertainty. The vertical dashed lines correspond to the upper and lower bounds on  $\text{Re}(C_7)$  in the absence of an imaginary part of  $C_7$ . (The corresponding points in the left-hand plot are highlighted by red dots.) For an arbitrary imaginary part, the upper bound on  $\text{Re}(C_7)$  is removed, and  $q_0^2(S_6^s)$  can be at or below  $1 \text{ GeV}^2$ .

level, one order of magnitude above the SM [59]:

$$\text{BR}(B_s \rightarrow \mu^+ \mu^-) < 5.8 \times 10^{-8}. \quad (4.82)$$

However, in many models, e.g. the MSSM at large  $\tan \beta$ , this branching ratio can be greatly enhanced.

In a generic NP model, the branching ratio is given by

$$\text{BR}(B_s \rightarrow \mu^+ \mu^-) \propto \left[ |S|^2 \left( 1 - \frac{4m_\mu^2}{m_{B_s}^2} \right) + |P|^2 \right], \quad (4.83)$$

where

$$S = \frac{m_{B_s}^2}{2} (C_S - C'_S), \quad P = \frac{m_{B_s}^2}{2} (C_P - C'_P) + m_\mu (C_{10} - C'_{10}). \quad (4.84)$$

Considering the experimental bound in eq. (4.82), these formulae translate in the ap-

proximate bounds

$$|C_S - C'_S| \lesssim 0.12 \text{ GeV}^{-1}, \quad -0.09 \text{ GeV}^{-1} \lesssim C_P - C'_P \lesssim 0.15 \text{ GeV}^{-1}, \quad (4.85)$$

barring large NP contributions to the Wilson coefficients  $C_{10}^{(\prime)}$ .

As seen from the formulae for the angular coefficients, eqs. (4.35)–(4.46), the only terms in which  $C_S^{(\prime)}$  and  $C_P^{(\prime)}$  are not suppressed by the lepton mass enter in the angular coefficient  $I_1^c$ . However, due to the small size of the Wilson coefficients themselves, see eq. (4.85), these terms turn out to be numerically irrelevant in general once the bound from  $B_s \rightarrow \mu^+ \mu^-$  is taken into account.

The pseudoscalar operators do not contribute to any other angular coefficient, implying that they are indeed irrelevant in the phenomenological study of  $B \rightarrow K^*(\rightarrow K\pi)\mu^+ \mu^-$ . For the scalar operators, however, the situation is different, because of the new angular coefficient  $I_6^c$ , eq. (4.42), which is directly proportional to the real part of  $(C_S - C'_S)$  and thus vanishes in the SM. So, although numerically small, this angular coefficient is an appealing observable because any measurement of a non-zero value would constitute an unambiguous signal of scalar currents.

This is in contrast to the process  $B_s \rightarrow \mu^+ \mu^-$ , where a large enhancement of the branching ratio compared to the SM could be caused by both scalar and pseudoscalar currents. In addition, the measurement of a non-zero  $S_6^c$  (the CP-averaged counterpart of  $I_6^c$ ) would allow to determine the sign of  $\text{Re}(C_S - C'_S)$ . In fact, by a combined study of  $B_s \rightarrow \mu^+ \mu^-$  and the observable  $S_6^c$ , one would be able to constrain the relative sizes of the scalar and pseudoscalar Wilson coefficients, which can serve to distinguish different models of NP.

To summarize, while pseudoscalar operators are numerically irrelevant in the decay  $B \rightarrow K^*(\rightarrow K\pi)\mu^+ \mu^-$ , a study of the angular distribution allows to probe the scalar sector of a theory beyond the SM, in a way that is theoretically clean and complementary to  $B_s \rightarrow \mu^+ \mu^-$ .

## 4.9 Specific New Physics Scenarios

The discussion presented in the previous section concentrated on the SM prediction of several observables, experimental deviations would signal the presence of physics beyond the SM. In this section we take a somewhat different point of view and analyze the impact of specific NP scenarios. For this analysis we choose benchmark parameter points to discuss, maximal and minimal, and discuss on the basis of these point correlations

with other flavor observables.

### 4.9.1 Minimal Flavor Violation

While the absence of CP-violating phases beyond the SM is one of the underlying assumptions in the MFV framework [54, 55], the NP contributions to the Wilson coefficients of the primed operators can be neglected because they are suppressed by  $m_s/m_b$ . Therefore no visible departures from the SM model predictions are expected in CP asymmetries and  $S_3$ . In fact, we only find effects in  $S_{1,2}^{s,c}$ ,  $S_4$ ,  $S_5$  and  $S_6^s$ .

Model-independent studies within the MFV framework show that large NP contributions to the Wilson coefficients  $C_7$ ,  $C_8$ ,  $C_9$  and  $C_{10}$  are still allowed [104] by all available constraints. In particular, scenarios in which the sign of these Wilson coefficients is flipped with respect to the SM cannot yet be excluded.

### 4.9.2 Minimal Flavor Violating MSSM

In the Minimal Flavor Violating MSSM (MFV MSSM), NP contributions to  $C_9$  and  $C_{10}$  are known to be typically very small [105, 106]. This feature, which is also generally true for many NP model, puts due to the data on  $\text{BR}(B \rightarrow X_s \gamma)$  and  $\text{BR}(B \rightarrow X_s \mu^+ \mu^-)$  a strong constraint on NP effects in  $C_7$  and in particular on a sign flip in  $C_7$  [107]. The consequence of this situation is that the possible effects in  $S_4$ ,  $S_5$  and  $S_6^s$  are not expected to be very large. In fig. 4.6, we show the largest possible effects in these observables, which arise in the following scenarios:

- Scenario MFV<sub>I</sub> (green curves) corresponds to the maximum allowed negative (i.e. constructive) NP contribution to  $C_7$  (i.e.  $C_7^{\text{NP}}$ ) and shifts the zeros of  $S_4$ ,  $S_5$  and  $S_6^s$  to larger values of  $q^2$ .
- Scenario MFV<sub>II</sub> (red curves), corresponds to the largest positive allowed value of  $C_7^{\text{NP}}$  and hence shifts the zeros to smaller values.

The separation in  $q^2$  between these two curves corresponds to the range shown in fig. 4.4 for  $(C_{10}^{\text{NP}} - C_{10}^{\text{SM}}) = 0$  and  $C_9^{\text{NP}} = 0$ , respectively, where the superscript NP denotes the NP contribution to the Wilson coefficient. The most relevant input parameters corresponding to the two scenarios are collected in tab. 4.8.

As pointed out in [108, 109], the shift in the zero crossing of the forward-backward asymmetry in  $B \rightarrow X_s \mu^+ \mu^-$  is highly correlated with a change of the branching ratio of  $B \rightarrow X_s \gamma$  in the MFV MSSM. We show in fig. 4.7 that a similar correlation exists also

Scenario	$\tan \beta$	$m_A$	$m_{\tilde{g}}$	$m_{\tilde{Q}}$	$m_{\tilde{U}}$	$A_{\tilde{t}}$	$\mu$
MFV <sub>I</sub>	28	380	530	800	540	-850	860
MFV <sub>II</sub>	29	530	1000	880	660	880	750

**Table 4.8:** Most relevant parameters of the two MFV MSSM scenarios discussed in the text.  $\tan \beta$  is the ratio of the two Higgs VEVs,  $m_A$  the mass of the pseudoscalar Higgs,  $m_{\tilde{g}}$  is the gluino mass,  $m_{\tilde{Q}}$  is a universal soft mass for the left handed squark doublets,  $m_{\tilde{U}}$  a universal soft mass for the right handed up squarks,  $A_{\tilde{t}}$  is the stop trilinear coupling and  $\mu$  the Higgsino mass parameter. Our conventions for the trilinear coupling are such that the left-right mixing entry in the stop mass matrix is  $(m^2)_{LR} = -m_t(A_{\tilde{t}} + \mu^* \cot \beta)$ . All massive parameters are given in GeV.

for the zero crossings of  $S_4$ ,  $S_5$  and  $S_6^s$  and  $\text{BR}(B \rightarrow X_s \gamma)$ . Any experimental deviation from this correlation would be an indication for either the presence of NP contributions to Wilson coefficients other than  $C_7$  or of new CP-violating phases that lead to complex values of  $C_7$ .

### 4.9.3 Flavor Blind MSSM

Let us now consider the FBMSSM, which is discussed in refs. [110–113]. In this rather restricted version of the MSSM, the CKM matrix is assumed to be the only source of flavor violation, but additional CP violating phases are introduced in the soft sector. The major source of deviations with respect to the SM in this setup are complex NP contributions to the Wilson coefficient  $C_7$ . We discuss two scenarios in which the effects are maximal and a third one, which is relevant in the context of the observable  $S_{\phi K_S}$ , the time dependent CP asymmetry in  $B \rightarrow \phi K_S$ :

- Scenario FBMSSM<sub>I</sub> is characterized by large negative  $\text{Im}(C_7)$ .
- Scenario FBMSSM<sub>II</sub> corresponds to a large positive  $\text{Im}(C_7)$ .
- Scenario FBMSSM<sub>III</sub> gives  $S_{\phi K_S} \simeq 0.4$  close to the experimental central value.

The corresponding input parameters are collected in tab. 4.9.

In the analysis of the CP-averaged angular coefficients in the context of the FBMSSM, we find only pronounced non-SM effects in  $S_{1,2}^{s,c}$ ,  $S_4$ ,  $S_5$ ,  $S_6^s$  and also in  $S_6^c$ . We note that while  $|S_{1,2}^s|$  is enhanced,  $|S_{1,2}^c|$  is suppressed with respect to the SM results. The impact in  $S_4$ ,  $S_5$  and  $S_6^s$  is more distinct, since their zero crossings are significantly shifted towards values of  $q^2$  lower than the SM prediction or they do not even have zero crossings in the allowed kinematic range. We show these effects in fig. 4.8 and note, that these are much

#### 4. $B \rightarrow K^* \mu^+ \mu^-$

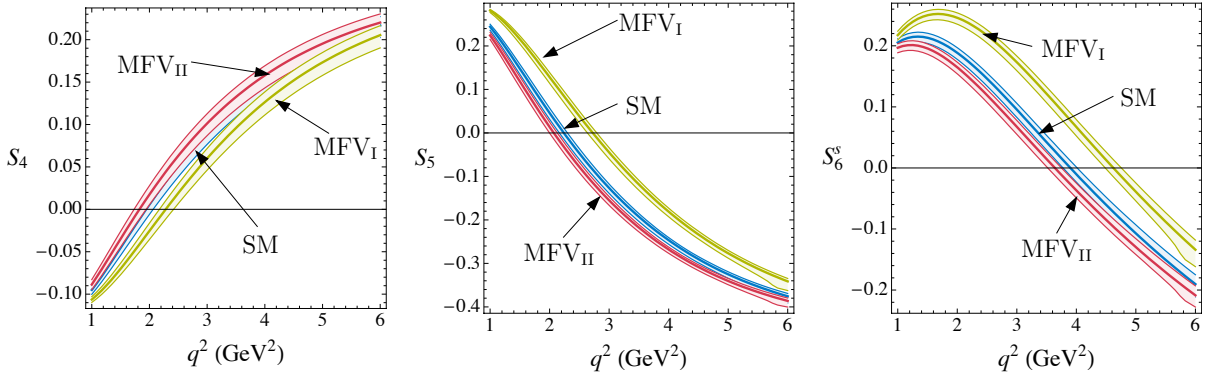


**Figure 4.6:** The observables  $S_4$ ,  $S_5$  and  $S_6^s$  in the SM (blue band) and the MFV MSSM scenarios  $\text{MFV}_{\text{I,II}}$  described in the text.

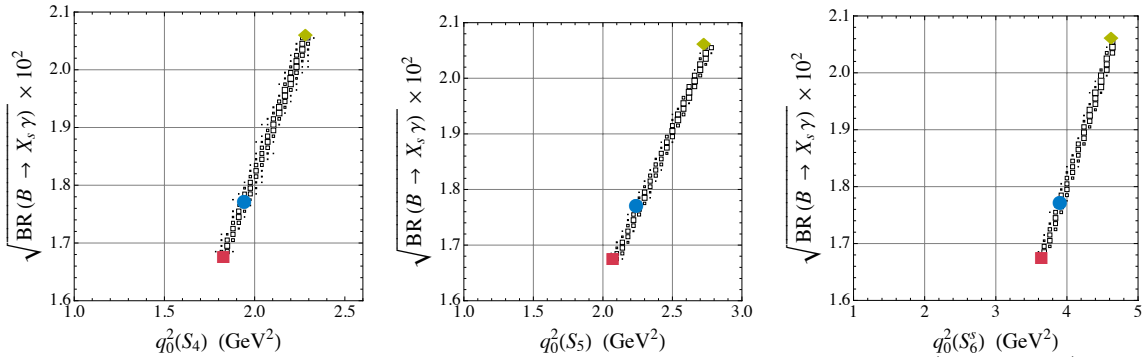


**Figure 4.7:** The correlation between the zeros of  $S_4$ ,  $S_5$  and  $S_6^s$  and  $\text{BR}(B \rightarrow X_s \gamma)$  in the MFV MSSM. The blue circles correspond to the central SM values, while the green diamonds represent scenario  $\text{MFV}_{\text{I}}$  and the red squares scenario  $\text{MFV}_{\text{II}}$ .

larger than those possible in the MFV MSSM (see fig. 4.6). The reason for this was already discussed in Sec. 4.8 in a more general context: large values of  $\text{Im}(C_7)$  lead to large shifts in the zero crossings. On the other hand, the effects in  $S_6^c$  are smaller than the maximal effects found in the model-independent discussion of scalar currents in sec. 4.8. This is due to the fact that the large imaginary part in  $C_7$  implies a large phase for the relevant Wilson coefficient  $C_S$ , even though in the FBMSSM the  $\text{BR}(B_s \rightarrow \mu^+ \mu^-)$  can be close to its experimental upper bound.

It turns out that the most significant departures of CP asymmetries from the SM predictions can be obtained in  $A_{1,2}^s$ ,  $A_5$ ,  $A_6^s$  and especially  $A_7$  and  $A_8$ . The latter are shown in the left and center plot of fig. 4.9. As in the case of the CP-averaged angular coefficients the effects have the origin mainly in the large imaginary part of  $C_7$ . We note also that in this setup, there is a correlation of positive values for  $A_7$  and negative ones for  $A_8$  and vice versa. This observation is even more transparent in terms of integrated asymmetries  $\langle A_7 \rangle$  and  $\langle A_8 \rangle$ . The right plot of fig. 4.9 shows an almost perfect correlation

Scenario	$\tan \beta$	$m_A$	$m_{\tilde{g}}$	$m_{\tilde{Q}}$	$m_{\tilde{U}}$	$A_{\tilde{t}}$	$\mu$	$\text{Arg}(\mu A_{\tilde{t}})$
FBMSSM <sub>I</sub>	40	400	700	380	700	900	150	$-45^\circ$
FBMSSM <sub>II</sub>	40	400	700	380	700	900	150	$50^\circ$
FBMSSM <sub>III</sub>	40	400	700	650	700	900	150	$60^\circ$

**Table 4.9:** Most relevant parameters of the three FBMSSM scenarios discussed in the text. All massive parameters are given in GeV.

between these observables. Any departure from this correlation would indicate additional imaginary parts in either  $C'_7$  or  $C_9^{(\prime)}$  and  $C_{10}^{(\prime)}$ .

In the upper plots of fig. 4.10, we show the correlation between the zeros of  $S_4$ ,  $S_5$  and  $S_6^s$  with the  $b \rightarrow s\gamma$  branching ratio. While the direct proportionality between the zero crossings and  $\text{BR}(B \rightarrow X_s\gamma)$  is lost in the FBMSSM, one still finds an upper bound on the zero crossings for a given value of  $\text{BR}(B \rightarrow X_s\gamma)$ . Both effects are due to the imaginary part of  $C_7$ , that leads to strictly positive enhancement of  $\text{BR}(B \rightarrow X_s\gamma)$ .

Having discussed correlation effects among the CP asymmetries and CP averaged coefficients separately, we give here an example of the interplay of these two classes of observables. We show in the lower plots of fig. 4.10 the zero crossings  $q_0^2(S_4)$ ,  $q_0^2(S_5)$  and  $q_0^2(S_6^s)$  against the integrated asymmetry  $\langle A_7 \rangle$ . One observes that large effects in  $\langle A_7 \rangle$  are correlated with large shifts in the zeros towards lower values.

In order to identify signs in the CP asymmetries which are favored in this model one must include additional observables in the analysis. To this end we also investigate the direct CP asymmetry in the  $b \rightarrow s\gamma$  decay  $A_{\text{CP}}(b \rightarrow s\gamma)$ , the electric dipole moments of the electron and the neutron  $d_e$  and  $d_n$  and the mixing induced CP asymmetry  $S_{\phi_{K_S}}$ . We recall that in [113] strong correlations between these observables have been found. In particular, the desire to explain the anomaly observed in  $S_{\phi_{K_S}}$  through the presence of flavor conserving but CP-violating phases implied a positive  $A_{\text{CP}}(b \rightarrow s\gamma)$ , up to an order of magnitude larger than its SM tiny value and  $d_e, d_n$  at least as large as  $10^{-28} e \text{ cm}$ .

The left plot of fig. 4.11 shows the correlation between  $\langle A_7 \rangle$  and  $S_{\phi_{K_S}}$ . We find that a value of  $S_{\phi_{K_S}} \simeq 0.44$ , as indicated by the present data [114], implies a negative value for  $\langle A_7 \rangle$  in the range  $[-0.2, -0.05]$  and then also a positive value for  $\langle A_8 \rangle$  in the range  $[0.03, 0.11]$ . In addition to the two scenarios discussed above, we have chosen also a third scenario, FBMSSM<sub>III</sub>, indicated as orange triangle in the plots of figs. 4.9, 4.10 and 4.11, that gives  $S_{\phi_{K_S}}$  close to the experimental value. This scenario is shown in figs. 4.9 and 4.8 as the orange bands and we find that while one still can get almost maximal effects in  $\langle A_7 \rangle$  and  $\langle A_8 \rangle$  the effects in  $S_4$ ,  $S_5$  and  $S_6^s$  are much less pronounced. In the center plot

#### 4. $B \rightarrow K^* \mu^+ \mu^-$

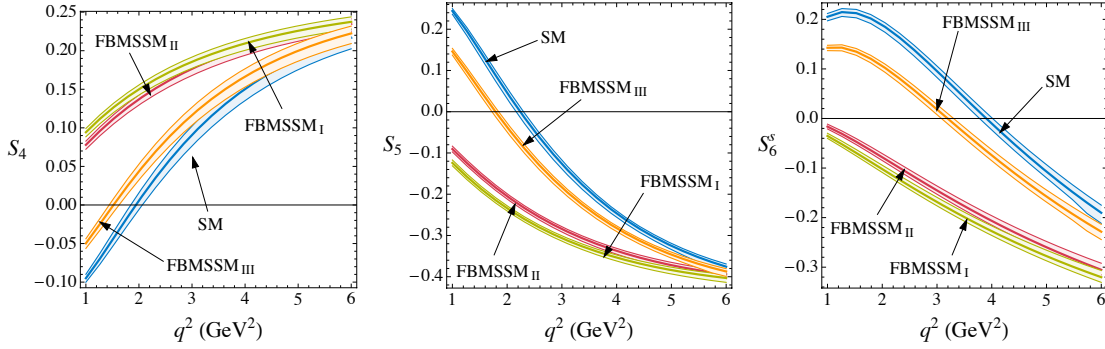


**Figure 4.8:** The observables  $S_4$ ,  $S_5$  and  $S_6^s$  in the SM (blue band) and the three FBSSM scenarios FBSSM<sub>I,II,III</sub>.

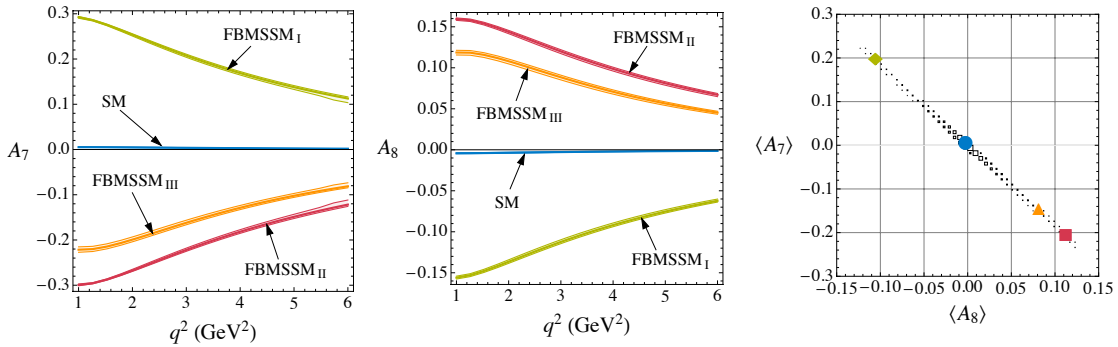


**Figure 4.9:** Left and center plot: CP asymmetries  $A_7$  and  $A_8$  in the SM (blue band) and three FBSSM scenarios as described in the text. Right plot: correlation between the integrated asymmetries  $\langle A_7 \rangle$  and  $\langle A_8 \rangle$  in the FBSSM. Blue circle: SM, green diamond: FBSSM<sub>I</sub>, red square: FBSSM<sub>II</sub>, orange triangle: FBSSM<sub>III</sub>.

of fig. 4.11, we report the correlation between  $\langle A_7 \rangle$  and  $A_{CP}(b \rightarrow s\gamma)$ . One observes that negative values for  $\langle A_7 \rangle$  imply positive values for  $A_{CP}(b \rightarrow s\gamma)$  that can reach values up to  $(5 - 6)\%$ . Finally, the right plot of fig. 4.11 shows the correlation between  $\langle A_7 \rangle$  and the EDM of the electron,  $d_e$  in the FBSSM. We find that large values for  $\langle A_7 \rangle$  necessarily require large values for the electron EDM close to the current upper bound of  $1.6 \times 10^{-27} e \text{ cm}$  [115].

#### 4.9.4 Littlest Higgs with T-Parity

A scan over the free model parameters of the LHT shows that the new physics effects in all observables considered here are mostly small. The largest effects relative to the SM are found in  $A_7$  and  $A_8$  as in the SM their absolute values are at most  $6 \times 10^{-3}$  and  $5 \times 10^{-3}$ , respectively. We consider again sets of parameters LHT<sub>I,II</sub> (with input parameters as given in tab. 4.10) where effects become maximal:

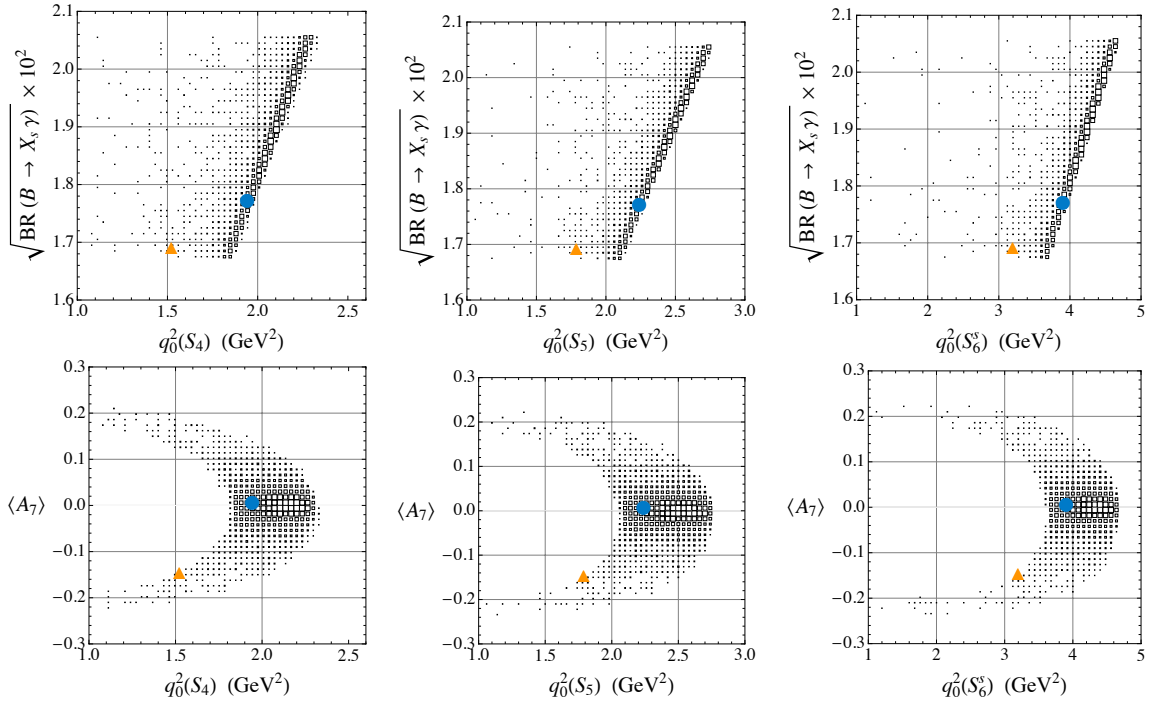


**Figure 4.10:** Correlation between the zeros of  $S_4$ ,  $S_5$  and  $S_6^s$  with the  $b \rightarrow s\gamma$  branching ratio (upper plots) and with the integrated asymmetry  $\langle A_7 \rangle$  (lower plots) in the FBMSM. The blue circles correspond to the SM predictions. The orange triangles correspond to a FBMSM scenario that gives  $S_{\phi K_S}$  close to the central experimental value  $\simeq 0.44$ .

- Scenario LHT<sub>I</sub> corresponds to a LHT parameter point that gives the largest negative NP contribution to  $\text{Im}(C_9)$  and  $\text{Im}(C_{10})$ .
- Scenario LHT<sub>II</sub> curves (red) give the largest positive contribution.

In the left and center plot of fig. 4.12, we show the corresponding asymmetries  $A_7$  and  $A_8$  as functions of  $q^2$  for the two sets of parameters, LHT<sub>I/II</sub>. Enhancement of both asymmetries by a factor of three is possible for low values of  $q^2$  with visible but smaller effects for larger values of  $q^2$ .

It is interesting to compare the results in the LHT just discussed with the effects in the FBMSM. While the LHT effects in  $A_7$  and  $A_8$  the most pronounced, they are still one order of magnitude smaller than the corresponding effects are in the FBMSM. This is due to the role of  $C_7$  in the two models. While it is possible to generate large NP contributions to the imaginary part of  $C_7$  in the FBMSM, this is not possible in LHT model [116]. The effects in the LHT therefore dominantly stem from  $\text{Im}(C_9)$  and  $\text{Im}(C_{10})$ . This in turn leads to a completely different pattern in the correlation between the integrated asymmetries  $\langle A_7 \rangle$  and  $\langle A_8 \rangle$  than that found in the FBMSM (see the

#### 4. $B \rightarrow K^* \mu^+ \mu^-$

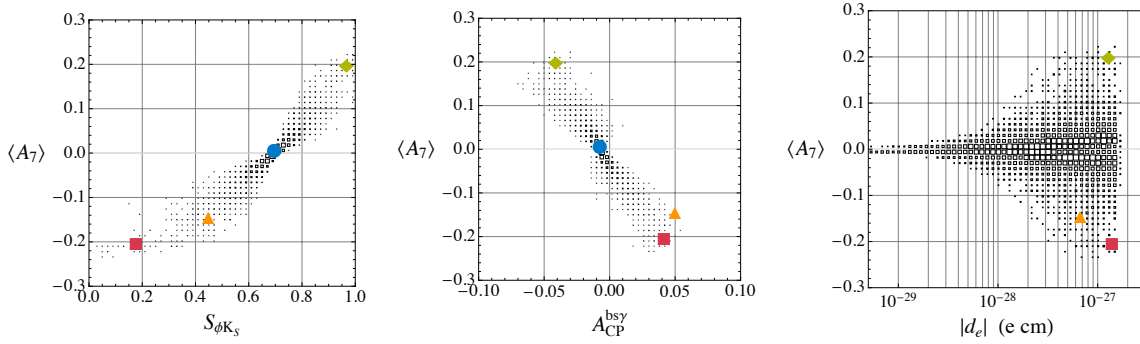


**Figure 4.11:**  $\langle A_7 \rangle$  vs.  $S_{\phi K_S}$  (left plot),  $\langle A_7 \rangle$  vs.  $A_{CP}^{bs\gamma}$  (center plot) and  $\langle A_7 \rangle$  vs.  $d_e$  (right plot) in the FBSSM. The blue circles indicate the SM values, while the green diamonds, red squares and orange triangles correspond to the scenarios FBSSM<sub>I</sub>, FBSSM<sub>II</sub> and FBSSM<sub>III</sub>, respectively.

Scenario	$f$	$x_L$	$m_H^1$	$m_H^2$	$m_H^3$	$\theta_{23}^d$	$\theta_{13}^d$	$\theta_{12}^d$	$\delta_{23}^d$	$\delta_{13}^d$	$\delta_{12}^d$
LHT <sub>I</sub>	1000	0.5	565	1000	770	1.60	2.50	1.35	5.70	4.20	5.80
LHT <sub>II</sub>	1000	0.5	1000	375	425	1.50	1.00	4.75	4.25	0.60	2.85

**Table 4.10:** Parameters of the LHT scenarios LHT<sub>I,II</sub>:  $\theta_{ij}^d$  and  $\delta_{ij}^d$  are the parameters of the CKM-like unitary mixing matrix for the mirror  $d$  quarks,  $m_H^i$  are the masses of the mirror quarks,  $f$  is the high energy scale and  $x_L$  the mixing parameter of the SM top and the T-even top partner (see [116] for details)

right-hand plots in figs. 4.9 and 4.12).

#### 4.9.5 General MSSM

A well-known feature of the MSSM without any further restricting assumptions is that it comes with a plethora of parameters. This makes a general discussion very difficult. We therefore restrict our discussion to four benchmark scenarios:

- GMSSM<sub>I,II</sub>: large contributions  $C_7'$

**Plots:** fig. 4.13, 4.14, 4.15

**Generation:** Such a situation can easily be achieved in the General MSSM if flavor violating terms are only introduced in the left-right sector of the down squark mass. In particular, a  $(\delta_d)_{32}^{LR}$  mass insertion will mostly create contributions to  $C_7'$  by means of down squark – gluino loops, while at the same time leaving the other relevant Wilson coefficients SM like.

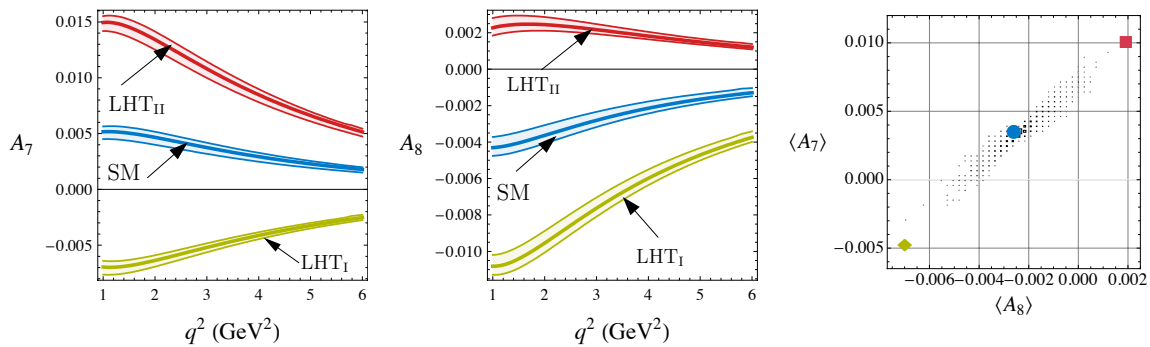


**Figure 4.12:** Left and center plot: CP asymmetries  $A_7$  and  $A_8$  in the SM (blue band) and the LHT scenarios  $LHT_{I,II}$ . Right plot: Correlation between the integrated asymmetries  $\langle A_7 \rangle$  and  $\langle A_8 \rangle$  in the LHT. The blue circle represents the SM, the green diamond scenario  $LHT_I$  and the red square scenario  $LHT_{II}$ .

**Discussion:** fig. 4.13 shows possible effects in  $S_4$ ,  $S_5$  and  $S_6^s$  that arise in this framework due to the real part of  $C_7'$ . In tab. 4.11, we collect the corresponding input parameters. Large imaginary parts of  $C_7'$  lead to sizeable effects in the asymmetries  $A_7$  and  $A_8$  as can be seen in fig. 4.14.

- $GMSSM_{IV}$  : large NP contributions to  $C_7$  and  $C_7'$

**Plot:** Fig. 4.16

**Generation:** This scenario arises from flavor violating down squark masses.

**Discussion:** In contrast to the scenario with NP effects dominantly in  $C_7'$  discussed above, one observes e.g. sizeable effects in the zeros of  $S_5$  and  $S_6^s$  while the zero in  $S_4$  is much less affected. Large non-standard effects in the observables  $S_3$  and  $A_9$  as shown in fig. 4.15. In fact, as already mentioned in sec. 4.8, effects in  $S_3$  and  $A_9$  are characteristic for scenarios with large NP contributions to the primed Wilson coefficients. The large effects in  $S_3$  are driven by the real part of  $C_7'$  and directly correspond to the large effects in the transverse asymmetry  $A_T^{(2)}$  that have been analysed in [88, 90, 93].

- $GMSSM_{III}$  : large NP contributions to  $C_7$ ,  $C_7'$  and  $C_{10}$

**Plot:** fig. 4.16

**Generation:** One possibility to generate large effects in the Wilson coefficient  $C_{10}$  in a supersymmetric framework is through flavor violating entries in the left-right part of the up squark mass [56, 105, 106] through a  $(\delta_u)_{32}^{LR}$  mass insertion.

#### 4. $B \rightarrow K^* \mu^+ \mu^-$

Scenario	$\tan \beta$	$m_A$	$m_{\tilde{g}}$	$m_{\tilde{Q}}$	$m_{\tilde{U}}$	$m_{\tilde{D}}$	$A_{\tilde{u}}$	$A_{\tilde{d}}$	$\mu$	$ (\delta_d)_{32}^{LR} $	$\text{Arg}(\delta_d)_{32}^{LR}$
GMSSM <sub>I</sub>	6	520	500	400	500	380	800	750	470	0.01	$-135^\circ$
GMSSM <sub>II</sub>	5	740	1000	460	1000	390	1500	440	200	0.03	$60^\circ$

**Table 4.11:** Most relevant parameters of the two general MSSM scenarios with large  $C'_7$  as discussed in the text.  $m_{\tilde{D}}$  a universal soft mass for the right handed down squarks,  $A_{\tilde{u}(\tilde{d})}$  universal trilinear couplings for the up (down) squarks and  $(\delta_d)_{32}^{LR}$  the left-right mass insertion that generates large effects in  $C'_7$ . Our conventions for the trilinear coupling are such that the left-right mixing entry in the sbottom mass matrix is  $(m^2)_{LR} = -m_b(A_{\tilde{d}} + \mu^* \tan \beta)$ . All massive parameters are given in GeV.

**Discussion:** These curves show again a qualitatively different behavior in various observables. For example large effects in  $S_3$  and  $A_9$  can be observed, that however do not show a zero in contrast to the red curves discussed above.

#### GMSSM versus FBMSSM

Compared to the framework of the FBMSSM (see fig. 4.8), the shift in the zeros of  $S_4$ ,  $S_5$  and  $S_6^s$  show a completely different pattern. While the zero of  $S_6^s$  remains SM like, a positive shift in  $q_0^2(S_4)$  implies a negative shift in  $q_0^2(S_5)$  and vice versa in scenarios GMSSM<sub>I,II</sub>. Large imaginary parts of  $C'_7$  lead to sizable effects in the asymmetries  $A_7$  and  $A_8$ , but again the pattern of these effects is different to that in the FBMSSM seen in fig. 4.9. As shown in fig. 4.14, a positive (negative)  $A_7$  implies also a positive (negative)  $A_8$ . In particular the correlation plot in the right panel of fig. 4.14 is completely orthogonal to the one in the FBMSSM (see fig. 4.9) and thus a clear distinction between these two frameworks is possible.

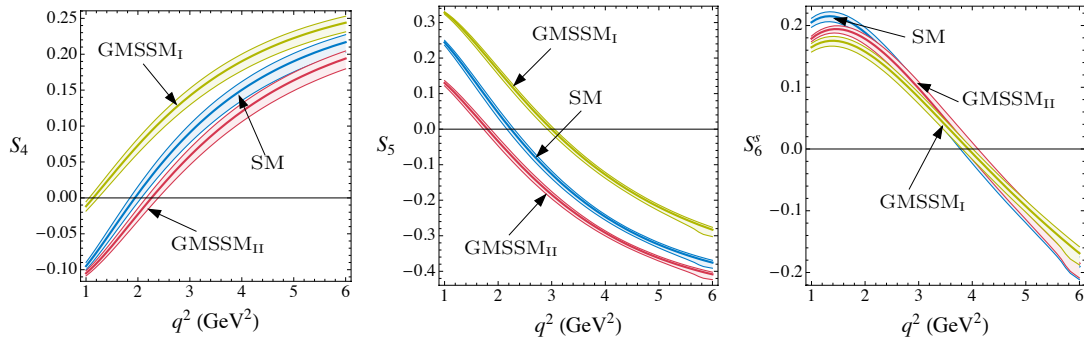


**Figure 4.13:** The observables  $S_4$ ,  $S_5$  and  $S_6^s$  in the SM (blue band) and two GMSSM scenarios with large complex contributions to  $C_7'$  as described in the text.

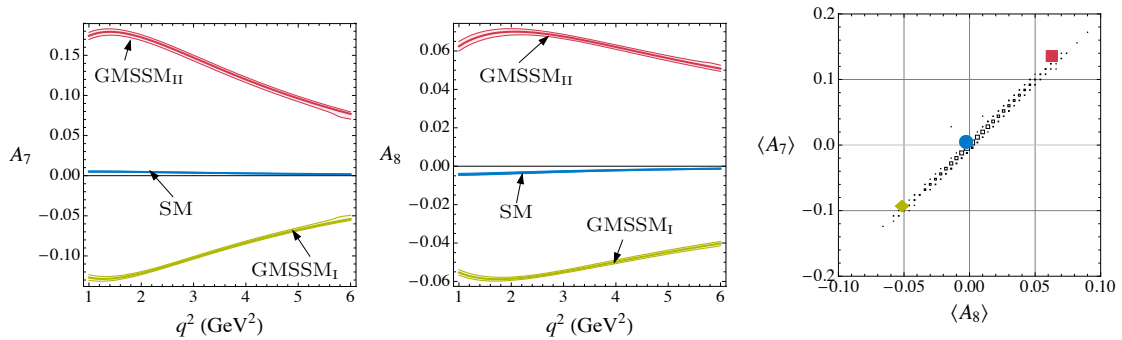


**Figure 4.14:** Left and center plot: CP asymmetries  $A_7$  and  $A_8$  in the SM (blue band) and two general MSSM scenarios with large complex contributions to  $C_7'$ . Right plot: Correlation between the integrated asymmetries  $\langle A_7 \rangle$  and  $\langle A_8 \rangle$  in the framework of a general MSSM with large complex  $C_7'$ . The blue circle corresponds to the central SM value, while the green diamond represents scenario GMSSM<sub>I</sub> and the red square scenario GMSSM<sub>II</sub>.

#### 4. $B \rightarrow K^* \mu^+ \mu^-$

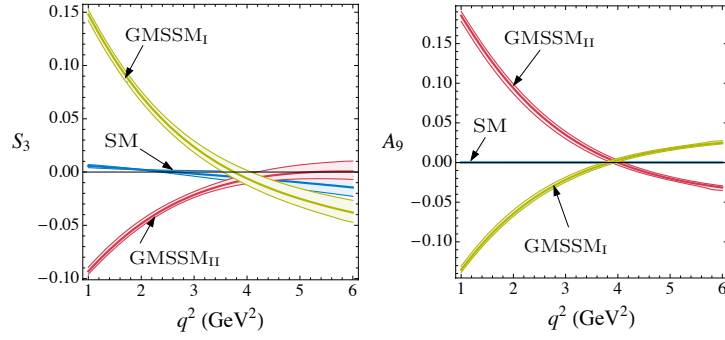


**Figure 4.15:** The observables  $S_3$  and  $A_9$  in the SM (blue band) and the two GMSSM scenarios  $\text{GMSSM}_{\text{I,II}}$  with large complex contributions to  $C_7'$  as described in the text.

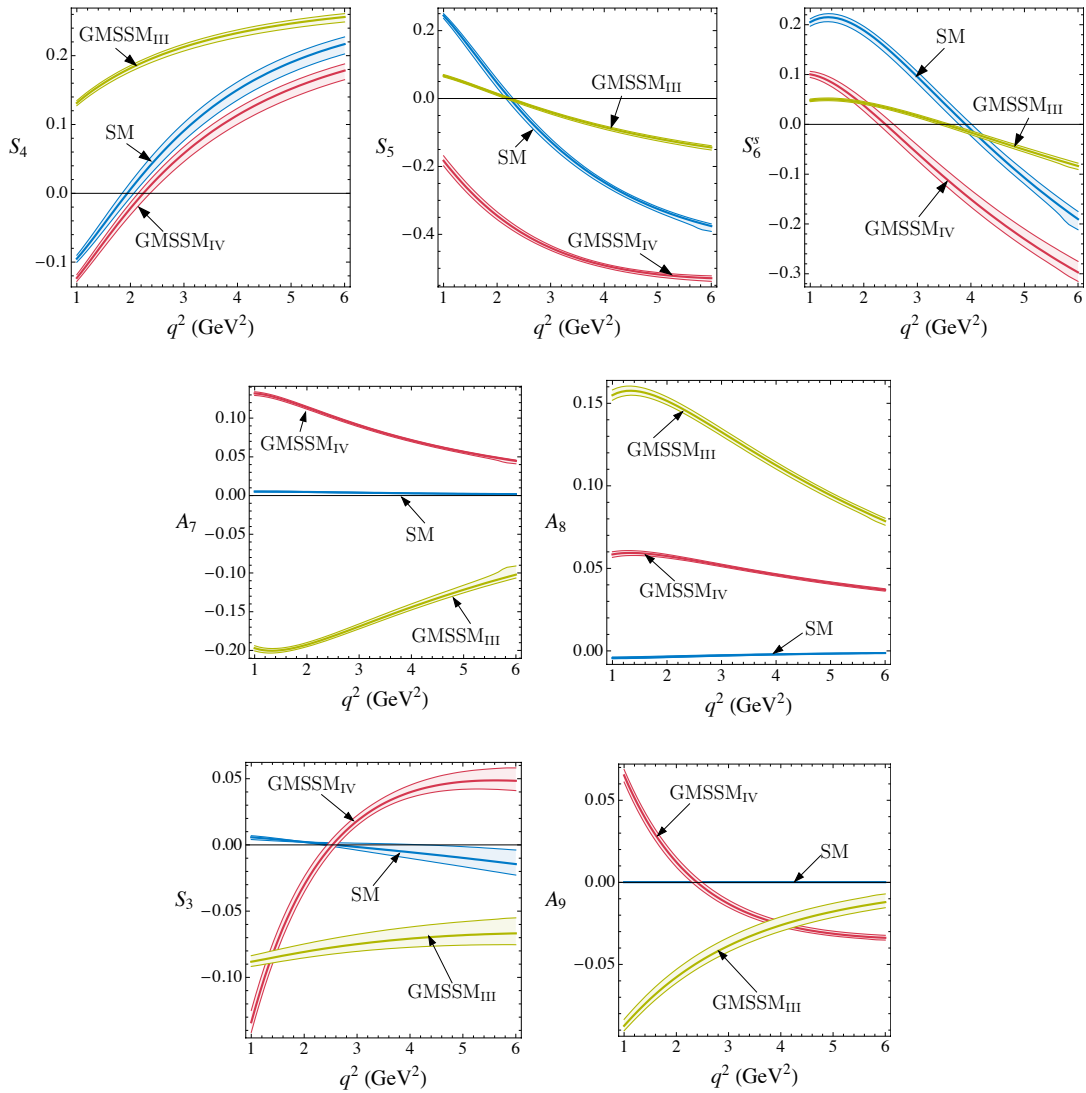


**Figure 4.16:** Several observables in the SM (blue band) and two selected GMSSM scenarios that show large non-standard behaviour. See text for details.



# Chapter 5

## Series Expansion

### 5.1 Introduction

As mentioned in section 2, there are many parametrizations of form factors discussed in the literature. The aim of this chapter is to use a particular parametrization, the so-called Series Expansion (SE), to describe the transition form factors on the basis of recent lattice and LCSR results, including a detailed analysis of systematic errors. The term SE has its origin in the form of the parametrization as an expansion in  $z(q^2)$ , a small,  $q^2$ -dependent quantity, to be defined below. We apply this expansion to form factors entering  $B \rightarrow V\gamma$ ,  $B \rightarrow L\ell^+\ell^-$ ,  $B \rightarrow L\nu\bar{\nu}$  decays, where  $L = P, V$  is a light vector or pseudoscalar meson, respectively. In particular, we give numerical results of fits of the parametrization to LCSR and lattice QCD data for  $B \rightarrow K$  and  $B \rightarrow \rho$  transitions. As a third source of theoretical input of the fits we use dispersive bounds, which arise from relations of the non-perturbative transition amplitudes  $B \rightarrow L$  and the perturbative pair-production amplitude of  $BL$ . For the discussion of dispersive bounds for tensor form factors, we will include the result of a precise calculation of the tensor current two-point correlator at next-to-leading order in the QCD coupling constant, including the leading non-perturbative corrections from quark and gluon condensates.

### 5.2 Dispersive Bounds

The form factors describing the transition amplitudes  $B \rightarrow L$  in the decay region  $0 < q^2 < t_- = (m_B - m_L)^2$  are related by crossing symmetry to the pair-production amplitude in the region  $q^2 > t_+ = (m_B + m_L)^2$ . Indeed, they can be seen as the same analytically connected functions. This fact can be exploited to obtain a bound on pa-

parameters describing the form factors. A detailed derivation of this bound can be found in refs. [26,27]. In order to incorporate form factors of vector and tensor currents we extend the discussion and the notation introduced in section 2.3. In particular the generalized correlator of two flavor-changing currents reads,

$$\Pi_{\mu\nu}^X(q^2) = i \int d^4x e^{iq \cdot x} \langle 0 | T j_\mu^X(x) j_\nu^{\dagger X}(0) | 0 \rangle . \quad (5.1)$$

Here the relevant currents  $j_\mu^X$  are defined as<sup>1</sup>

$$\begin{aligned} j_\mu^V &= \bar{q} \gamma_\mu b, & j_\mu^{V-A} &= \bar{q} \gamma_\mu (1 - \gamma^5) b, \\ j_\mu^T &= \bar{q} \sigma_{\mu\alpha} q^\alpha b, & j_\mu^{T+A_T} &= \bar{q} \sigma_{\mu\alpha} q^\alpha (1 + \gamma^5) b. \end{aligned} \quad (5.2)$$

Furthermore, we introduce longitudinal and transverse helicity projectors,

$$P_L^{\mu\nu}(q^2) = \frac{q^\mu q^\nu}{q^2}, \quad P_T^{\mu\nu}(q^2) = \frac{1}{3} \left( \frac{q^\mu q^\nu}{q^2} - g^{\mu\nu} \right), \quad (5.3)$$

which allow us to rewrite the correlation functions in terms of Lorentz scalars,

$$\Pi_I^X(q^2) \equiv P_I^{\mu\nu}(q^2) \Pi_{\mu\nu}^X(q^2), \quad (I = L, T). \quad (5.4)$$

### 5.2.1 Unitary representation of the correlator

Unitarity allows to express  $\text{Im} \Pi_I^X(q^2)$  as the positive definite sum over all hadronic states  $\Gamma$  with allowed quantum numbers:

$$\text{Im} \Pi_I^X(q^2) = \frac{1}{2} \sum_{\Gamma} \int d\rho_{\Gamma} (2\pi)^4 \delta^4(q - p_{\Gamma}) P_I^{\mu\nu} \langle 0 | j_\mu^X | \Gamma \rangle \langle \Gamma | j_\nu^{\dagger X} | 0 \rangle, \quad (5.5)$$

where  $p_{\Gamma}$  is the total momentum of the final state, and  $d\rho_{\Gamma}$  contains the appropriate phase-space weighting. For a particular choice of intermediate state,  $\Gamma = BL$ , we define

$$\text{Im} \Pi_{I,BL}^X(q^2) = \eta \int d\rho_{BL} P_I^{\mu\nu} \langle 0 | j_\mu^X | BL \rangle \langle BL | j_\nu^{\dagger X} | 0 \rangle, \quad (5.6)$$

---

<sup>1</sup>In phenomenological applications, we are only interested in the currents  $j_\mu^{T+A_T}$ . The connection to correlators with genuine tensor currents  $j_{\mu\nu} = \bar{q} \sigma_{\mu\nu} q$  is given in appendix B.4.

## 5. Series Expansion

---

where  $\eta$  is an isospin-degeneracy factor for a given channel, and we relegate the contribution from phase space to the function

$$d\rho_{BL} = \frac{1}{4\pi^2} \int \frac{d^3 p_B}{2E_B} \frac{d^3 p_L}{2E_L} \delta^4(q - p_B - p_L). \quad (5.7)$$

Clearly, this results in the inequality

$$\text{Im}\Pi_{I,BL}^X(t) \leq \text{Im}\Pi_I^X(t). \quad (5.8)$$

Crossing symmetry allows to relate the matrix elements  $\langle 0 | j^X | BL \rangle$  to  $\langle B | j^X | L \rangle$ . The latter can be rewritten in terms of form factors, as defined in chapter 2.

As mentioned earlier, a further remarkable feature of the helicity-based form factors is the diagonal form of the production amplitudes:

$$\begin{aligned} P_T^{\mu\nu} \langle P | j_\mu^V | B \rangle \langle B | j_\nu^{\dagger V} | P \rangle &= \frac{\lambda}{3q^2} |\mathcal{A}_{V,0}|^2, \\ P_L^{\mu\nu} \langle P | j_\mu^V | B \rangle \langle B | j_\nu^{\dagger V} | P \rangle &= \frac{\lambda}{q^2} |\mathcal{A}_{V,t}|^2, \\ P_T^{\mu\nu} \langle P | j_\mu^T | B \rangle \langle B | j_\nu^{\dagger T} | P \rangle &= \frac{\lambda}{3} |\mathcal{A}_{T,0}|^2, \end{aligned} \quad (5.9)$$

for  $B$  decays into pseudoscalars, and

$$\begin{aligned} P_T^{\mu\nu} \langle V | j_\mu^{V-A} | B \rangle \langle B | j_\nu^{\dagger, V-A} | V \rangle &= \frac{\lambda}{3q^2} \sum_{i=0}^2 |\mathcal{B}_{V,i}|^2, \\ P_L^{\mu\nu} \langle V | j_\mu^{V-A} | B \rangle \langle B | j_\nu^{\dagger, V-A} | V \rangle &= \frac{\lambda}{q^2} |\mathcal{B}_{V,t}|^2, \\ P_T^{\mu\nu} \langle V | j_\mu^{T+A_T} | B \rangle \langle B | j_\nu^{\dagger, T+A_T} | V \rangle &= \frac{\lambda}{3} \sum_{i=0}^2 |\mathcal{B}_{T,i}|^2. \end{aligned} \quad (5.10)$$

for decays into vector mesons. Specifically, in this context *diagonal* means that the right-hand sides of the latter equations are sums of absolute values squared and that no products of two different form factors are present.  $\text{Im}\Pi_{I,BL}^X$  can be expressed in compact form,

$$\text{Im}\Pi_{I,BL}^X = \eta \int d\rho_{BL} \frac{\lambda}{3q^2} |A_I^X|^2 = \frac{\eta}{48\pi} \frac{\lambda^{3/2}}{(q^2)^2} |A_I^X|^2, \quad (5.11)$$

where the  $|A_I^X|^2$  can be read off from (5.9, 5.10),

$$|A_T^V|^2 = |\mathcal{A}_{V,0}|^2, \quad |A_L^V|^2 = 3|\mathcal{A}_{V,t}|^2, \quad |A_T^T|^2 = q^2 |\mathcal{A}_{T,0}|^2, \quad (5.12)$$

for decays into pseudoscalars, and

$$|A_T^{V-A}|^2 = \sum_{i=0}^2 |\mathcal{B}_{V,i}|^2, \quad |A_L^{V-A}|^2 = 3|\mathcal{B}_{V,t}|^2, \quad |A_T^{T+A_T}|^2 = q^2 \sum_{i=0}^2 |\mathcal{B}_{T,i}|^2, \quad (5.13)$$

for decays into vector mesons.

## 5.2.2 Operator Product Expansion for the Correlator

Alternatively, we can examine the correlator (5.1), using an operator product expansion for the time-ordered product of currents in the limit  $q^2 = 0 \ll t_+$ . The standard expansion takes the form [14, 117, 118]

$$i \int dx e^{iq \cdot x} P_I^{\mu\nu} \text{T} \{j_\mu^X(x) j_\nu^{\dagger X}(0)\} = \sum_{k=1}^{\infty} C_{I,k}^X(q) \mathcal{O}_k, \quad (5.14)$$

where  $C_{I,n}^X(q)$  are Wilson coefficients for a given current  $X$  and projector  $I$ , and  $\mathcal{O}_n$  are local gauge-invariant operators, consisting of quark and gluon fields. Besides the identity operator, whose Wilson coefficient contains the purely perturbative contribution to the correlator, we will specifically consider the first few operators related to the non-perturbative contribution from the quark condensate  $\langle m_q \bar{q}q \rangle$ , the gluon condensate  $\langle \frac{\alpha_s}{\pi} G^2 \rangle$  and the mixed condensate  $\langle g_s \bar{q} (\sigma \cdot G) q \rangle$ . We will elaborate on our calculation of the Wilson coefficients,  $C_{I,k}^X(q^2)$ , later. Specifically, we must calculate the Wilson coefficients entering the functions  $\chi_I^X(n)$  in eq. (2.38).

## 5.2.3 Dispersive Bounds

Combining, the representation of  $\text{Im} \Pi_{I,BL}^X(q^2)$  in terms of form factors (eq. (5.5, 5.9, 5.10)), the representation of  $\Pi_{I,BL}^X(q^2)$  through  $\text{Im} \Pi_{I,BL}^X(q^2)$  (eq. (2.38)) and the inequality (5.8), we find:

$$\frac{1}{\pi} \int_0^\infty dt \frac{\text{Im} \Pi_{I,BL}^X(t)}{(t - q^2)^{n+1}} \Big|_{q^2=0} = \frac{1}{\pi} \int_{t_+}^\infty dt \frac{\eta \lambda^{3/2}(t)}{48\pi t^{n+3}} |A_I^X(t)|^2 \leq \chi_I^X(n), \quad (5.15)$$

where  $\chi_I^X \equiv \chi_{I,\text{OPE}}^X$  is calculated from (5.14).

### 5.3 Series Expansion Parametrization

The primary motivation for the SE is to make direct use of the explicit dispersive bound (5.15). The starting point is to extend the form factors defined in the physical range to analytic functions throughout the complex  $t = q^2$  plane, except along the branch cut at the threshold for production of real  $BP/BV$  pairs at  $q^2 \geq t_+ = (m_B + m_L)^2$ .

Then, using

$$z(t) \equiv z(t, t_0) = \frac{\sqrt{t_+ - t} - \sqrt{t_+ - t_0}}{\sqrt{t_+ - t} + \sqrt{t_+ - t_0}}, \quad (5.16)$$

the pair-production region  $t \geq t_+$  is mapped onto the unit circle  $|z(t)| = 1$ . Note, that  $0 \leq t_0 < t_-$  is a free parameter which can be optimized to reduce the maximum value of  $|z(t)|$  in the physical form factors range,

$$t_0|_{\text{opt.}} = t_+ \left( 1 - \sqrt{1 - \frac{t_-}{t_+}} \right). \quad (5.17)$$

The inequality (5.15) takes the form

$$\frac{1}{2\pi i} \oint \frac{dz}{z} |\phi_I^X A_I^X|^2(z) \leq 1 \quad \Leftrightarrow \quad \frac{1}{\pi} \int_{t_+}^{\infty} \frac{dt}{t - t_0} \sqrt{\frac{t_+ - t_0}{t - t_+}} |\phi_I^X A_I^X|^2(t) \leq 1, \quad (5.18)$$

where the function  $|\phi_I^X(t)|^2$  can be obtained by comparing (5.18) and (5.15), and using  $\lambda(t) = (t_+ - t)(t_- - t)$ ,

$$|\phi_I^X(t)|^2 = \frac{\eta}{48\pi \chi_I^X(n)} \frac{(t - t_+)^2}{(t_+ - t_0)^{1/2}} \frac{(t - t_-)^{3/2}}{t^{n+2}} \frac{t - t_0}{t}. \quad (5.19)$$

The isospin-degeneracy factor  $\eta$  takes the values 3/2 and 2 for  $B \rightarrow \rho$  and  $B \rightarrow K$  respectively. We may now generically write the helicity-based form factors  $A_I^X(t)$  as

$$A_I^X(t) = \frac{(\sqrt{-z(t, 0)})^m (\sqrt{z(t, t_-)})^l}{B(t) \phi_I^X(t)} \sum_{k=0}^{\infty} \alpha_k z^k \quad (5.20)$$

with real coefficients  $\alpha_k$ , and a Blaschke factor  $B(t) = \prod_i z(t, m_{R_i}^2)$ , representing poles due to sub-threshold resonances of masses  $m_{R_i}$ , and satisfying  $|B(t)| = 1$  in the pair-production region. The additional factors  $(\sqrt{-z(t, 0)})^m$  and  $(\sqrt{z(t, t_-)})^l$  have been added to take into account the unconventional normalization of our form factor functions through factors of  $\sqrt{q^2}$  and  $\sqrt{\lambda}$  (e.g.  $m = 1$  for  $\mathcal{A}_{T,0}$ , and  $l = -1$  for  $\mathcal{A}_{V,t}$ , cf.

above).<sup>2</sup> The function  $\phi_I^X(t)$  has to be constructed in such a way that its absolute value satisfies eq. (5.19), while (5.20) retains the analytical properties of the form factors. This can easily be achieved by replacing potential poles and cuts in  $\sqrt{|\phi_I^X(t)|^2}$ , by making replacements of the form

$$\frac{1}{t-X} \rightarrow \frac{-z(t, X)}{t-X}, \quad (5.21)$$

which is allowed as  $|z(t, X)| = 1$  in the pair-production region. This results in (see also [119])

$$\phi_I^X(t) = \sqrt{\frac{\eta}{48\pi\chi_I^X(n)}} \frac{(t-t_+)}{(t_+-t_0)^{1/4}} \left(\frac{z(t,0)}{-t}\right)^{(3+n)/2} \left(\frac{z(t,t_0)}{t_0-t}\right)^{-1/2} \left(\frac{z(t,t_-)}{t_- - t}\right)^{-3/4}. \quad (5.22)$$

Inserting the parametrization (5.20) into (5.18), and using  $|z(t, t_0)| = |z(t, m_R^2)| = |z(t, 0)| = 1$ , the integration  $dz/z = d\varphi$  along the unit circle is trivial, yielding the desired bound on the coefficients  $\alpha_k$ ,

$$\sum_{k=0}^{\infty} \alpha_k^2 < 1. \quad (5.23)$$

For decays into vector mesons, using an analogous parametrization as (5.20) for each individual form factor contribution in (5.13), one obtains a bound on the sum of the corresponding coefficients.

For those channels where lattice data are not available, it is essential to employ a form factor parametrization that takes into account the characteristic features of the form factor shape as determined from the analyticity and unitarity consideration above. For every form factor considered, we will therefore define a parametrization based on the general SE given in eq. (5.20),

$$\mathcal{A}_{V,0}(t) = \frac{1}{B(t)\phi_T^V(t)} \sum_{k=0}^{K-1} \alpha_k^{(V,0)} z^k,$$

$$\mathcal{A}_{V,t}(t) = \frac{1}{B(t)\sqrt{z(t,t_-)}\phi_L^V(t)} \sum_{k=0}^{K-1} \alpha_k^{(V,t)} z^k,$$

---

<sup>2</sup>These factors could also be considered as part of the Blaschke factor. Note that under a change of normalization convention for the form factors, both the so-constructed Blaschke factor as well as the function  $\phi(t)$  have to be modified, while the coefficients  $\alpha_k$  of the SE remain the same.

## 5. Series Expansion

---

$$\mathcal{A}_{T,0}(t) = \frac{\sqrt{-z(t,0)}}{B(t) \phi_T^T(t)} \sum_{k=0}^{K-1} \alpha_k^{(T,0)} z^k, \quad (5.24)$$

and

$$\begin{aligned} \mathcal{B}_{V,0}(t) &= \frac{1}{B(t) \sqrt{z(t,t_-)} \phi_T^{V-A}(t)} \sum_{k=0}^{K-1} \beta_k^{(V,0)} z^k, \\ \mathcal{B}_{V,1}(t) &= \frac{\sqrt{-z(t,0)}}{B(t) \phi_T^{V-A}(t)} \sum_{k=0}^{K-1} \beta_k^{(V,1)} z^k, \\ \mathcal{B}_{V,2}(t) &= \frac{\sqrt{-z(t,0)}}{B(t) \sqrt{z(t,t_-)} \phi_T^{V-A}(t)} \sum_{k=0}^{K-1} \beta_k^{(V,2)} z^k, \\ \mathcal{B}_{V,t}(t) &= \frac{1}{B(t) \phi_L^{V-A}(t)} \sum_{k=0}^{K-1} \beta_k^{(V,t)} z^k, \\ \mathcal{B}_{T,0}(t) &= \frac{\sqrt{-z(t,0)}}{B(t) \sqrt{z(t,t_-)} \phi_T^{T+A_T}(t)} \sum_{k=0}^{K-1} \beta_k^{(T,0)} z^k, \\ \mathcal{B}_{T,1}(t) &= \frac{1}{B(t) \phi_T^{T+A_T}(t)} \sum_{k=0}^{K-1} \beta_k^{(T,1)} z^k, \\ \mathcal{B}_{T,2}(t) &= \frac{1}{B(t) \sqrt{z(t,t_-)} \phi_T^{T+A_T}(t)} \sum_{k=0}^{K-1} \beta_k^{(T,2)} z^k. \end{aligned} \quad (5.25)$$

Here we have used our form factors convention defined in eqs. (2.5, 2.8, 2.10, 2.12) and explicitly quoted the pre-factors necessary to obtain the correct analytical behavior of our form factors. In our fits below, we will find that in general the SE can be truncated after the first two terms, i.e. the parameter  $K$  can be set to 2.

For simplicity, we will not explicitly implement the theoretical relations (2.14, 2.15), that some of the form factors fulfill at  $q^2 = 0$ , into the fit, because they are automatically satisfied by the rather precise input from LCSR at this point. However, the helicity-based form factor definition further implies a relation between the form factors  $\mathcal{B}_{V,0}$  and  $\mathcal{B}_{V,2}$ , and similarly between  $\mathcal{B}_{T,0}$  and  $\mathcal{B}_{T,2}$  (see (2.16) in the appendix), which we will implement as an additional constraint on the corresponding coefficients in the SE.

For the SE parametrization, the unitarity constraints take the form (see. 5.23)

$$\sum_{k=0}^{K-1} (\alpha_k)^2 \leq 1 \quad \text{for } \mathcal{A}_{V,0} \text{ and } \mathcal{A}_{T,0}, \quad 3 \sum_{k=0}^{K-1} (\alpha_k)^2 \leq 1 \quad \text{for } \mathcal{A}_{V,t}, \quad (5.26)$$

and

$$\begin{aligned} 3 \sum_{k=0}^{K-1} (\beta_k^{(V,t)})^2 &\leq 1 \quad \text{for } \mathcal{B}_{V,t}, \\ \sum_{k=0}^{K-1} \left\{ (\beta_k^{(V,0)})^2 + (\beta_k^{(V,1)})^2 + (\beta_k^{(V,2)})^2 \right\} &\leq 1 \quad \text{for } \mathcal{B}_{V,0}, \mathcal{B}_{V,1}, \text{ and } \mathcal{B}_{V,2}, \\ \sum_{k=0}^{K-1} \left\{ (\beta_k^{(T,0)})^2 + (\beta_k^{(T,1)})^2 + (\beta_k^{(T,2)})^2 \right\} &\leq 1 \quad \text{for } \mathcal{B}_{T,0}, \mathcal{B}_{T,1}, \text{ and } \mathcal{B}_{T,2}. \end{aligned} \quad (5.27)$$

## 5.4 Simplified Series Expansion

Another form of the SE method can also be considered. Instead of the Blaschke factor  $B(t)$ , one can use a simple pole  $P(q^2)$  to account for low-lying resonances. This idea was proposed in ref. [24], yielding

$$f(t) = \frac{1}{P(t)} \sum_k \tilde{\alpha}_k z^k(t, t_0). \quad (5.28)$$

It was found that the dispersive bounds can still be imposed on the coefficients  $\tilde{\alpha}_k$  of the Simplified Series Expansion (SSE). We will discuss this and other issues concerning the validity of the simplifications in the following section.

From the above parametrizations, the SSE is obtained by the replacements

$$\phi_I^X(t) \rightarrow 1, \quad B(t) \rightarrow P(t), \quad \sqrt{-z(t,0)} \rightarrow \sqrt{q^2/m_B}, \quad \sqrt{z(t,t_-)} \rightarrow \sqrt{\lambda/m_B^2}, \quad (5.29)$$

with new coefficients  $\tilde{\alpha}_k$  and  $\tilde{\beta}_k$ .

For the SSE parametrization, imposing the unitarity bound is more complicated, as shown in ref. [24]. We repeat the derivation of this bound in order to define notation used later. One first compares the SE and SSE parametrizations:

$$\sum_{k=0}^{K-1} \alpha_k z^k = \Lambda(z) \sum_{k=0}^{K-1} \tilde{\alpha}_k z^k \quad (5.30)$$

## 5. Series Expansion

---

One can simply obtain  $\Lambda(z)$  by combining the prefactors from the SE expansion with the prefactors from the SSE expansion, and expressing the result as a function of  $z(t, t_0)$ . Since  $z$  is a small parameter, we can expand  $\Lambda(z)$  in powers of  $z$ :

$$\Lambda(z) = \sum_k \zeta_k z^k. \quad (5.31)$$

We can therefore obtain a relation between the coefficients  $\alpha_k$  and  $\tilde{\alpha}_k$ ,

$$\alpha_i = \sum_{k=0}^{\min[K-1, i]} \zeta_{i-k} \tilde{\alpha}_k, \quad 0 \leq i \leq K-1, \quad (5.32)$$

which results in bounds of the type

$$\sum_{j,k=0}^{K-1} C_{jk} \tilde{\alpha}_j \tilde{\alpha}_k \leq 1, \quad (5.33)$$

where

$$C_{jk} = \sum_{i=0}^{K-1-\max[j,k]} \zeta_i \zeta_{i+|j-k|} \quad (5.34)$$

is a positive definite matrix.

### 5.5 Fitting prescription

We perform a fit to the LCSR data, as well as, where possible, a combined fit to the LCSR and lattice data, by minimizing a  $\chi^2$  function defined by

$$\chi^2(\vec{\theta}) = \left( F_i - F(t_i, \vec{\theta}) \right) [V^{-1}]_{ij} \left( F_j - F(t_j, \vec{\theta}) \right), \quad (5.35)$$

where  $\vec{\theta}$  contains the parameters of a given form factor parametrization,  $F_i$  are the form factor values from LCSR/lattice at given points  $t_i$ , and  $V_{ij}$  are elements of the covariance matrix as defined below.

As explained above, we are going to investigate parametrizations based on two variants of the SE, where the parameters will be subject to additional constraints derived from dispersive bounds on the form factors.

- In the conventional SE, we use eq. (5.20), and truncate the series after the first

two terms, such that

$$\vec{\theta} = \{\alpha_0, \alpha_1\}, \quad \sum \alpha_i^2 \stackrel{!}{<} 1.$$

- The simplified series expansion (SSE) uses (5.28), with

$$\vec{\theta} = \{\tilde{\alpha}_0, \tilde{\alpha}_1\}, \quad \sum_{i,j=0}^1 C_{ij} \tilde{\alpha}_i \tilde{\alpha}_j \stackrel{!}{<} 1,$$

where the matrix  $C_{ij}$  is defined in (5.34).

In constructing the covariance matrix, when we do a combined fit to LCSR and lattice data, we assume the matrix to be block diagonal with independent blocks for LCSR and lattice, equivalent to  $\chi^2 = \chi_{\text{LCSR}}^2 + \chi_{\text{Lat}}^2$ , where

$$\chi_{\text{LCSR}}^2(\vec{\theta}) = \left( F_i - F(t_i, \vec{\theta}) \right) [V_{\text{LCSR}}^{-1}]_{ij} \left( F_j - F(t_j, \vec{\theta}) \right), \quad (5.36)$$

and

$$\chi_{\text{Lat}}^2(\vec{\theta}) = \left( F_i - F(t_i, \vec{\theta}) \right) [V_{\text{Lat}}^{-1}]_{ij} \left( F_j - F(t_j, \vec{\theta}) \right). \quad (5.37)$$

We consider the statistical and systematic contributions to the lattice errors separately. For results that are not (yet) available in the literature, we received the data by private communication with the authors. In obtaining the covariance matrix, we make the following conservative assumptions:

- Statistical errors of lattice data are 50% correlated [120, 121].
- Systematic errors of lattice data are 100% correlated [120, 121].
- Errors of LCSR data at different values  $t_i$  are estimated to be 75% correlated.

This prescription leads to a covariance matrix  $V^{ij} = \text{cov}[t^i, t^j]$ , containing

$$V_{\text{LCSR}}^{ij} = \frac{1}{4} \kappa^i \kappa^j \delta_{ij} + \frac{3}{4} \kappa^i \kappa^j \quad \text{and} \quad (5.38)$$

$$V_{\text{Lat}}^{ij} = \frac{1}{2} \sigma^i \sigma^j \delta_{ij} + \frac{1}{2} \sigma^i \sigma^j + \varepsilon^i \varepsilon^j \quad (5.39)$$

where  $\sigma_i$  are the statistical errors,  $\varepsilon_i$  are the systematic errors for the lattice data, and  $\kappa_i$  are the errors for the LCSR predictions.

## 5. Series Expansion

---

Minimizing  $\chi^2(\vec{\theta})$  then yields the best fit parameters  $\vec{\theta}^*$  as well as the covariance matrix of the fit,  $U_{ij} = \text{cov}[\theta_i, \theta_j]$ ,

$$(U^{-1})_{ij} = \frac{1}{2} \frac{\partial^2 \chi^2(\vec{\theta})}{\partial \theta_i \partial \theta_j} \Bigg|_{\vec{\theta}=\vec{\theta}^*}, \quad (5.40)$$

from which we calculate the error associated to the fitted form factor function:

$$\Delta F(t, \vec{\theta}^*) = \frac{\partial F(t, \vec{\theta})}{\partial \theta_i} \Bigg|_{\vec{\theta}=\vec{\theta}^*} U_{ij} \frac{\partial F(t, \vec{\theta})}{\partial \theta_j} \Bigg|_{\vec{\theta}=\vec{\theta}^*}. \quad (5.41)$$

## 5.6 Results

Having established the fitting procedure, we consider form factors for the decays  $B \rightarrow \rho$  and  $B \rightarrow K$ . We concentrate on radiative and rare semi-leptonic decays, as previously the dispersive bounds had not been calculated for the tensor current, so could not be applied to these decays. In the following subsection, we present the results of fitting the specific form factors to both, the SE and SSE parametrizations, using LCSR and lattice data where appropriate.

**$B \rightarrow K$  form factors:** In figs. 5.1–5.4, we show the fit for the various  $B \rightarrow K$  form factors, which enter, for instance, the radiative  $B \rightarrow K \ell^+ \ell^-$  and  $B \rightarrow K \nu \bar{\nu}$  decays. We compare the result of the SE and SSE parametrizations using LCSR data, and investigate the changes when the lattice data is included. The numerical results for the best-fit parameters of the SE and SSE fit are found in corresponding tables 5.1–5.2. The covariance matrices for these fits can also be found in ref. [122]. Generally, both parametrizations are seen to fit the data well, and importantly, we find agreement with the lattice predictions for  $\mathcal{A}_{V,0}$  and  $\mathcal{A}_{V,t}$ , even when they are not included in the fit. We therefore consider our extrapolation of LCSR data for the tensor form factor  $\mathcal{A}_{T,0}$  to the high- $q^2$  region, where lattice data does not exist, as sufficiently reliable. The quality of the fits is astonishingly good, considering the  $\chi^2$  values for only two free parameters in the expansion. The differences between the SE and SSE are only marginal, which can be traced back to the usage of the optimized value for the auxiliary parameter  $t_0$  in (5.17). The dispersive bounds turn out to be far from being separated, and therefore they have only little impact on the form factor fit. This observation is in line with other studies of heavy-to-light form factors in the literature, see e.g. [21, 25, 123].

Another comment applies to the scalar form factors  $\mathcal{A}_{V,t}$ : As shown in table 2.1,

the combined heavy-quark/chiral-symmetry limit considered in [20] predicts a scalar  $B_s$  resonance *below* the  $BK$ -production threshold (such a state is also favored by a lattice computation in [124]). On the other hand, the PDG only finds resonances at masses near/above the production threshold. We have therefore chosen to compare two variants of the fit, with/without a scalar resonance.<sup>3</sup> As can be seen, the fit *with* a scalar resonance from [20] describes the combined lattice/LCSR data significantly better than the fit without a low-lying resonance (where in the latter case again the dispersive bounds constrain the form factor to lie systematically below the lattice data). However, within the present uncertainties of lattice and LCSR data, this could only be taken as a very indirect argument in favor of a scalar resonance in the anticipated mass region.

**Table 5.1:**  $B \rightarrow K$ : Fit of SE parametrization to LCSR or LCSR/lattice results, for  $\mathcal{A}_{V,0}$  ( $X = 1$ ),  $\mathcal{A}_{V,t}$  ( $X = 3$ ) and  $\mathcal{A}_{T,0}$  ( $X = 1$ ).

$A_X$	$m_R$	$\alpha_0$	$\alpha_1$	Fit to	$\chi_{\text{fit}}^2$	$X \sum_i \alpha_i^2$
$\mathcal{A}_{V,0}$	5.41	$-2.4 \times 10^{-2}$	$6.2 \times 10^{-2}$	LCSR and lattice	$5.07 \times 10^{-3}$	$4.43 \times 10^{-3}$
$\mathcal{A}_{V,t}$	-	$-6.8 \times 10^{-2}$	0.20	LCSR and lattice	0.200	0.129
$\mathcal{A}_{V,t}$	5.72	$-4.8 \times 10^{-2}$	0.11	LCSR and lattice	$1.54 \times 10^{-4}$	$4.34 \times 10^{-2}$
$\mathcal{A}_{V,0}$	5.41	$-2.8 \times 10^{-2}$	$6.0 \times 10^{-2}$	LCSR	$3.94 \times 10^{-3}$	$4.40 \times 10^{-3}$
$\mathcal{A}_{V,t}$	-	$-6.7 \times 10^{-2}$	0.18	LCSR	$1.44 \times 10^{-3}$	0.111
$\mathcal{A}_{V,t}$	5.72	$-2.5 \times 10^{-2}$	$7.2 \times 10^{-2}$	LCSR	0.329	$5.77 \times 10^{-3}$
$\mathcal{A}_{T,0}$	5.41	$-4.5 \times 10^{-2}$	$8.9 \times 10^{-2}$	LCSR	0.234	$2.99 \times 10^{-2}$

**$B \rightarrow \rho$  form factors:** Our form factor fits for  $B \rightarrow \rho$  transitions, relevant for the radiative  $B \rightarrow \rho\gamma$  and  $B \rightarrow \rho\ell^+\ell^-$  decays, are summarized in figs. 5.5–5.11 and tables 5.3 and 5.4, where we again compare the fit to SE and SSE parametrizations. As in the case of  $B \rightarrow K$  form factors, we generally observe similarly good results for SE and SSE fits, with the dispersive bounds again playing only a minor role in restricting the coefficients of the SE/SSE. The covariance matrices for the fits can again be found in appendix ??.

lattice results are restricted to the (axial-)vector form factors, and we again study how the fits change when the lattice data is included: In case of the form factor  $\mathcal{B}_{V,0}$ , the uncertainties on the lattice data are rather large, and the fit is in any case dominated by the LCSR points at low values of  $q^2$ . Still, we find that the best-fit curve also

<sup>3</sup>Notice that BZ [37] use an effective resonance mass above production threshold to parameterize the scalar form factors.

## 5. Series Expansion

**Table 5.2:**  $B \rightarrow K$ : Fit of SSE parametrization to LCSR or LCSR/lattice results, for  $\mathcal{A}_{V,0}$  ( $X = 1$ ),  $\mathcal{A}_{V,t}$  ( $X = 3$ ) and  $\mathcal{A}_{T,0}$  ( $X = 1$ ).

$\mathcal{A}_X$	$m_R$	$\tilde{\alpha}_0$	$\tilde{\alpha}_1$	Fit to	$\chi_{\text{fit}}^2$	$X \sum_{i,j} C_{i,j} \tilde{\alpha}_i \tilde{\alpha}_j$
$\mathcal{A}_{V,0}$	5.41	0.48	-1.0	LCSR and lattice	$5.15 \times 10^{-3}$	$4.04 \times 10^{-3}$
$\mathcal{A}_{V,t}$	-	0.54	-1.7	LCSR and lattice	0.904	0.142
$\mathcal{A}_{V,t}$	5.72	0.30	0.20	LCSR and lattice	$7.17 \times 10^{-5}$	$5.32 \times 10^{-2}$
$\mathcal{A}_{V,0}$	5.41	0.48	-1.1	LCSR	$8.15 \times 10^{-3}$	$3.06 \times 10^{-3}$
$\mathcal{A}_{V,t}$	-	0.52	-1.4	LCSR	$2.27 \times 10^{-3}$	$9.55 \times 10^{-2}$
$\mathcal{A}_{V,t}$	5.72	0.50	-1.4	LCSR	0.940	$6.51 \times 10^{-3}$
$\mathcal{A}_{T,0}$	5.41	0.28	0.35	LCSR	0.128	$3.15 \times 10^{-2}$

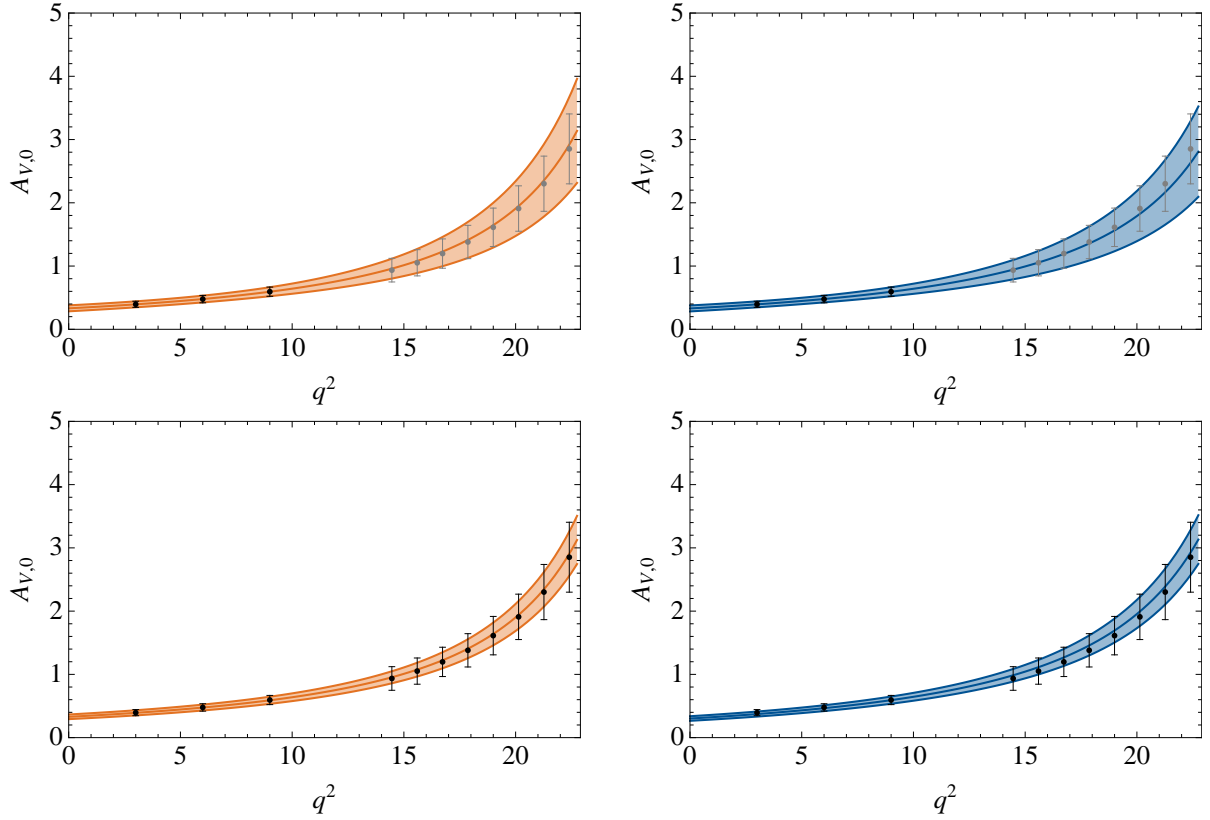


**Figure 5.1:**  $B \rightarrow K$ : Fit of SE (left) and SSE (right) parametrizations to LCSR (top) and to LCSR and lattice (bottom) for  $\mathcal{A}_{V,0}$ . The LCSR and lattice data are shown by black points with error bars in the appropriate  $q^2$  range.

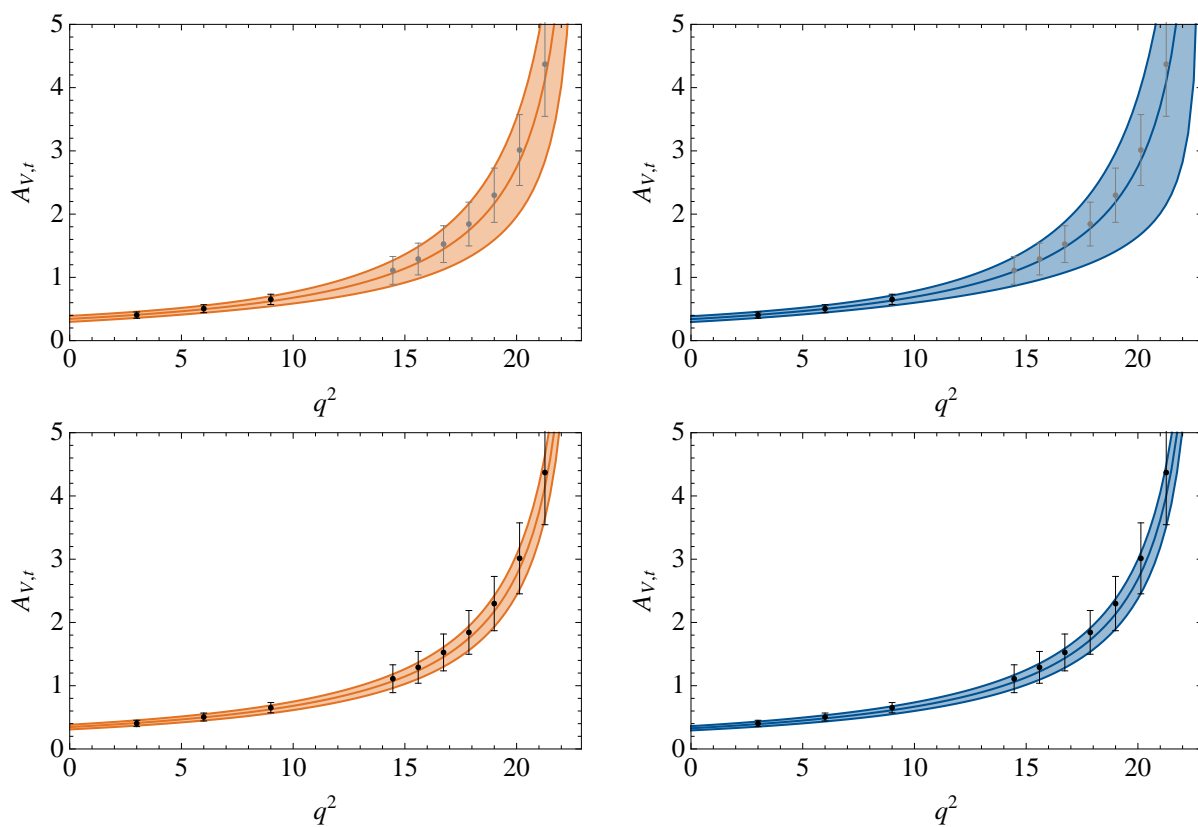


**Figure 5.2:**  $B \rightarrow K$ : Fit of SE (left) and SSE (right) parameterizations to LCSR (top) and to LCSR and lattice (bottom) for  $\mathcal{A}_{V,t}$ . The LCSR and lattice data are shown by black points with error bars in the appropriate  $q^2$  range.

## 5. Series Expansion

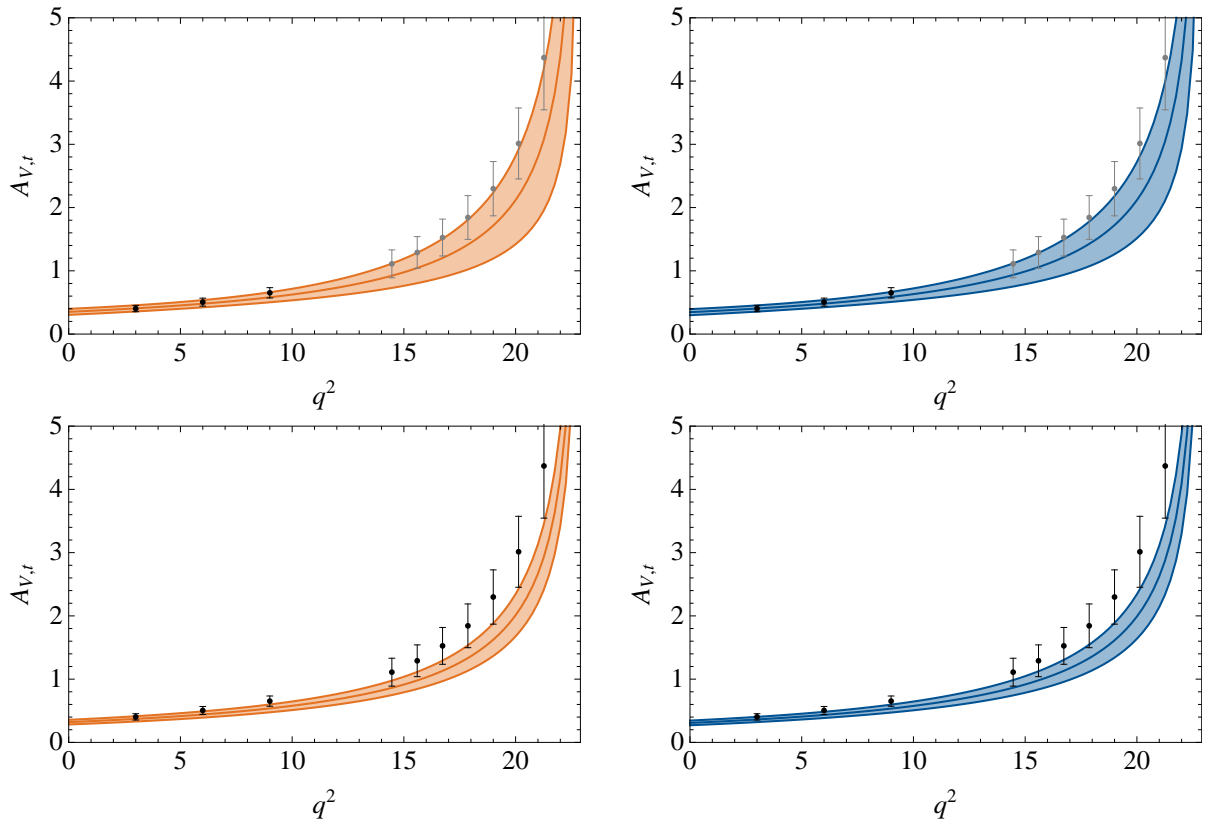


**Figure 5.3:**  $B \rightarrow K$ : The same as fig. 5.2 but without using the scalar  $B_s$  resonance in the fit ansatz.

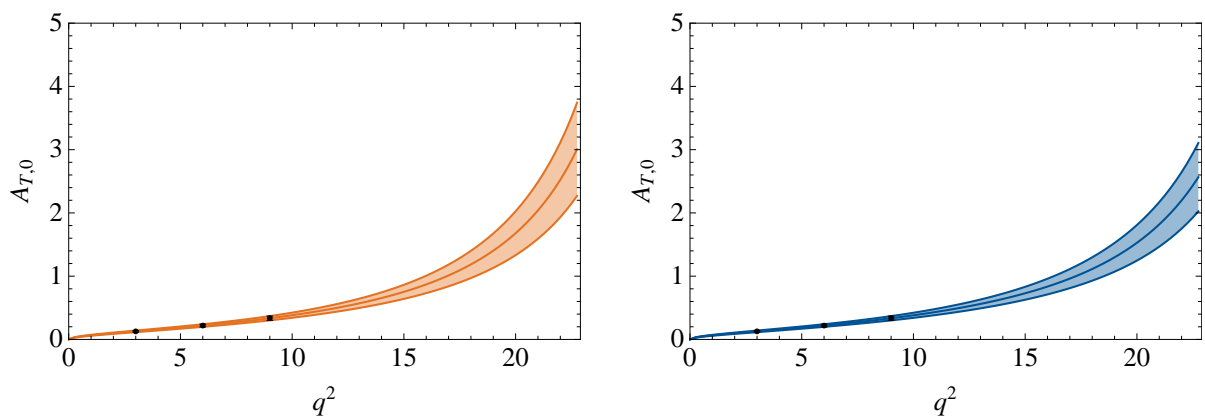


**Figure 5.4:**  $B \rightarrow K$ : Fit of SE (left) and SSE (right) parameterizations to LCSR for  $\mathcal{A}_{T,0}$ . The LCSR data is shown by black points with error bars.

well describes the central values of the lattice estimates. The situation is somewhat different for  $\mathcal{B}_{V,1}$ , where the central values of the lattice points do not quite agree with the extrapolation of the LCSR prediction. The fit is consistent within lattice uncertainties, but a rather large value of  $\chi^2$ , dominated by the deviations from the lattice points, is generated. On the other hand, for  $\mathcal{B}_{V,1}$  the lattice data are competitive with the LCSR input, and we can again observe that the extrapolation of the LCSR predictions describes the lattice points very well, while inclusion of the lattice data in this case leads to a very precise form factor description.

In the remaining cases, we again provide the extrapolations for the pseudoscalar and tensor form factors from LCSR input, where lattice data are not available. Here, it is to be mentioned that the uncertainties for the form factor  $\mathcal{B}_{T,0}$  are quite large, because we had to determine the LCSR input values from the difference of two form factors in (2.12). Of course, it would be desirable to directly calculate the form factor  $\mathcal{B}_{T,0}$  in the LCSR approach which should lead to significantly smaller uncertainties for the input data and the extrapolation to large values of  $q^2$ . A similar comment applies to the form factor  $\mathcal{B}_{V,0}$ .

**Table 5.3:**  $B \rightarrow \rho$ : Fit of SE parametrization to LCSR or LCSR/lattice results for  $\mathcal{B}_{V,0-2}$  ( $X = 1$ ),  $\mathcal{B}_{V,t}$  ( $X = 3$ ) and  $\mathcal{B}_{T,0-2}$  ( $X = 1$ ).

$B_X$	$m_R$	$\beta_0$	$\beta_1$	Fit to	$\chi_{\text{fit}}^2$	$X \sum_t \beta_i^2$
$\mathcal{B}_{V,0}$	5.72	$-8.0 \times 10^{-3}$	$2.5 \times 10^{-2}$	LCSR and lattice	32.1	$1.98 \times 10^{-2}$
$\mathcal{B}_{V,1}$	5.33	$-3.5 \times 10^{-2}$	0.11			
$\mathcal{B}_{V,2}$	5.72	$-2.5 \times 10^{-2}$	$7.8 \times 10^{-2}$			
$\mathcal{B}_{V,0}$	5.72	$-7.5 \times 10^{-3}$	$1.4 \times 10^{-2}$	LCSR	$9.56 \times 10^{-2}$	$1.28 \times 10^{-2}$
$\mathcal{B}_{V,1}$	5.33	$-3.7 \times 10^{-2}$	$8.9 \times 10^{-2}$			
$\mathcal{B}_{V,2}$	5.72	$-2.3 \times 10^{-2}$	$5.2 \times 10^{-2}$			
$\mathcal{B}_{V,t}$	5.28	$-3.2 \times 10^{-2}$	$8.9 \times 10^{-2}$	LCSR	$3.81 \times 10^{-3}$	$2.66 \times 10^{-2}$
$\mathcal{B}_{T,0}$	5.72	$-1.4 \times 10^{-2}$	$-8.3 \times 10^{-3}$	LCSR	$4.18 \times 10^{-2}$	$1.86 \times 10^{-3}$
$\mathcal{B}_{T,1}$	5.33	$-1.0 \times 10^{-2}$	$3.4 \times 10^{-2}$			
$\mathcal{B}_{T,2}$	5.72	$-6.3 \times 10^{-3}$	$1.7 \times 10^{-2}$			

## 5. Series Expansion

**Table 5.4:**  $B \rightarrow \rho$ : Fit of SSE parametrization to LCSR or LCSR/lattice results for  $\mathcal{B}_{V,0-2}$  ( $X = 1$ ),  $\mathcal{B}_{V,t}$  ( $X = 3$ ) and  $\mathcal{B}_{T,0-2}$  ( $X = 1$ ).

$B_X$	$m_R$	$\tilde{\beta}_0$	$\tilde{\beta}_1$	Fit to	$\chi^2_{\text{fit}}$	$X \sum_{i,j} C_{i,j} \tilde{\beta}_i \tilde{\beta}_j$
$\mathcal{B}_{V,0}$	5.72	0.26	0.14	LCSR and lattice	33.0	$1.85 \times 10^{-2}$
$\mathcal{B}_{V,1}$	5.33	0.51	-1.7			
$\mathcal{B}_{V,2}$	5.72	0.40	-0.15			
$\mathcal{B}_{V,0}$	5.72	0.26	0.50	LCSR	$4.34 \times 10^{-2}$	$1.10 \times 10^{-2}$
$\mathcal{B}_{V,1}$	5.33	0.54	-1.4			
$\mathcal{B}_{V,2}$	5.72	0.37	0.24			
$\mathcal{B}_{V,t}$	5.28	0.43	-1.3	LCSR	$8.49 \times 10^{-3}$	$2.16 \times 10^{-2}$
$\mathcal{B}_{T,0}$	5.72	0.35	0.94	LCSR	$3.57 \times 10^{-2}$	$1.79 \times 10^{-3}$
$\mathcal{B}_{T,1}$	5.33	0.52	-1.5			
$\mathcal{B}_{T,2}$	5.72	0.34	0.31			

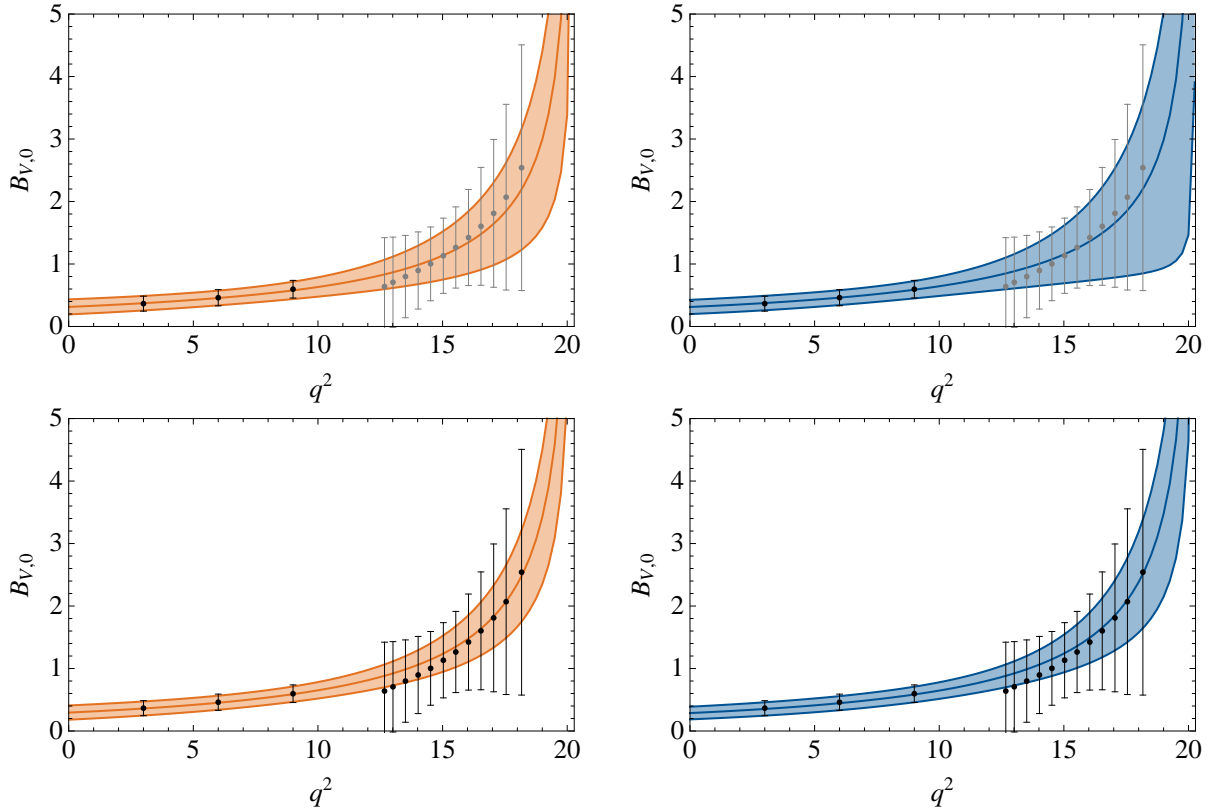


**Figure 5.5:**  $B \rightarrow \rho$ : Fit of SE (left) and SSE (right) parameterisations to LCSR (top) and to LCSR and lattice (bottom) for  $\mathcal{B}_{V,0}$ . The LCSR and lattice data are shown by black points with error bars in the appropriate  $q^2$  range.

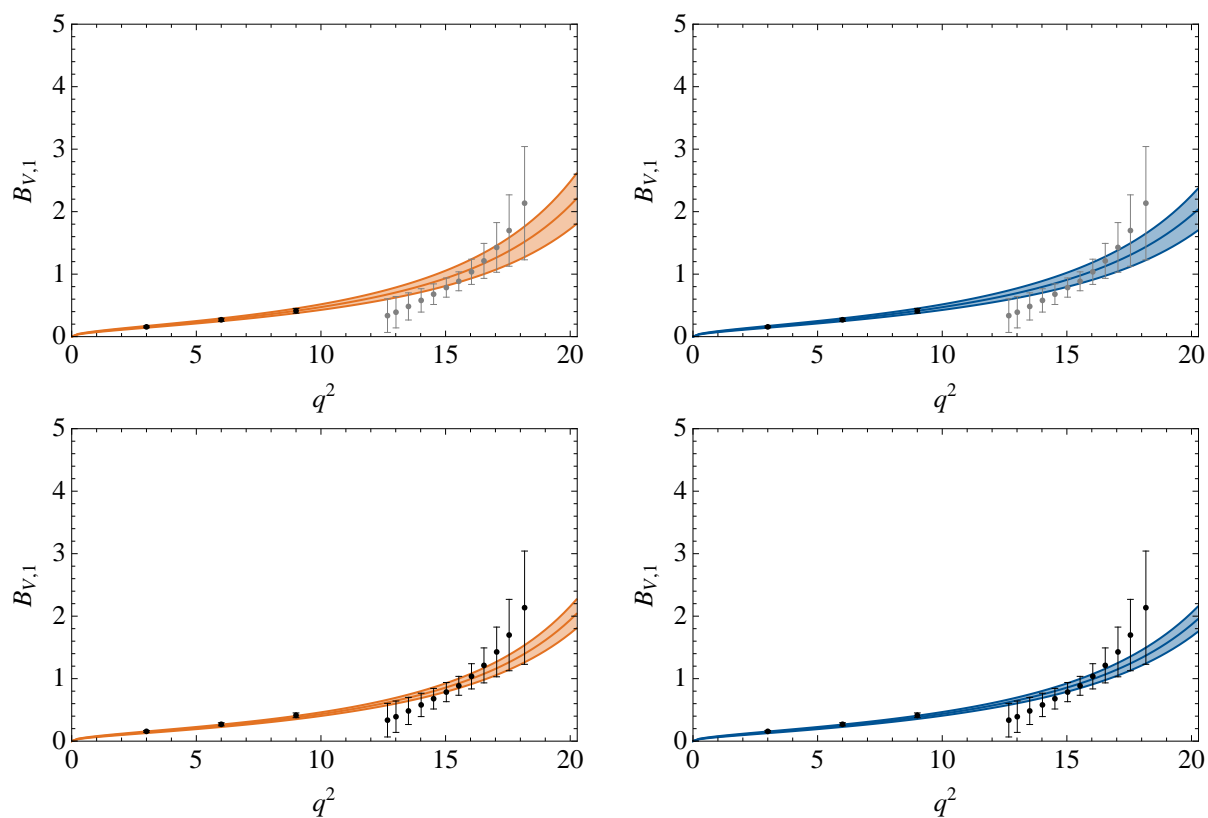


**Figure 5.6:**  $B \rightarrow \rho$ : Fit of SE (left) and SSE (right) parameterisations to LCSR (top) and to LCSR and lattice (bottom) for  $B_{V,1}$ . The LCSR and lattice data are shown by black points with error bars in the appropriate  $q^2$  range.

## 5. Series Expansion

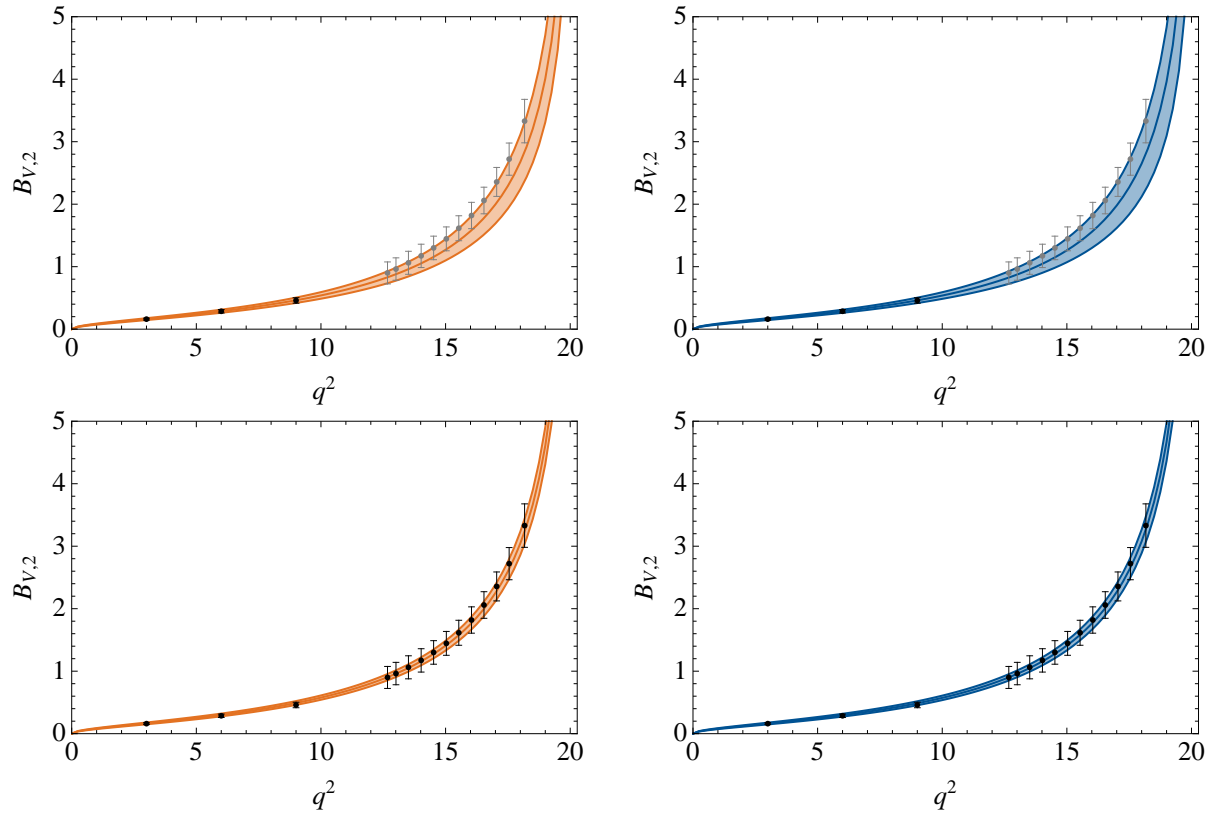


**Figure 5.7:**  $B \rightarrow \rho$ : Fit of SE (left) and SSE (right) parameterisations to LCSR (top) and to LCSR and lattice (bottom) for  $\mathcal{B}_{V,2}$ . The LCSR and lattice data are shown by black points with error bars in the appropriate  $q^2$  range.

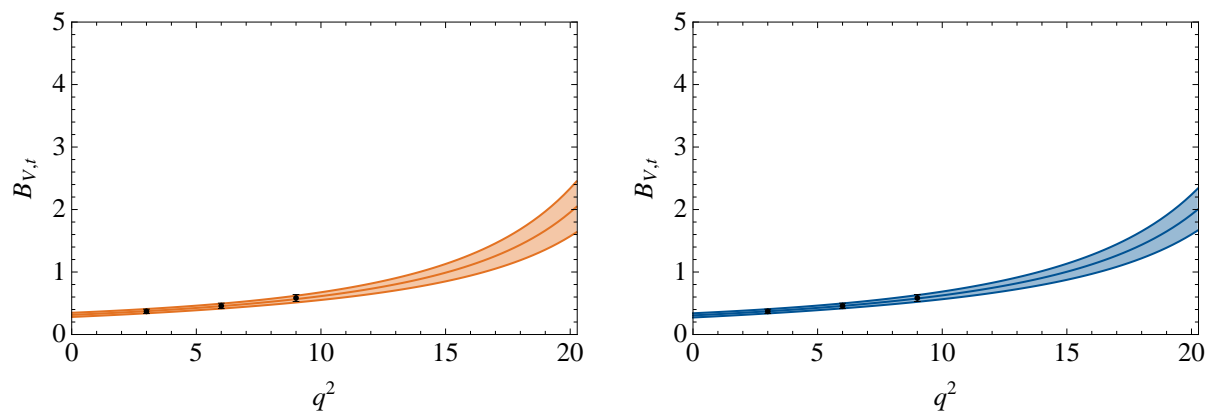


**Figure 5.8:**  $B \rightarrow \rho$ : Fit of SE (left) and SSE (right) parameterisations to LCSR for  $\mathcal{B}_{V,t}$ . The LCSR data is shown by black points with error bars.

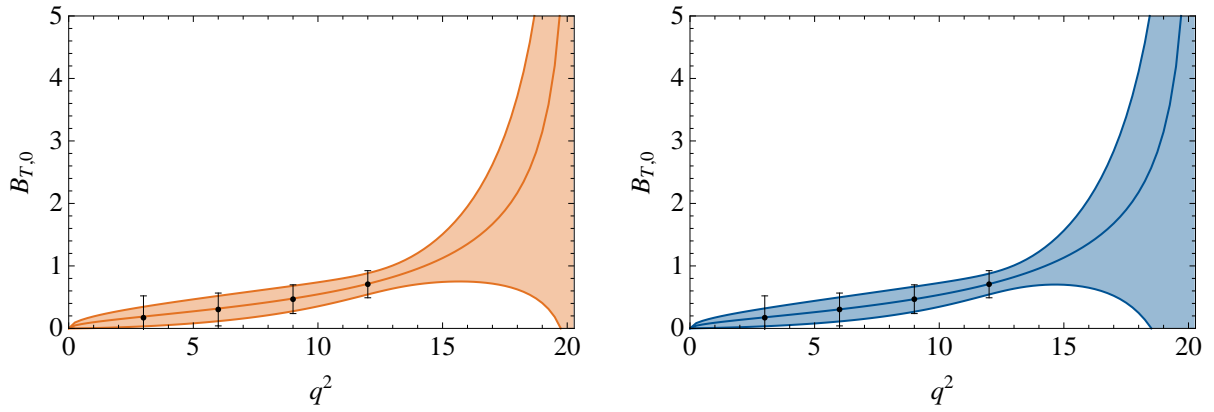


**Figure 5.9:**  $B \rightarrow \rho$ : Fit of SE (left) and SSE (right) parametrizations to LCSR for  $\mathcal{B}_{T,0}$ . The LCSR data is shown by black points with error bars.

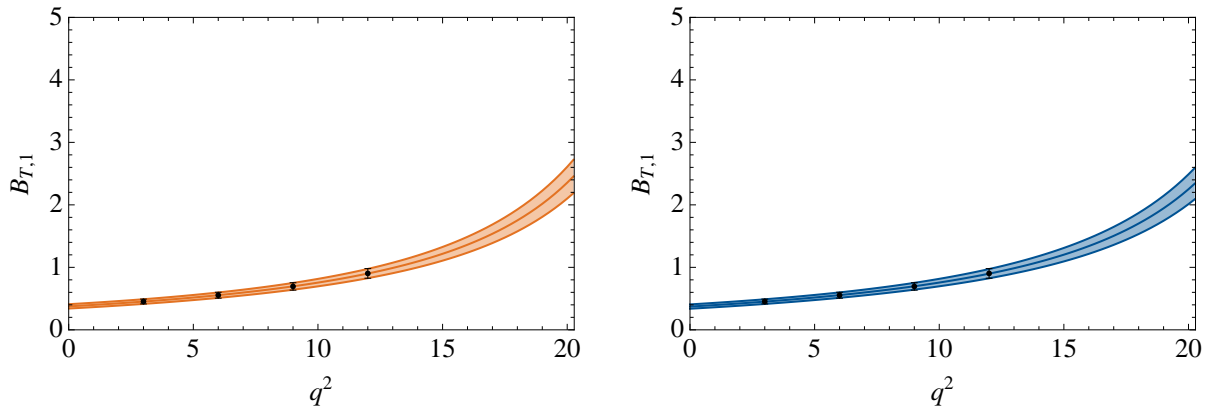


**Figure 5.10:**  $B \rightarrow \rho$ : Fit of SE (left) and SSE (right) parametrizations to LCSR for  $\mathcal{B}_{T,1}$ . The LCSR data is shown by black points with error bars.

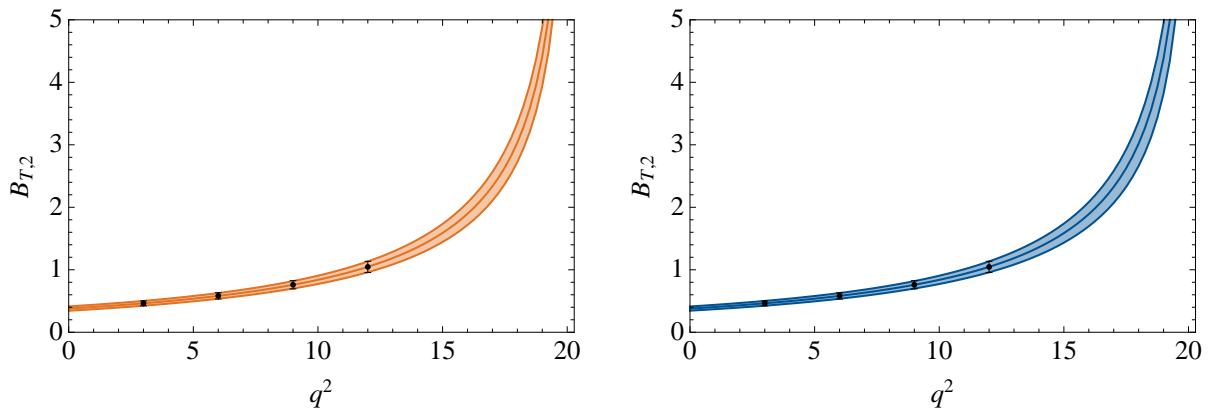


**Figure 5.11:**  $B \rightarrow \rho$ : Fit of SE (left) and SSE (right) parametrizations to LCSR for  $\mathcal{B}_{T,2}$ . The LCSR data is shown by black points with error bars.

# Chapter 6

## Summary and Outlook

Based on helicity form factors, we defined in this thesis a new set of form factors. These definition has many advantages over the traditional, some are definite spin-parity quantum numbers, simple relations to the universal form factors, particular simple expressions for the observables in the  $B \rightarrow (P, V) (\ell^+ \ell^-, \ell^+ \nu, \nu \bar{\nu})$  decays, new symmetric and universal dispersive bounds.

Using these form factor definition combined with recent LCSR results we have performed a new analysis of the decays  $B \rightarrow K^* \nu \bar{\nu}$ ,  $B \rightarrow K \nu \bar{\nu}$  and  $B \rightarrow X_s \nu \bar{\nu}$  in the SM, model-independently and in a number of new physics scenarios. The the set of observables for the three decays includes in addition to the three branching ratios the fraction of longitudinal polarized  $K^*$  meson produced in the decay  $B \rightarrow K^* \nu \bar{\nu}$ . The results of our analysis the observables can be summarized as follow:

- Our new SM prediction of  $\text{BR}(B \rightarrow K^* \nu \bar{\nu}) = (6.8_{-1.1}^{+1.0}) \times 10^{-6}$  improved form factors is significantly lower than the ones present in the literature. The improved estimate of the inclusive  $\text{BR}(B \rightarrow X_s \nu \bar{\nu}) = (2.7 \pm 0.2) \times 10^{-5}$  in the SM is considerably more accurate than the ones present in the literature.
- The two, in general complex, Wilson coefficients,  $C_L^\nu$  and  $C_R^\nu$ , of the most general effective theory of new physics with the low-energy SM particle content are found to enter the observables only in two real combinations,  $(\epsilon, \eta)$ . This means that every model of NP corresponds to a point on the  $(\epsilon, \eta)$  plane or in turn a measurement of one (integrated) observable leads to an excluded/allowed area on this plane. Measuring all four observables would lead to four overlapping areas, with the actual  $(\epsilon, \eta)$  point in the intersection area.
- The presence of a hypothetical, scalar singlet under the SM gauge group, which

---

couples to the  $b \rightarrow s$  transitions, would be signaled transparently in the  $(\epsilon, \eta)$  plane through the absence of an intersection point. Furthermore, this scenario would lead to characteristic edges in the  $q^2$  distributions.

- Modified  $Z$  penguins can lead to sizable deviations from the SM prediction for the four observables and give rise to an interesting interplay of  $b \rightarrow s\ell^+\ell^-$  and  $b \rightarrow s\nu\bar{\nu}$  based transitions, especially with  $\text{BR}(B \rightarrow X_s\ell^+\ell^-)$ .
- NP effects in the considered observables in the LHT models where by construction right-handed currents are absent are found to be small. The same holds for a RS model with custodial protection of left-handed  $Z$ -couplings.
- Sizable NP effects in the MSSM with a generic flavor violating soft sector contributions are still allowed by of the full set of constraints. The dominant origin of effects in  $C_L^\nu$  is identified to be the chargino contribution. The analysis of the here presented correlation of  $\text{BR}(B \rightarrow K^*\nu\bar{\nu})$  and  $\text{BR}(B_s \rightarrow \mu^+\mu^-)$  provides a promising way to probe a particular MSSM scenario.

In chapter 3, we have presented an extensive analysis of the angular observables in the decay  $B \rightarrow K^*(\rightarrow K\pi)\mu^+\mu^-$ . The set of CP-conserving and CP-violating quantities  $A_i^{(a)}$  and  $S_i^{(a)}$  here defined constitute the first systematical definition of a complete set of observables. Furthermore, the observables are very clean due to maximal cancellation of the parametric and hadronic uncertainties. The main results of our analysis are:

- The SM prediction of some  $S_i^{(a)}$  turns out to be relatively large and all of the  $A_i^{(a)}$  are close to zero in the SM.
- The here outlined approach is found to be a theoretically clean test of the scalar sector of a theory beyond the SM and, furthermore, it is complementary to  $B_s \rightarrow \mu^+\mu^-$ .
- As the  $A_i^{(a)}$  probe CP violation they are, as expected, in MFV models as small as in the SM. However, the  $S_i^{(a)}$ , in particular  $S_4$ ,  $S_5$  and  $S_6^c$  can show deviations from the SM.
- In the FBMSSM several  $S_i^{(a)}$  and  $A_i^{(a)}$  differ significantly, even by orders of magnitude, from the SM results. Furthermore, correlations among the observables and also with other flavor observables, e.g. the correlations between  $A_7$  (and  $A_8$ ) and  $A_{CP}(b \rightarrow s\gamma)$  and  $S_{\phi K_S}$ , show characteristic patterns.

## 6. Summary and Outlook

---

- An entirely different pattern has been found in the LHT model, where only the CP asymmetries  $A_7$  and  $A_8$  differ significantly from the SM predictions.
- The enormous number of parameters in the general MSSM makes the identification of definite patterns very difficult. However, almost all observables considered receive potentially large correction with respect to the SM results and the pattern of deviations can differ from those found in the FBMSSM and LHT models.

In chapter 4, we studied transition form factors for radiative and rare semi-leptonic  $B$ -meson decays into light pseudoscalar or vector mesons, combining theoretical and phenomenological constraints from Lattice QCD, LCSR and dispersive bounds. The results of our analysis are summarized by the following statements:

- We demonstrated that the helicity form factors, parametrized in terms of a series expansion in the variable  $z(q^2)$ , allow to fit conveniently the radiative and semi-leptonic decays of  $B$  mesons into light pseudoscalar or vector mesons. Already an expansion in only two terms, interpolates excellently both, the current estimates from LCSR and (where available) Lattice QCD results.
- The dispersive bounds expressed in terms of helicity form factors take a particular simple form, which is universal for vector and tensor form factors. Furthermore, we stress that for decays into vector mesons the dispersive bounds constrain the sum of (squared) coefficients. This allows to fit all form factors for a given current simultaneously, which improves the strength of the constraints compared to those for the individual form factors in that sum.
- In order to determine the correct normalization of the series expansion we calculate the current correlators using an operator product expansion, including next-to-leading order perturbative corrections and the leading non-perturbative contributions from quark, gluon and mixed condensates. In particular, we provide the next-to-leading order results for the tensor-current correlation functions, which are relevant for the form factors appearing in radiative and rare semi-leptonic  $B$  decays.
- We have performed numerical fits to LCSR (Lattice) predictions at low (medium) momentum transfer for all the form factors appearing in  $B \rightarrow K$  and  $B \rightarrow \rho$  transitions. In those cases, where Lattice estimates of the form factors is lacking, the SE is used to extrapolate the LCSR predictions to the high- $q^2$  region. Comparing fits

---

with/without using the available Lattice data for  $B \rightarrow K$  and  $B \rightarrow \rho$  transitions, we judge these extrapolations to be rather reliable.

A further improvement of our approach would be the calculation of LCSRs directly in the helicity basis.

Clearly, it will be very exciting to monitor the upcoming LHC, Belle upgrade and eventually Super-B factory in this decade to see whether the angular observables in the decay  $B \rightarrow K^*(\rightarrow K\pi)\mu^+\mu^-$  and  $B \rightarrow K^*(\rightarrow K\pi)\nu\bar{\nu}$  discussed in this thesis can give a hint for any of the extensions of the SM.

# Appendix A

## Kinematics and Polarization Vectors

In the following, we consider the rest frame of the decaying  $B$ -meson, with the 3-momentum of the final-state meson pointing in the  $z$ -direction. The polarisation vectors for a (virtual) vector state, with 4-momentum  $q^\mu = (q^0, 0, 0, -|\vec{q}|)$ , are defined as

$$\begin{aligned}\varepsilon_\pm^\mu(q) &= \mp \frac{1}{\sqrt{2}} (0, 1, \mp i, 0), & \varepsilon_0^\mu(q) &= \frac{1}{\sqrt{q^2}} (|\vec{q}|, 0, 0, -q^0), \\ \varepsilon_t^\mu(q) &= \frac{1}{\sqrt{q^2}} q^\mu.\end{aligned}\tag{A.1}$$

For the decay of a  $B$ -meson at rest into a light meson with mass  $m_L$  and momentum  $\vec{k}$ , we have in particular

$$q^0 = m_B - E = \frac{m_B^2 - m_L^2 + q^2}{2m_B}, \quad |\vec{q}| = |\vec{k}| = \frac{\sqrt{\lambda}}{2m_B},\tag{A.2}$$

with  $\lambda$  defined in (2.6). We also define the linear combinations

$$\varepsilon_1^\mu(q) = \frac{\varepsilon_-^\mu(q) - \varepsilon_+^\mu(q)}{\sqrt{2}} = (0, 1, 0, 0), \quad \varepsilon_2^\mu(q) = \frac{\varepsilon_-^\mu(q) + \varepsilon_+^\mu(q)}{\sqrt{2}} = (0, 0, i, 0).\tag{A.3}$$

In the same way, the polarisation vectors for an on-shell  $K^*$  meson with momentum  $k^\mu = (E, 0, 0, |\vec{k}|)$  are given as

$$\varepsilon_\pm^\mu(k) = \mp \frac{1}{\sqrt{2}} (0, 1, \pm i, 0), \quad \varepsilon_0^\mu(k) = \frac{1}{m_{K^*}} (|\vec{k}|, 0, 0, E).\tag{A.4}$$



# Appendix B

## Calculation of Wilson Coefficients

### B.1 Perturbative Contribution

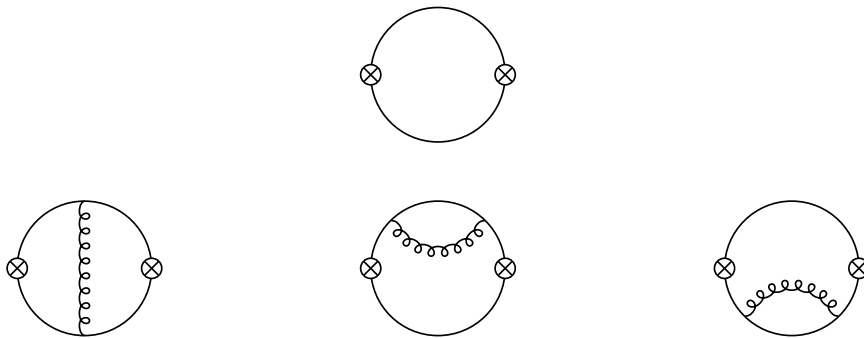


**Figure B.1:** One- and two-loop diagrams contributing to the correlation function. The crossed circle indicates the insertion of the corresponding scalar, vector or tensor currents. The counter-term diagrams related to the fermion self-energies are not shown.

In this section, we will briefly sketch the evaluation of the one- and two-loop diagrams (see Fig. B.1) contributing to the perturbative part of the correlation functions. We will specify the necessary number  $n$  of subtractions for the scalar, vector and tensor correlators, and determine the corresponding values of  $\chi_I^X(n)$  from the Taylor expansion of the Wilson coefficients at  $q^2 = 0$ . This leads to a major simplification in the calculation, which allows to eliminate external momenta in propagator denominators and to use tensor reduction and recursion relations to express the two-loop integrals in terms of two fundamental master integrals. Furthermore, we will follow the procedure explained in [15] and absorb the IR-sensitive contributions to the Feynman integrals (in the limit

$m \rightarrow 0$ ) into the corresponding condensate terms, such that our results have a finite limit when  $m \rightarrow 0$ .

We will find it useful to present the result in terms of the dimensionless variable

$$v \equiv \frac{M - m}{M + m}, \quad (\text{B.1})$$

where  $M$  and  $m$  are the masses of the heavy and light quark in the loop. We further define the functions

$$\begin{aligned} f_1(v) &\equiv \frac{1 - v^2}{v} \operatorname{atanh}[v], \\ f_2(v) &\equiv \frac{1}{v} \ln \left[ \frac{1 - v}{1 + v} \right] - \frac{2}{1 - v} \ln \left[ \frac{1 + v}{2} \right] - \frac{2}{1 + v} \ln \left[ \frac{1 - v}{2} \right], \\ f_3(v) &\equiv \frac{1}{v} \operatorname{Li}_2 \left[ \frac{4v}{(1 + v)^2} \right] - \frac{1}{v} \operatorname{Li}_2 \left[ -\frac{4v}{(1 - v)^2} \right] - \frac{4(1 + v^2)}{v^2} \operatorname{atanh}^2[v], \end{aligned} \quad (\text{B.2})$$

which are manifestly symmetric under exchange of light and heavy quarks ( $v \rightarrow -v$ ), and take finite values in the limits  $v \rightarrow \{-1, 0, 1\}$ .

We will quote our results for scalar, vector and tensor currents. The expressions for currents with opposite parity can be simply obtained by changing  $v \rightarrow 1/v$ . Our expressions for scalar and vector currents coincide with [15]; the results for the tensor currents are new.

**Scalar Correlator:** For the correlator of two scalar currents, we obtain

$$\chi^S(n = 2) \Big|_{\text{LO}} = \frac{(3 + v^2)(3v^2 - 1)}{64\pi^2(M + m)^2 v^4} \xrightarrow{v \rightarrow 1} \frac{1}{8\pi^2 M^2}, \quad (\text{B.3})$$

$$\begin{aligned} \chi^S(n = 2) \Big|_{\text{NLO}} &= \frac{\alpha_s C_F}{4\pi} \frac{1}{64\pi^2(M + m)^2 v^4} \left\{ \right. \\ &6(3f_1(1 - v^2)^2 + (3 + v^2)(3v^2 - 1)) \left( f_2(1 - v^2) - 4 \ln \left[ \frac{m + M}{\mu} \right] \right) \\ &- f_1^2(11v^4 - 50v^2 + 23) + f_1(47v^4 - 126v^2 + 103) \\ &\left. + 4f_3 v^2(5v^2 - 1) + 2(29v^4 + 65v^2 - 40) \right\} \\ &\xrightarrow{v \rightarrow 1} \frac{1}{8\pi^2 M^2} \frac{\alpha_s C_F}{4\pi} \left\{ -24 \ln \left[ \frac{M}{\mu} \right] + \frac{2\pi^2}{3} + \frac{27}{2} \right\}. \end{aligned} \quad (\text{B.4})$$

**Vector Correlator:** For the different projections of the correlator of two vector currents, we obtain

$$\chi_L^V(n=1)\Big|_{\text{LO}} = \frac{(3+v^2)(3v^2-1)}{64\pi^2 v^2} \xrightarrow{v \rightarrow 1} \frac{1}{8\pi^2}, \quad (\text{B.5})$$

$$\begin{aligned} \chi_L^V(n=1)\Big|_{\text{NLO}} &= \frac{\alpha_s C_F}{4\pi} \frac{1}{64\pi^2 v^2} \left\{ \right. \\ &\quad f_1^2 (25v^4 + 14v^2 - 23) + 2f_1 (19v^4 - 6v^2 + 23) \\ &\quad \left. + 4f_3 v^2 (5v^2 - 1) - 23 + 14v^2 + 13v^4 \right\}, \\ &\xrightarrow{v \rightarrow 1} \frac{\alpha_s C_F}{4\pi} \frac{1}{8\pi^2} \left( \frac{1}{2} + \frac{2\pi^2}{3} \right), \end{aligned} \quad (\text{B.6})$$

and

$$\chi_T^V(n=2)\Big|_{\text{LO}} = \frac{-21v^6 + 53v^4 + 13v^2 + 3}{512\pi^2 (M+m)^2 v^4} \xrightarrow{v \rightarrow 1} \frac{3}{32\pi^2 M^2}, \quad (\text{B.7})$$

$$\begin{aligned} \chi_T^V(n=2)\Big|_{\text{NLO}} &= \frac{\alpha_s C_F}{4\pi} \frac{1}{1536\pi^2 (M+m)^2 v^4} \left\{ \right. \\ &\quad -f_1^2 (803v^6 - 863v^4 - 155v^2 - 73) - 2f_1 (677v^6 - 741v^4 + 279v^2 + 73) \\ &\quad \left. - 4f_3 v^2 (19v^4 - 86v^2 - 5) + 73 + 323v^2 + 755v^4 - 551v^6 \right\}, \\ &\xrightarrow{v \rightarrow 1} \frac{\alpha_s C_F}{4\pi} \frac{3}{32\pi^2 M^2} \left( \frac{25}{6} + \frac{2\pi^2}{3} \right). \end{aligned} \quad (\text{B.8})$$

**Tensor Correlator:** The relevant projection of the tensor current gives rise to

$$\begin{aligned} \chi_T^T(n=3)\Big|_{\text{LO}} &= \frac{-9f_1 (v^2-1)^2 (3v^2+1) + 4(-9v^6 + 21v^4 + v^2 + 3)}{256\pi^2 (m+M)^2 v^4} \\ &\xrightarrow{v \rightarrow 1} \frac{1}{4\pi^2 M^2} \end{aligned} \quad (\text{B.9})$$

$$\begin{aligned} \chi_T^T(n=3)\Big|_{\text{NLO}} &= \frac{\alpha_s C_F}{4\pi} \frac{1}{384\pi^2 (M+m)^2 v^4} \left\{ \right. \\ &\quad 12 (3(v^2-1)^2 (3v^2+1) f_1 - 3 - v^2 - 21v^4 + 9v^6) \\ &\quad \times \left( f_2 (1-v^2) - 4 \ln \left[ \frac{m+M}{\mu} \right] \right) \\ &\quad \left. - f_1^2 (766v^6 - 598v^4 - 142v^2 - 218) \right\} \end{aligned}$$

$$\left. \begin{aligned} & -f_1 (1091v^6 - 1137v^4 + 297v^2 + 325) \\ & -8f_3 v^2 (7v^4 - 26v^2 - 5) + 107 + 69v^2 + 469v^4 - 325v^6 \end{aligned} \right\} \\ \xrightarrow{v \rightarrow 1} \frac{\alpha_s C_F}{4\pi} \frac{1}{4\pi^2 M^2} \left( \frac{10}{3} + \frac{2\pi^2}{3} + 8 \ln \left[ \frac{M}{\mu} \right] \right). \quad (\text{B.10})$$

## B.2 Condensate Contribution to the Correlation Functions

In this section we provide the expressions for the contributions of the gluon condensate, the quark condensate and the mixed quark-gluon condensate to the various current correlators. The contributions to the coefficient of the scalar and vector correlators to all orders in the quark mass and lowest order in the coupling constant can already be found in [15], and we reproduce the results given in that paper. We extend this analysis by determining the coefficient functions for the tensor correlators. For the quark and the quark-gluon condensate, we employ techniques analogous to that given in [15] and closely follow their notation. In case of the gluon condensate, we use the plane-wave technique.

**Quark Condensate and Quark–Gluon Condensate:** The starting point for calculating the coefficient functions to all orders in the quark masses is a closed expression for the non-local quark condensate. The position-space expressions for the projection of the non-local quark condensates on the local quark condensate  $\langle : \bar{q}q : \rangle^{(0)}$  and the local mixed quark-gluon condensate  $\langle : g_s \bar{q} \sigma F q : \rangle^{(0)}$  read

$$\begin{aligned} \langle : \bar{q}_\alpha(0) q_\beta(x) : \rangle_{\bar{q}q} &= \frac{1}{4m} \langle : \bar{q}q : \rangle^{(0)} \Gamma \left( \frac{D}{2} \right) (i \not{\partial} + m)_{\beta\alpha} \sum_{n=0}^{\infty} \frac{(-m^2 x^2/4)^n}{n! \Gamma(n + D/2)}, \\ \langle : \bar{q}_\alpha(0) q_\beta(x) : \rangle_{\bar{q}Fq} &= -\frac{1}{8m^3} \langle : g_s \bar{q} \sigma F q : \rangle^{(0)} \Gamma \left( \frac{D}{2} \right) \\ &\quad \times \sum_{n=0}^{\infty} \left[ (n-1) i \not{\partial} + n m \right]_{\beta\alpha} \frac{(-m^2 x^2/4)^n}{n! \Gamma(n + D/2)}. \end{aligned} \quad (\text{B.11})$$

## B. Calculation of Wilson Coefficients

---

Here  $\alpha$  and  $\beta$  indicate the spinor indices. The corresponding projection of the non-local mixed quark-gluon condensate reads

$$\begin{aligned} \langle :g_s \bar{q}_\alpha(0) F_{\mu\nu}(0) q_\beta(x): \rangle_{\bar{q}Fq} &= \frac{1}{4(D-1)(D-2)m^2} \langle :g_s \bar{q}\sigma Fq: \rangle^{(0)} \Gamma\left(\frac{D}{2}\right) \\ &\times \left[ \left( (\gamma_\mu \partial_\nu - \gamma_\nu \partial_\mu) + m\sigma_{\mu\nu} \right) (i\not{\partial} + m) \right]_{\beta\alpha} \sum_{n=0}^{\infty} \frac{(-m^2 x^2/4)^n}{n! \Gamma(n + D/2)}. \end{aligned} \quad (\text{B.12})$$

The relevant diagrams for the contribution of the non-local quark condensate and the non-local mixed quark-gluon condensate are given in Figs. B.2 and ??, respectively.



**Figure B.2:** Diagrams involving the non-local quark condensate, indicated by the two solid dots. The crossed circle symbolises the insertion of the currents.

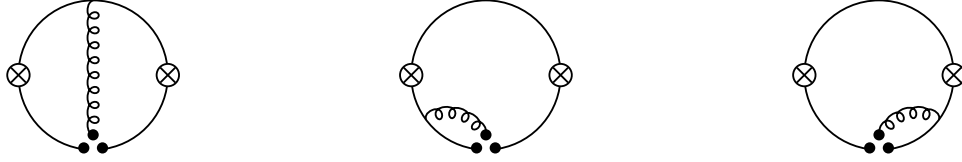


**Figure B.3:** Diagrams involving the non-local mixed quark-gluon condensate, indicated by the three solid dots.

The evaluation of the diagrams is simplified by the use of the equations of motion,

$$(\not{p} - m) \langle :g_s \bar{q}_\alpha(0) F_{\mu\nu}(0) q_\beta(x): \rangle_{\bar{q}Fq} = 0, \quad (\text{B.13})$$

$$(p^2 - m^2) \langle : \bar{q}(0) \tilde{q}(p) : \rangle_{\bar{q}Fq} = -\frac{\langle :g_s \bar{q}\sigma Fq: \rangle^{(0)}}{2 \langle : \bar{q}q : \rangle^{(0)}} \langle : \bar{q}(0) \tilde{q}(p) : \rangle_{\bar{q}q}, \quad (\text{B.14})$$

$$(\not{p} - m) \langle : \bar{q}(0) \tilde{q}(p) : \rangle_{\bar{q}q} = 0. \quad (\text{B.15})$$

**Gluon Condensate:** For the gluon condensate, it is more convenient to use the so-called fixed-point gauge technique, which is described in detail in [16]. In the framework

of the fixed-point gauge, it is possible to derive an expression for

$$\text{---} \begin{array}{c} \bullet \\ \vdots \\ \text{---} \end{array} = -\frac{i}{4} g t^a G_{\kappa\lambda}^a(0) \frac{1}{(p^2 - m^2)} \{ \sigma_{\kappa\lambda} (\not{p} + m) + (\not{p} + m) \sigma_{\kappa\lambda} \}, \quad (\text{B.16})$$

which is the basic building block for three lowest-order diagrams shown in Fig. B.4.

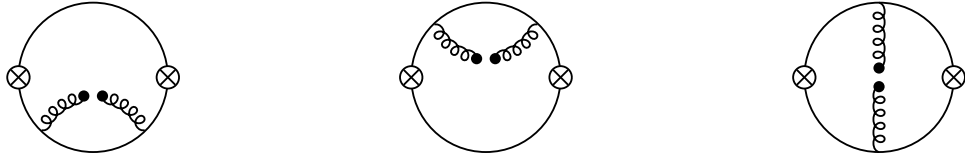


**Figure B.4:** Diagrams involving the gluon condensate.

## B.3 Results

**Quark Condensate:** The quark-condensate contribution to the coefficient for the scalar correlation function is given by

$$\chi^S(n=2) \Big|_{\bar{q}q} = \frac{\langle \bar{q}q \rangle (v+1)^3}{8(m+M)^5 v^5} \xrightarrow{v \rightarrow 1} \frac{\langle \bar{q}q \rangle}{M^5}. \quad (\text{B.17})$$

The same expression (up to an overall normalization factor) is obtained in case of the longitudinal projection of the vector correlator,  $\chi_L^V(n=1) \Big|_{\bar{q}q} = (M+m)^2 v^2 \chi^S(n=2) \Big|_{\bar{q}q}$ . The transverse projection of the vector correlator leads to

$$\chi_T^V(n=2) \Big|_{\bar{q}q} = -\frac{\langle \bar{q}q \rangle (v+1)^3}{64(m+M)^5 v^5} (7v^2 + 1) \xrightarrow{v \rightarrow 1} -\frac{\langle \bar{q}q \rangle}{M^5}. \quad (\text{B.18})$$

Finally, from the relevant tensor correlator we obtain

$$\chi_T^T(n=3) \Big|_{\bar{q}q} = -\frac{\langle \bar{q}q \rangle (v+1)^3}{32(m+M)^5 v^5} (3v^2 + 1) \xrightarrow{v \rightarrow 1} -\frac{\langle \bar{q}q \rangle}{M^5}. \quad (\text{B.19})$$

**Gluon Condensate:** The expressions for the gluon-condensate contributions to the various  $\chi_I^X$  coefficients read as follows: For the scalar correlator we obtain

$$\begin{aligned} \chi^S(n=2)|_{G^2} &= \frac{\langle \frac{\alpha}{\pi} G^2 \rangle}{96 (m+M)^6 v^6} \left\{ 15f_1 (1-v^2)^2 - 15 - 4v^2 + 27v^4 \right. \\ &\quad \left. - 6v^2(1-v^2) \left( f_2(1-v^2) - 4 \ln \left[ \frac{m+M}{\mu} \right] \right) \right\} \\ &\xrightarrow{v \rightarrow 1} \frac{\langle \frac{\alpha}{\pi} G^2 \rangle}{12M^6}. \end{aligned} \quad (\text{B.20})$$

Again, the same expression is obtained for the longitudinal projection of the vector correlator,  $\chi_L^V(n=1)|_{GG} = (M+m)^2 v^2 \chi^S(n=2)|_{GG}$ . For the transverse projection of the vector correlator, one has

$$\begin{aligned} \chi_T^V(n=2)|_{G^2} &= \frac{\langle \frac{\alpha}{\pi} G^2 \rangle}{384 (m+M)^6 v^6} \left\{ \right. \\ &\quad 45 + 115v^2 + 3v^4 - 195v^6 - 5f_1 (1-v^2)^2 (25v^2 + 9) \\ &\quad \left. + v^2(1-v^2) (35v^2 + 41) \left( f_2(1-v^2) - 4 \ln \left[ \frac{m+M}{\mu} \right] \right) \right\} \\ &\xrightarrow{v \rightarrow 1} -\frac{\langle \frac{\alpha}{\pi} G^2 \rangle}{12M^6}, \end{aligned} \quad (\text{B.21})$$

and for the tensor correlator, we get

$$\begin{aligned} \chi_T^T(n=3)|_{G^2} &= \frac{\langle \frac{\alpha}{\pi} G^2 \rangle}{384 (m+M)^6 v^6} \left\{ \right. \\ &\quad 105 + 91v^2 - 17v^4 - 195v^6 - 5f_1 (1-v^2)^2 (27v^2 + 17) \\ &\quad \left. + 2(1-v^2) (15v^4 + 24v^2 + 5) \left( f_2(1-v^2) - 4 \ln \left[ \frac{m+M}{\mu} \right] \right) \right\} \\ &\xrightarrow{v \rightarrow 1} -\frac{\langle \frac{\alpha}{\pi} G^2 \rangle}{24M^6}. \end{aligned} \quad (\text{B.22})$$

**Mixed Condensate:** For the mixed-condensate contributions, we finally obtain

$$\chi^S(n=2)|_{\bar{q}Gq} = -\frac{\langle \bar{q}Gq \rangle (1+v)}{4(m+M)^7 v^5} (2+v) \xrightarrow{v \rightarrow 1} -\frac{3\langle \bar{q}Gq \rangle}{2M^7}, \quad (\text{B.23})$$

and

$$\chi_L^V(n=1)|_{\bar{q}Gq} = -\frac{\langle \bar{q}Gq \rangle (1+v)}{4(m+M)^5 v^3} (2+v) \xrightarrow{v \rightarrow 1} -\frac{3\langle \bar{q}Gq \rangle}{2M^5}, \quad (\text{B.24})$$

where  $\chi_L^V(n=1)|_{\bar{q}Gq}$  is again proportional to  $\chi^S(n=2)|_{\bar{q}Gq}$ , as well as

$$\chi_T^V(n=2)|_{\bar{q}Gq} = \frac{\langle \bar{q}Gq \rangle (1+v)}{96(m+M)^7 v^5} (35v^3 + 59v^2 + 41v + 9) \xrightarrow{v \rightarrow 1} \frac{3\langle \bar{q}Gq \rangle}{M^7}, \quad (\text{B.25})$$

and

$$\begin{aligned} \chi^{TT}(n=3)|_{\bar{q}Gq} &= \frac{\langle \bar{q}Gq \rangle (1+v)}{48(m+M)^7 v^6} (15v^4 + 28v^3 + 24v^2 + 12v + 5) \\ &\xrightarrow{v \rightarrow 1} \frac{7\langle \bar{q}Gq \rangle}{2M^7}. \end{aligned} \quad (\text{B.26})$$

## B.4 Decomposition of the tensor-current correlator

Using the projectors

$$P_L^{\mu\nu} = \frac{q^\mu q^\nu}{q^2}, \quad P_T^{\mu\nu} = \frac{(q^\mu q^\nu - g^{\mu\nu} q^2)}{(D-1)q^2}, \quad (\text{B.27})$$

we decompose the correlator of general tensor currents,

$$\Pi_{\mu\nu\alpha\beta} = i \int d^4x e^{iqx} \langle 0|T[\bar{q}_1(x)\sigma_{\mu\nu}q_2(x) \bar{q}_2(0)\sigma_{\alpha\beta}q_1(0)]|0\rangle, \quad (\text{B.28})$$

into the two Lorentz-invariant functions  $\Pi_{TT}$  and  $\Pi_{LT}$  as follows,

$$\begin{aligned} \Pi_{\mu\nu\alpha\beta} &= [g_{\mu\alpha}g_{\nu\beta} - g_{\mu\beta}g_{\nu\alpha}] \frac{3\Pi_{TT}(q^2)}{2} \\ &+ \frac{g_{\mu\beta}q_\nu q_\alpha + g_{\nu\alpha}q_\mu q_\beta - g_{\mu\alpha}q_\nu q_\beta - g_{\nu\beta}q_\mu q_\alpha}{q^2} \left( \frac{3\Pi_{TT}(q^2)}{2} + \Pi_{LT}(q^2) \right) \end{aligned} \quad (\text{B.29})$$

where

$$\begin{aligned} P_L^{\mu\alpha} P_T^{\nu\beta} \Pi_{\mu\nu\alpha\beta} &= P_T^{\mu\alpha} P_L^{\nu\beta} \Pi_{\mu\nu\alpha\beta} = \Pi_{LT}(q^2), \\ P_T^{\mu\alpha} P_T^{\nu\beta} \Pi_{\mu\nu\alpha\beta} &= \Pi_{TT}(q^2), \\ P_L^{\mu\alpha} P_L^{\nu\beta} \Pi_{\mu\nu\alpha\beta} &= 0. \end{aligned} \quad (\text{B.30})$$

## B. Calculation of Wilson Coefficients

---

In this notation, the correlator of the currents

$$j_\mu^T = \bar{q} \sigma_{\mu\alpha} q^\alpha \quad (\text{B.31})$$

leads to  $q^2 \Pi_{LT}(q^2)$ .



# Appendix C

## Input Data for the Series Expansion

**Table C.1:** Overview of LCSR points used, transformed to the helicity amplitude basis.

Decay	form factors	LCSR/ $q^2$ (GeV <sup>2</sup> )				Ref.
		3	6	9	12	
$B \rightarrow K$	$q^2$					Table 3, [37]
	$\mathcal{A}_{V,0}$	$0.40 \pm 0.05$	$0.48 \pm 0.06$	$0.59 \pm 0.07$	-	
	$\mathcal{A}_{V,t}$	$0.40 \pm 0.05$	$0.51 \pm 0.06$	$0.65 \pm 0.08$	-	
	$\mathcal{A}_{T,0}$	$0.13 \pm 0.01$	$0.22 \pm 0.02$	$0.34 \pm 0.03$	-	
$B \rightarrow \rho$	$q^2$					Table 8, [18]
	$\mathcal{B}_{V,0}$	$0.37 \pm 0.12$	$0.46 \pm 0.13$	$0.60 \pm 0.14$	-	
	$\mathcal{B}_{V,1}$	$0.16 \pm 0.01$	$0.27 \pm 0.02$	$0.41 \pm 0.04$	-	
	$\mathcal{B}_{V,2}$	$0.16 \pm 0.02$	$0.29 \pm 0.03$	$0.46 \pm 0.04$	-	
	$\mathcal{B}_{V,t}$	$0.37 \pm 0.04$	$0.46 \pm 0.04$	$0.58 \pm 0.06$	-	
	$\mathcal{B}_{T,0}$	$0.17 \pm 0.35$	$0.3 \pm 0.26$	$0.47 \pm 0.23$	$0.71 \pm 0.22$	
	$\mathcal{B}_{T,1}$	$0.45 \pm 0.04$	$0.55 \pm 0.05$	$0.69 \pm 0.06$	$0.9 \pm 0.08$	
	$\mathcal{B}_{T,2}$	$0.46 \pm 0.04$	$0.58 \pm 0.05$	$0.76 \pm 0.07$	$1.0 \pm 0.1$	

**Table C.2:** Overview of Lattice points used, transformed to the helicity amplitude basis. Note that specific values for  $B \rightarrow \rho$  are as in Table 2 of Ref. [23].

Decay	$q^2$ (GeV <sup>2</sup> )	form factors			Ref.
$B \rightarrow K$		$\mathcal{A}_{V,0}$	$\mathcal{A}_{V,t}$	$\mathcal{A}_{T,0}$	QCDSF [120]
	14.5	$0.94 \pm 0.19$	$1.1 \pm 0.2$	-	
	15.6	$1.1 \pm 0.2$	$1.3 \pm 0.3$	-	
	16.7	$1.2 \pm 0.2$	$1.5 \pm 0.3$	-	
	17.9	$1.4 \pm 0.3$	$1.8 \pm 0.3$	-	
	19.	$1.6 \pm 0.3$	$2.3 \pm 0.4$	-	
	20.1	$1.9 \pm 0.4$	$3. \pm 0.6$	-	
	21.3	$2.3 \pm 0.4$	$4.4 \pm 0.8$	-	
	22.4	$2.9 \pm 0.6$	$8.7 \pm 1.7$	-	
$B \rightarrow \rho$		$\mathcal{B}_{V,0}$	$\mathcal{B}_{V,1}$	$\mathcal{B}_{T,2}$	UKQCD [121]
	12.7	$0.64 \pm 0.78$	$0.34 \pm 0.27$	$0.9 \pm 0.18$	
	13.	$0.71 \pm 0.72$	$0.39 \pm 0.25$	$0.96 \pm 0.18$	
	13.5	$0.8 \pm 0.66$	$0.48 \pm 0.22$	$1.1 \pm 0.2$	
	14.	$0.9 \pm 0.62$	$0.58 \pm 0.19$	$1.2 \pm 0.2$	
	14.5	$1.0 \pm 0.6$	$0.68 \pm 0.16$	$1.3 \pm 0.2$	
	15.	$1.1 \pm 0.6$	$0.78 \pm 0.15$	$1.4 \pm 0.2$	
	15.5	$1.3 \pm 0.7$	$0.89 \pm 0.15$	$1.6 \pm 0.2$	
	16.	$1.4 \pm 0.8$	$1.0 \pm 0.2$	$1.8 \pm 0.2$	
	16.5	$1.6 \pm 0.9$	$1.2 \pm 0.3$	$2.1 \pm 0.2$	
	17.1	$1.8 \pm 1.2$	$1.4 \pm 0.4$	$2.4 \pm 0.2$	
	17.6	$2.1 \pm 1.5$	$1.7 \pm 0.6$	$2.7 \pm 0.3$	
	18.2	$2.5 \pm 2.$	$2.1 \pm 0.9$	$3.3 \pm 0.3$	

### C. Input Data for the Series Expansion

---

**Table C.3:** Summary of OPE results for the coefficients  $\chi_I^X(n)$ . The following parameter values have been used [14, 125–127]:  $\mu = m_b = 4.2$  GeV,  $m_d = 4.8$  MeV,  $m_s = 104$  MeV,  $\alpha_s = 0.2185$ ,  $\langle \bar{d}d \rangle = (278 \text{ MeV})^3$ ,  $\langle \bar{s}s \rangle = 0.8 \langle \bar{d}d \rangle$ ,  $\langle \frac{\alpha_s}{\pi} G^2 \rangle = 0.038 \text{ GeV}^4$ ,  $\langle \bar{q}Gq \rangle = (1.4 \text{ GeV})^2 \langle \bar{q}q \rangle$ .

$q$	Correlator	Subtractions	LO	NLO	$\langle \bar{q}q \rangle$	$\langle \frac{\alpha_s}{\pi} G^2 \rangle$	$\langle \bar{q}Gq \rangle$	$\Sigma$
$d$	$100 \times m_b^2 \chi^S$	2	1.265	0.589	0.029	0.001	-0.003	1.88
	$100 \times m_b^2 \chi^P$	2	1.268	0.590	0.029	0.001	-0.003	1.88
	$100 \times \chi_L^V$	1	1.262	0.211	0.029	0.001	-0.003	1.50
	$100 \times \chi_L^A$	1	1.271	0.205	0.029	0.001	-0.003	1.50
	$100 \times m_b^2 \chi_T^V$	2	0.951	0.236	-0.029	-0.001	0.007	1.16
	$100 \times m_b^2 \chi_T^A$	2	0.948	0.237	-0.029	-0.001	0.007	1.16
	$100 \times m_b^2 \chi_T^T$	3	2.539	0.579	-0.029	-0.000	0.008	3.10
	$100 \times m_b^2 \chi_T^{AT}$	3	2.527	0.586	-0.029	-0.001	0.008	3.09
$s$	$100 \times m_b^2 \chi^S$	2	1.233	0.571	0.024	0.001	-0.003	1.83
	$100 \times m_b^2 \chi^P$	2	1.296	0.608	0.022	0.001	-0.003	1.93
	$100 \times \chi_L^V$	1	1.172	0.229	0.023	0.000	-0.003	1.42
	$100 \times \chi_L^A$	1	1.361	0.187	0.023	0.002	-0.003	1.57
	$100 \times m_b^2 \chi_T^V$	2	0.980	0.237	-0.022	0.000	0.005	1.20
	$100 \times m_b^2 \chi_T^A$	2	0.916	0.238	-0.024	-0.002	0.006	1.13
	$100 \times m_b^2 \chi_T^T$	3	2.652	0.569	-0.023	0.001	0.006	3.21
	$100 \times m_b^2 \chi_T^{AT}$	3	2.404	0.603	-0.024	-0.002	0.007	2.99



# Bibliography

- [1] S. Weinberg, “The cosmological constant problem,” *Rev. Mod. Phys.* **61** (1989) 1–23.
- [2] E. Gildener and S. Weinberg, “Symmetry Breaking and Scalar Bosons,” *Phys. Rev.* **D13** (1976) 3333.
- [3] P. H. Frampton, “Vacuum Instability and Higgs Scalar Mass,” *Phys. Rev. Lett.* **37** (1976) 1378.
- [4] H. Georgi, “THE FLAVOR PROBLEM,” *Phys. Lett.* **B169** (1986) 231.
- [5] C. G. Boyd and M. J. Savage, “Analyticity, shapes of semileptonic form factors, and  $B \rightarrow \pi l \bar{l}$ ,” *Phys. Rev.* **D56** (1997) 303–311, [arXiv:hep-ph/9702300](#).
- [6] N. Isgur and M. B. Wise, “Weak Transition Form Factors Between Heavy Mesons,” *Phys. Lett.* **B237** (1990) 527.
- [7] N. Isgur and M. B. Wise, “Weak Decays of Heavy Mesons in the Static Quark Approximation,” *Phys. Lett.* **B232** (1989) 113.
- [8] J. Charles, A. Le Yaouanc, L. Oliver, O. Pene, and J. C. Raynal, “Heavy-to-light form factors in the heavy mass to large energy limit of QCD,” *Phys. Rev.* **D60** (1999) 014001, [arXiv:hep-ph/9812358](#).
- [9] M. Beneke and T. Feldmann, “Symmetry-breaking corrections to heavy-to-light  $B$  meson form factors at large recoil,” *Nucl. Phys.* **B592** (2001) 3–34, [arXiv:hep-ph/0008255](#).
- [10] M. Beneke and T. Feldmann, “Spectator interactions and factorization in  $B \rightarrow \pi \ell \nu$  decay,” *Eur. Phys. J.* **C33** (2004) s241–s243, [arXiv:hep-ph/0308303](#).

- 
- [11] B. O. Lange and M. Neubert, “Factorization and the soft overlap contribution to heavy- to-light form factors,” *Nucl. Phys.* **B690** (2004) 249–278, [arXiv:hep-ph/0311345](#).
- [12] M. Beneke and T. Feldmann, “Factorization of heavy-to-light form factors in soft- collinear effective theory,” *Nucl. Phys.* **B685** (2004) 249–296, [arXiv:hep-ph/0311335](#).
- [13] P. Colangelo and A. Khodjamirian, “QCD sum rules, a modern perspective,” [arXiv:hep-ph/0010175](#).
- [14] M. A. Shifman, A. I. Vainshtein, and V. I. Zakharov, “QCD and Resonance Physics. Sum Rules,” *Nucl. Phys.* **B147** (1979) 385–447.
- [15] M. Jamin and M. Munz, “Current correlators to all orders in the quark masses,” *Z. Phys.* **C60** (1993) 569–578, [arXiv:hep-ph/9208201](#).
- [16] L. J. Reinders, H. Rubinstein, and S. Yazaki, “Hadron Properties from QCD Sum Rules,” *Phys. Rept.* **127** (1985) 1.
- [17] E. Dalgic *et al.*, “B Meson Semileptonic Form Factors from Unquenched Lattice QCD,” *Phys. Rev.* **D73** (2006) 074502, [arXiv:hep-lat/0601021](#).
- [18] P. Ball and R. Zwicky, “ $B_{d,s} \rightarrow \rho, \omega, K^*, \phi$  Decay Form Factors from Light-Cone Sum Rules Revisited,” *Phys. Rev.* **D71** (2005) 014029, [arXiv:hep-ph/0412079](#).
- [19] **Particle Data Group** Collaboration, C. Amsler *et al.*, “Review of particle physics,” *Phys. Lett.* **B667** (2008) 1.
- [20] W. A. Bardeen, E. J. Eichten, and C. T. Hill, “Chiral Multiplets of Heavy-Light Mesons,” *Phys. Rev.* **D68** (2003) 054024, [arXiv:hep-ph/0305049](#).
- [21] T. Becher and R. J. Hill, “Comment on form factor shape and extraction of  $|V_{ub}|$  from  $B \rightarrow \pi \ell \nu$ ,” *Phys. Lett.* **B633** (2006) 61–69, [arXiv:hep-ph/0509090](#).
- [22] D. Becirevic and A. B. Kaidlov, “Comment on the heavy to light form factors,” *Phys. Lett.* **B478** (2000) 417–423, [arXiv:hep-ph/9904490](#).
- [23] J. M. Flynn and J. Nieves, “ $|V_{ub}|$  from exclusive semileptonic  $B$  to  $\pi$  decays revisited,” *Phys. Rev.* **D76** (2007) 031302, [arXiv:0705.3553 \[hep-ph\]](#).

- [24] C. Bourrely, I. Caprini, and L. Lellouch, “Model-independent description of  $B \rightarrow \pi \ell \nu$  decays and a determination of  $|V_{ub}|$ ,” *Phys. Rev.* **D79** (2009) 013008, [arXiv:0807.2722 \[hep-ph\]](#).
- [25] M. C. Arnesen, B. Grinstein, I. Z. Rothstein, and I. W. Stewart, “A precision model independent determination of  $|V_{ub}|$  from  $B \rightarrow \pi \ell \nu$ ,” *Phys. Rev. Lett.* **95** (2005) 071802, [arXiv:hep-ph/0504209](#).
- [26] C. G. Boyd, B. Grinstein, and R. F. Lebed, “Constraints on form-factors for exclusive semileptonic heavy to light meson decays,” *Phys. Rev. Lett.* **74** (1995) 4603–4606, [arXiv:hep-ph/9412324](#).
- [27] I. Caprini, L. Lellouch, and M. Neubert, “Dispersive bounds on the shape of  $\bar{B} \rightarrow D^{(*)} \ell \bar{\nu}$  form factors,” *Nucl. Phys.* **B530** (1998) 153–181, [arXiv:hep-ph/9712417](#).
- [28] **Particle Data Group** Collaboration, C. Amsler *et al.*, “Review of particle physics,” *Phys. Lett.* **B667** (2008) 1.
- [29] M. Misiak and J. Urban, “QCD corrections to FCNC decays mediated by Z-penguins and W-boxes,” *Phys. Lett.* **B451** (1999) 161–169, [arXiv:hep-ph/9901278](#).
- [30] G. Buchalla and A. J. Buras, “The rare decays  $K \rightarrow \pi \nu \bar{\nu}$ ,  $B \rightarrow X \nu \bar{\nu}$  and  $B \rightarrow \ell^+ \ell^-$ : An update,” *Nucl. Phys.* **B548** (1999) 309–327, [arXiv:hep-ph/9901288](#).
- [31] **Tevatron Electroweak Working Group** Collaboration, “Combination of CDF and D0 Results on the Mass of the Top Quark,” [arXiv:0808.1089 \[hep-ex\]](#).
- [32] H. E. Haber, “Spin formalism and applications to new physics searches,” [arXiv:hep-ph/9405376](#).
- [33] F. Kruger, L. M. Sehgal, N. Sinha, and R. Sinha, “Angular distribution and CP asymmetries in the decays  $\bar{B} \rightarrow K^- \pi^+ e^- e^+$  and  $\bar{B} \rightarrow \pi^- \pi^+ e^- e^+$ ,” *Phys. Rev.* **D61** (2000) 114028, [arXiv:hep-ph/9907386](#).
- [34] C. S. Kim, Y. G. Kim, C.-D. Lu, and T. Morozumi, “Azimuthal angle distribution in  $B \rightarrow K^*(\rightarrow K \pi) \ell^+ \ell^-$  at low invariant  $m(\ell^+ \ell^-)$  region,” *Phys. Rev.* **D62** (2000) 034013, [arXiv:hep-ph/0001151](#).

- 
- [35] J. F. Kamenik and C. Smith, “Tree-level contributions to the rare decays  $B \rightarrow \pi \nu \bar{\nu}$ ,  $B \rightarrow K \nu \bar{\nu}$ , and  $B \rightarrow K^* \nu \bar{\nu}$  in the Standard Model,” *Phys. Lett.* **B680** (2009) 471–475, [arXiv:0908.1174](#) [hep-ph].
- [36] P. Colangelo, F. De Fazio, P. Santorelli, and E. Scrimieri, “Rare  $B \rightarrow K^{(*)} \nu \bar{\nu}$  decays at  $B$  factories,” *Phys. Lett.* **B395** (1997) 339–344, [arXiv:hep-ph/9610297](#).
- [37] P. Ball and R. Zwicky, “New Results on  $B \rightarrow \pi, K, \eta$  Decay Formfactors from Light- Cone Sum Rules,” *Phys. Rev.* **D71** (2005) 014015, [arXiv:hep-ph/0406232](#).
- [38] Y. Grossman, Z. Ligeti, and E. Nardi, “New limit on inclusive  $B \rightarrow X_s \bar{\nu} \nu$  decay and constraints on new physics,” *Nucl. Phys.* **B465** (1996) 369–398, [arXiv:hep-ph/9510378](#).
- [39] G. Buchalla, A. J. Buras, and M. E. Lautenbacher, “Weak decays beyond leading logarithms,” *Rev. Mod. Phys.* **68** (1996) 1125–1144, [arXiv:hep-ph/9512380](#).
- [40] C. Bobeth, A. J. Buras, F. Kruger, and J. Urban, “QCD corrections to  $\bar{B} \rightarrow X_{d,s} \nu \bar{\nu}$ ,  $\bar{B}_{d,s} \rightarrow \ell^+ \ell^-$ ,  $K \rightarrow \pi \nu \bar{\nu}$  and  $K_L \rightarrow \mu^+ \mu^-$  in the MSSM,” *Nucl. Phys.* **B630** (2002) 87–131, [arXiv:hep-ph/0112305](#).
- [41] A. F. Falk, M. E. Luke, and M. J. Savage, “Hadron spectra for semileptonic heavy quark decay,” *Phys. Rev.* **D53** (1996) 2491–2505, [arXiv:hep-ph/9507284](#).
- [42] C. W. Bauer, Z. Ligeti, M. Luke, A. V. Manohar, and M. Trott, “Global analysis of inclusive  $B$  decays,” *Phys. Rev.* **D70** (2004) 094017, [arXiv:hep-ph/0408002](#).
- [43] K. G. Chetyrkin, M. Misiak, and M. Munz, “Weak radiative  $B$  meson decay beyond leading logarithms,” *Phys. Lett.* **B400** (1997) 206–219, [arXiv:hep-ph/9612313](#).
- [44] A. H. Hoang, Z. Ligeti, and A. V. Manohar, “ $B$  decay and the Upsilon mass,” *Phys. Rev. Lett.* **82** (1999) 277–280, [arXiv:hep-ph/9809423](#).
- [45] A. H. Hoang, Z. Ligeti, and A. V. Manohar, “ $B$  decays in the Upsilon expansion,” *Phys. Rev.* **D59** (1999) 074017, [arXiv:hep-ph/9811239](#).

- [46] A. H. Hoang, “Bottom quark mass from Upsilon mesons: Charm mass effects,” [arXiv:hep-ph/0008102](#).
- [47] **BABAR** Collaboration, B. Aubert *et al.*, “Search for  $B \rightarrow K^* \nu \bar{\nu}$  decays,” *Phys. Rev.* **D78** (2008) 072007, [arXiv:0808.1338](#) [**hep-ex**].
- [48] **BELLE** Collaboration, K. F. Chen *et al.*, “Search for  $B \rightarrow h^{(*)} \nu \bar{\nu}$  Decays at Belle,” *Phys. Rev. Lett.* **99** (2007) 221802, [arXiv:0707.0138](#) [**hep-ex**].
- [49] **ALEPH** Collaboration, R. Barate *et al.*, “Measurements of  $\text{BR}(b \rightarrow \tau^- \bar{\nu}_\tau X)$  and  $\text{BR}(b \rightarrow \tau^- \bar{\nu}_\tau D^{*\pm} X)$  and upper limits on  $\text{BR}(b \rightarrow \tau^- \bar{\nu}_\tau au)$  and  $\text{BR}(b \rightarrow s \nu \bar{\nu})$ ,” *Eur. Phys. J.* **C19** (2001) 213–227, [arXiv:hep-ex/0010022](#).
- [50] **FlaviaNet Working Group on Kaon Decays** Collaboration, M. Antonelli *et al.*, “Precision tests of the Standard Model with leptonic and semileptonic kaon decays,” [arXiv:0801.1817](#) [**hep-ph**].
- [51] **UTfit** Collaboration, M. Bona *et al.*, “The unitarity triangle fit in the standard model and hadronic parameters from lattice QCD: A reappraisal after the measurements of  $\Delta(m_s)$  and  $\text{BR}(B \rightarrow \tau \nu / \tau)$ ,” *JHEP* **10** (2006) 081, [arXiv:hep-ph/0606167](#).
- [52] D. Melikhov, N. Nikitin, and S. Simula, “Right-handed currents in rare exclusive  $B \rightarrow (K, K^*) \nu \bar{\nu}$  decays,” *Phys. Lett.* **B428** (1998) 171–178, [arXiv:hep-ph/9803269](#).
- [53] T. Hurth, G. Isidori, J. F. Kamenik, and F. Mescia, “Constraints on New Physics in MFV models: A model independent analysis of  $\Delta F = 1$  processes,” *Nucl. Phys.* **B808** (2009) 326–346, [arXiv:0807.5039](#) [**hep-ph**].
- [54] A. J. Buras, P. Gambino, M. Gorbahn, S. Jager, and L. Silvestrini, “Universal unitarity triangle and physics beyond the standard model,” *Phys. Lett.* **B500** (2001) 161–167, [arXiv:hep-ph/0007085](#).
- [55] G. D’Ambrosio, G. F. Giudice, G. Isidori, and A. Strumia, “Minimal flavour violation: An effective field theory approach,” *Nucl. Phys.* **B645** (2002) 155–187, [arXiv:hep-ph/0207036](#).
- [56] G. Buchalla, G. Hiller, and G. Isidori, “Phenomenology of nonstandard  $Z$  couplings in exclusive semileptonic  $b \rightarrow s$  transitions,” *Phys. Rev.* **D63** (2000) 014015, [arXiv:hep-ph/0006136](#).

- [57] **BABAR** Collaboration, B. Aubert *et al.*, “Measurement of the  $B \rightarrow X_s \ell^+ \ell^-$  branching fraction with a sum over exclusive modes,” *Phys. Rev. Lett.* **93** (2004) 081802, [arXiv:hep-ex/0404006](#).
- [58] **Belle** Collaboration, M. Iwasaki *et al.*, “Improved measurement of the electroweak penguin process  $B \rightarrow X_s \ell^+ \ell^-$ ,” *Phys. Rev.* **D72** (2005) 092005, [arXiv:hep-ex/0503044](#).
- [59] **CDF** Collaboration, T. Aaltonen *et al.*, “Search for  $B_s^0 \rightarrow \mu^+ \mu^-$  and  $B_d^0 \rightarrow \mu^+ \mu^-$  decays with  $2fb^{-1}$  of  $p\bar{p}$  collisions,” *Phys. Rev. Lett.* **100** (2008) 101802, [arXiv:0712.1708 \[hep-ex\]](#).
- [60] **CDF** Collaboration, A. Abulencia *et al.*, “Observation of  $B_s^0 - \bar{B}_s^0$  oscillations,” *Phys. Rev. Lett.* **97** (2006) 242003, [arXiv:hep-ex/0609040](#).
- [61] W. Altmannshofer, A. J. Buras, D. M. Straub, and M. Wick, “New strategies for New Physics search in  $B \rightarrow K^* \nu \bar{\nu}$ ,  $B \rightarrow K \nu \bar{\nu}$  and  $B \rightarrow X_s \nu \bar{\nu}$  decays,” *JHEP* **04** (2009) 022, [arXiv:0902.0160 \[hep-ph\]](#).
- [62] **UTfit** Collaboration, M. Bona *et al.*, “First Evidence of New Physics in  $b \longleftrightarrow s$  Transitions,” *PMC Phys.* **A3** (2009) 6, [arXiv:0803.0659 \[hep-ph\]](#).
- [63] A. J. Lenz, “Search for new physics in  $B_s$ -mixing,” [arXiv:0808.1944 \[hep-ph\]](#).
- [64] **CDF** Collaboration, G. Brooijmans, “Mixing and CP Violation at the Tevatron,” [arXiv:0808.0726 \[hep-ex\]](#).
- [65] A. Lenz and U. Nierste, “Theoretical update of  $B_s - \bar{B}_s$  mixing,” *JHEP* **06** (2007) 072, [arXiv:hep-ph/0612167](#).
- [66] P. Ball and R. Fleischer, “Probing new physics through  $B$  mixing: Status, benchmarks and prospects,” *Eur. Phys. J.* **C48** (2006) 413–426, [arXiv:hep-ph/0604249](#).
- [67] C. Bird, P. Jackson, R. V. Kowalewski, and M. Pospelov, “Search for dark matter in  $b \rightarrow s$  transitions with missing energy,” *Phys. Rev. Lett.* **93** (2004) 201803, [arXiv:hep-ph/0401195](#).
- [68] P. Langacker and M. Plumacher, “Flavor changing effects in theories with a heavy  $Z'$  boson with family nonuniversal couplings,” *Phys. Rev.* **D62** (2000) 013006, [arXiv:hep-ph/0001204](#).

- [69] M. Blanke *et al.*, “Rare and CP-Violating  $K$  and  $B$  Decays in the Littlest Higgs Model with  $T^-$  Parity,” *JHEP* **01** (2007) 066, [arXiv:hep-ph/0610298](#).
- [70] M. Blanke, A. J. Buras, B. Duling, K. Gemmler, and S. Gori, “Rare  $K$  and  $B$  Decays in a Warped Extra Dimension with Custodial Protection,” *JHEP* **03** (2009) 108, [arXiv:0812.3803 \[hep-ph\]](#).
- [71] M. Bauer, S. Casagrande, U. Haisch, and M. Neubert, “Flavor Physics in the Randall-Sundrum Model: II. Tree- Level Weak-Interaction Processes,” [arXiv:0912.1625 \[hep-ph\]](#).
- [72] S. Bertolini, F. Borzumati, A. Masiero, and G. Ridolfi, “Effects of supergravity induced electroweak breaking on rare  $B$  decays and mixings,” *Nucl. Phys.* **B353** (1991) 591–649.
- [73] T. Goto, Y. Okada, Y. Shimizu, and M. Tanaka, “ $b \rightarrow s\ell\bar{\ell}$  in the minimal supergravity model,” *Phys. Rev.* **D55** (1997) 4273–4289, [arXiv:hep-ph/9609512](#).
- [74] A. J. Buras, T. Ewerth, S. Jager, and J. Rosiek, “ $K^+ \rightarrow \pi^+\nu\bar{\nu}$  and  $K_L \rightarrow \pi^0\nu\bar{\nu}$  Decays in the General MSSM,” *Nucl. Phys.* **B714** (2005) 103–136, [arXiv:hep-ph/0408142](#).
- [75] Y. Yamada, “ $b \rightarrow s\nu\bar{\nu}$  decay in the MSSM: Implication of  $b \rightarrow s\gamma$  at large  $\tan\beta$ ,” *Phys. Rev.* **D77** (2008) 014025, [arXiv:0709.1022 \[hep-ph\]](#).
- [76] G. Isidori and P. Paradisi, “Higgs-mediated  $K \rightarrow \pi\nu\bar{\nu}$  in the MSSM at large  $\tan\beta$ ,” *Phys. Rev.* **D73** (2006) 055017, [arXiv:hep-ph/0601094](#).
- [77] E. Lunghi, A. Masiero, I. Scimemi, and L. Silvestrini, “ $B \rightarrow X_s\ell^+\ell^-$  decays in supersymmetry,” *Nucl. Phys.* **B568** (2000) 120–144, [arXiv:hep-ph/9906286](#).
- [78] A. Ali, E. Lunghi, C. Greub, and G. Hiller, “Improved model independent analysis of semileptonic and radiative rare  $B$  decays,” *Phys. Rev.* **D66** (2002) 034002, [arXiv:hep-ph/0112300](#).
- [79] M. Misiak, S. Pokorski, and J. Rosiek, “Supersymmetry and FCNC effects,” *Adv. Ser. Direct. High Energy Phys.* **15** (1998) 795–828, [arXiv:hep-ph/9703442](#).
- [80] G. Colangelo and G. Isidori, “Supersymmetric contributions to rare kaon decays: Beyond the single mass-insertion approximation,” *JHEP* **09** (1998) 009, [arXiv:hep-ph/9808487](#).

- [81] Z.-j. Xiao, F.-g. Li, and W.-j. Zou, “ $B \rightarrow X_s \gamma$ ,  $X_s \ell^+ \ell^-$  decays and constraints on the mass insertion parameters in the MSSM,” *Commun. Theor. Phys.* **46** (2006) 687–696, [arXiv:hep-ph/0603120](#).
- [82] C. Bobeth, M. Misiak, and J. Urban, “Photonic penguins at two loops and  $m_t$ -dependence of  $\text{BR}(B \rightarrow X_s \ell^+ \ell^-)$ ,” *Nucl. Phys.* **B574** (2000) 291–330, [arXiv:hep-ph/9910220](#).
- [83] C. Bobeth, A. J. Buras, F. Kruger, and J. Urban, “QCD corrections to  $\bar{B} \rightarrow X_{d,s} \nu \bar{\nu}$ ,  $\bar{B}_{d,s} \rightarrow \ell^+ \ell^-$ ,  $K \rightarrow \pi \nu \bar{\nu}$  and  $K_L \rightarrow \mu^+ \mu^-$  in the MSSM,” *Nucl. Phys.* **B630** (2002) 87–131, [arXiv:hep-ph/0112305](#).
- [84] A. J. Buras, M. Misiak, M. Munz, and S. Pokorski, “Theoretical uncertainties and phenomenological aspects of  $B \rightarrow X_s \gamma$  decay,” *Nucl. Phys.* **B424** (1994) 374–398, [arXiv:hep-ph/9311345](#).
- [85] M. Beneke, T. Feldmann, and D. Seidel, “Systematic approach to exclusive  $B \rightarrow V \ell^+ \ell^-$ ,  $V \gamma$  decays,” *Nucl. Phys.* **B612** (2001) 25–58, [arXiv:hep-ph/0106067](#).
- [86] K. Hagiwara, A. D. Martin, and M. F. Wade, “Exclusive Semileptonic  $B$  Meson Decays,” *Nucl. Phys.* **B327** (1989) 569.
- [87] W. Altmannshofer *et al.*, “Symmetries and Asymmetries of  $B \rightarrow K^* \mu^+ \mu^-$  Decays in the Standard Model and Beyond,” *JHEP* **01** (2009) 019, [arXiv:0811.1214](#) [hep-ph].
- [88] U. Egede, T. Hurth, J. Matias, M. Ramon, and W. Reece, “New observables in the decay mode  $\bar{B} \rightarrow \bar{K}_0^* \ell^+ \ell^-$ ,” *JHEP* **11** (2008) 032, [arXiv:0807.2589](#) [hep-ph].
- [89] C. Bobeth, G. Hiller, and G. Piranishvili, “CP Asymmetries in bar  $B \rightarrow \bar{K}^*(\rightarrow \bar{K} \pi) \bar{\ell} \ell$  and Untagged  $\bar{B}_s, B_s \rightarrow \phi(\rightarrow K^+ K^-) \bar{\ell} \ell$  Decays at NLO,” *JHEP* **07** (2008) 106, [arXiv:0805.2525](#) [hep-ph].
- [90] F. Kruger and J. Matias, “Probing New Physics Via the Transverse Amplitudes of  $B^0 \rightarrow K^{*0}(\rightarrow K^- \pi^+) l^+ l^-$  at Large Recoil,” *Phys. Rev.* **D71** (2005) 094009, [arXiv:hep-ph/0502060](#).

- [91] J. Dickens, V. Gibson, C. Lazzeroni, and M. Patel, “A study of the sensitivity to the forward-backward asymmetry in  $B_d \rightarrow K^* \mu^+ \mu^-$  decays at LHCb,” CERN-LHCB-2007-039.
- [92] M. Beneke, T. Feldmann, and D. Seidel, “Exclusive radiative and electroweak  $b \rightarrow d$  and  $b \rightarrow s$  penguin decays at NLO,” *Eur. Phys. J.* **C41** (2005) 173–188, arXiv:hep-ph/0412400.
- [93] E. Lunghi and J. Matias, “Huge right-handed current effects in  $B \rightarrow K^*(K\pi)\ell^+\ell^-$  in supersymmetry,” *JHEP* **04** (2007) 058, arXiv:hep-ph/0612166.
- [94] D. Seidel, “Analytic two-loop virtual corrections to  $b \rightarrow d\ell^+\ell^-$ ,” *Phys. Rev.* **D70** (2004) 094038, arXiv:hep-ph/0403185.
- [95] G. Burdman, “Short distance coefficients and the vanishing of the lepton asymmetry in  $B \rightarrow V\ell^+\ell^-$ ,” *Phys. Rev.* **D57** (1998) 4254–4257, arXiv:hep-ph/9710550.
- [96] T. Feldmann and J. Matias, “Forward-backward and isospin asymmetry for  $B \rightarrow K^*\ell^+\ell^-$  decay in the standard model and in supersymmetry,” *JHEP* **01** (2003) 074, arXiv:hep-ph/0212158.
- [97] T. Onogi, “Heavy flavor physics from lattice QCD,” *PoS LAT2006* (2006) 017, arXiv:hep-lat/0610115.
- [98] P. Ball and R. Zwicky, “ $|V_{td}/V_{ts}|$  from  $B \rightarrow V\gamma$ ,” *JHEP* **04** (2006) 046, arXiv:hep-ph/0603232.
- [99] M. Steinhauser, “Precise Determinations of the Charm Quark Mass,” arXiv:0809.1925 [hep-ph].
- [100] P. Ball and R. Zwicky, “ $SU(3)$  breaking of leading-twist K and  $K^*$  distribution amplitudes: A reprise,” *Phys. Lett.* **B633** (2006) 289–297, arXiv:hep-ph/0510338.
- [101] **BABAR** Collaboration, B. Aubert *et al.*, “Angular Distributions in the Decays  $B \rightarrow K^*\ell^+\ell^-$ ,” *Phys. Rev.* **D79** (2009) 031102, arXiv:0804.4412 [hep-ex].
- [102] **BELLE** Collaboration, J. T. Wei *et al.*, “Measurement of the Differential Branching Fraction and Forward-Backward Asymmetry for  $B \rightarrow K^{(*)}\ell^+\ell^-$ ,” *Phys. Rev. Lett.* **103** (2009) 171801, arXiv:0904.0770 [hep-ex].

- 
- [103] A. J. Buras *et al.*, “Patterns of Flavour Violation in the Presence of a Fourth Generation of Quarks and Leptons,” [arXiv:1002.2126](#) [hep-ph].
- [104] T. Hurth, G. Isidori, J. F. Kamenik, and F. Mescia, “Constraints on New Physics in MFV models: A Model-independent analysis of  $\Delta F = 1$  processes,” *Nucl. Phys.* **B808** (2009) 326–346, [arXiv:0807.5039](#) [hep-ph].
- [105] E. Lunghi, A. Masiero, I. Scimemi, and L. Silvestrini, “ $B \rightarrow X_s \ell^+ \ell^-$  decays in supersymmetry,” *Nucl. Phys.* **B568** (2000) 120–144, [arXiv:hep-ph/9906286](#).
- [106] A. Ali, E. Lunghi, C. Greub, and G. Hiller, “Improved model independent analysis of semileptonic and radiative rare  $B$  decays,” *Phys. Rev.* **D66** (2002) 034002, [arXiv:hep-ph/0112300](#).
- [107] P. Gambino, U. Haisch, and M. Misiak, “Determining the sign of the  $b \rightarrow s\gamma$  amplitude,” *Phys. Rev. Lett.* **94** (2005) 061803, [arXiv:hep-ph/0410155](#).
- [108] A. J. Buras, A. Poschenrieder, M. Spranger, and A. Weiler, “The Impact of Universal Extra Dimensions on  $B \rightarrow X_s \gamma$ ,  $B \rightarrow X_s$  gluon,  $B \rightarrow X_s \mu^+ \mu^-$ ,  $K_L \rightarrow \pi^0 e^+ e^-$  and  $\varepsilon'/\varepsilon$ ,” *Nucl. Phys.* **B678** (2004) 455–490, [arXiv:hep-ph/0306158](#).
- [109] C. Bobeth, A. J. Buras, and T. Ewerth, “ $\bar{B} \rightarrow X_s \ell^+ \ell^-$  in the MSSM at NNLO,” *Nucl. Phys.* **B713** (2005) 522–554, [arXiv:hep-ph/0409293](#).
- [110] S. Baek and P. Ko, “Probing SUSY-induced CP violations at  $B$  factories,” *Phys. Rev. Lett.* **83** (1999) 488–491, [arXiv:hep-ph/9812229](#).
- [111] A. Bartl *et al.*, “General flavor blind MSSM and CP violation,” *Phys. Rev.* **D64** (2001) 076009, [arXiv:hep-ph/0103324](#).
- [112] J. R. Ellis, J. S. Lee, and A. Pilaftsis, “ $B$ -Meson Observables in the Maximally CP-Violating MSSM with Minimal Flavour Violation,” *Phys. Rev.* **D76** (2007) 115011, [arXiv:0708.2079](#) [hep-ph].
- [113] W. Altmannshofer, A. J. Buras, and P. Paradisi, “Low Energy Probes of CP Violation in a Flavor Blind MSSM,” *Phys. Lett.* **B669** (2008) 239–245, [arXiv:0808.0707](#) [hep-ph].
- [114] **Heavy Flavor Averaging Group** Collaboration, E. Barberio *et al.*, “Averages of  $b$ -hadron and  $c$ -hadron Properties at the End of 2007,” [arXiv:0808.1297](#) [hep-ex].

- [115] B. C. Regan, E. D. Commins, C. J. Schmidt, and D. DeMille, “New limit on the electron electric dipole moment,” *Phys. Rev. Lett.* **88** (2002) 071805.
- [116] M. Blanke *et al.*, “Rare and CP-Violating  $K$  and  $B$  Decays in the Littlest Higgs Model with  $T^-$  Parity,” *JHEP* **01** (2007) 066, [arXiv:hep-ph/0610298](#).
- [117] M. A. Shifman, A. I. Vainshtein, and V. I. Zakharov, “QCD and Resonance Physics: Applications,” *Nucl. Phys.* **B147** (1979) 448–518.
- [118] V. A. Novikov, M. A. Shifman, A. I. Vainshtein, and V. I. Zakharov, “Operator Expansion in Quantum Chromodynamics Beyond Perturbation Theory,” *Nucl. Phys.* **B174** (1980) 378.
- [119] R. J. Hill, “The modern description of semileptonic meson form factors,” [arXiv:hep-ph/0606023](#).
- [120] **QCDSF** Collaboration, A. Al-Haydari *et al.*, “Semileptonic form factors  $D \rightarrow \pi, K$  and  $B \rightarrow \pi, K$  from a fine lattice,” *Eur. Phys. J.* **A43** (2010) 107–120, [arXiv:0903.1664 \[hep-lat\]](#).
- [121] **UKQCD** Collaboration, K. C. Bowler, J. F. Gill, C. M. Maynard, and J. M. Flynn, “ $B \rightarrow \rho \ell \nu$  form factors in lattice QCD,” *JHEP* **05** (2004) 035, [arXiv:hep-lat/0402023](#).
- [122] A. Bharucha, T. Feldmann, and M. Wick, “Theoretical and Phenomenological Constraints on Form Factors for Radiative and Semi-Leptonic B-Meson Decays,” [arXiv:1004.3249 \[hep-ph\]](#).
- [123] S. Descotes-Genon and A. Le Yaouanc, “Parametrisations of the  $D \rightarrow K \ell \nu$  form factor and the determination of  $\hat{g}$ ,” *J. Phys.* **G35** (2008) 115005, [arXiv:0804.0203 \[hep-ph\]](#).
- [124] **UKQCD** Collaboration, A. M. Green, J. Koponen, C. McNeile, C. Michael, and G. Thompson, “Excited  $B$  mesons from the lattice,” *Phys. Rev.* **D69** (2004) 094505, [arXiv:hep-lat/0312007](#).
- [125] C. Bernard *et al.*, “Status of the MILC light pseudoscalar meson project,” *PoS LAT2007* (2007) 090, [arXiv:0710.1118 \[hep-lat\]](#).
- [126] R. Williams, C. S. Fischer, and M. R. Pennington, “Extracting the  $\bar{q}q$  condensate for light quarks beyond the chiral limit in models of QCD,” [arXiv:0704.2296 \[hep-ph\]](#).

- [127] M. V. Polyakov and C. Weiss, “Mixed quark-gluon condensate from instantons,” *Phys. Lett.* **B387** (1996) 841–847, [arXiv:hep-ph/9607244](#).

# Acknowledgements

First and foremost, I want to thank my advisor Prof. Andrzej J. Buras for the opportunity to graduate on such an interesting and topical subject as well as for the excellent care and correction of this work. I appreciate that he enabled me to travel to numerous conferences, workshops and schools.

Furthermore, my particular thanks go to Prof. Thorsten Feldmann for many stimulating discussions in- and outside physics and for introducing me in the complete works of *The Doors*.

I am indebted to my collaborators Wolfgang Altmannshofer, Andrzej Buras, Diego Guadagnoli, Patricia Ball, David Straub, Aoife Bharucha and Thorsten Feldmann. I wish them all the best for their future and thank David, Wolfgang and Yasutaka for their selflessly careful reading of the manuscript. I thank all the current and former members of T31: Andi J., Andi W., Andrzej, Anton, Björn, Cecilia, Christoph, David, Diego, Elmar, Felix, Gino, Katrin, Maria Valentina, Michaela, Monika, Paride, Sebastian, Stefan, Stefania, Thorsten, Tillmann, Wolfgang and Yasutaka. Special thanks go to Wolfgang who tolerated me for the last 4.5 years and created a motivating Zen-like atmosphere in our office.

Ich danke meiner Familie, im Besonderen meinen Eltern und Großeltern, für ihre fortwährende Unterstützung und Ermutigung. Grazie anche a Francesca per le piccole e grandi cose che ha fatto per me.